Title
DESIGN OF LOW CARBON DUAL-PHASE STEELS FOR HIGH STRENGTH WIRE

Author
Ahn, J.-H.

Publication Date
1986-08-01

Lawrence Berkeley Laboratory
UNIVERSITY OF CALIFORNIA

Materials & Molecular Research Division

DESIGN OF LOW CARBON DUAL-PHASE STEELS FOR HIGH STRENGTH WIRE

J.-H. Ahn
(Ph.D. Thesis)

August 1986

Prepared for the U.S. Department of Energy under Contract DE-AC03-76SF00098

DISCLAIMER

DESIGN OF LOW CARBON DUAL-PHASE STEELS FOR HIGH STRENGTH WIRE

Jae-Hwan Ahn

(Ph.D. Thesis)

Department of Materials Science and Mineral Engineering
University of California, Berkeley

and

Materials and Molecular Research Division
Lawrence Berkeley Laboratory
Berkeley, California 94720

August 1986

This work was supported by the Director, Office of Energy Research, Office of Basic Energy Sciences, Division of Materials Sciences of the U.S. Department of Energy under Contract No. DE-AC03-76SF00098.

DESIGN OF LOW CARBON DUAL-PHASE STEELS FOR HIGH STRENGTH WIRE

Jae-Hwan Ahn

Ph.D.

ABSTRACT

An investigation has been made to produce high strength wire from low carbon dual-phase steel using its high strain hardening rate and superior formability. This dual-phase steel wire is an alternative to conventional high strength wire, which is produced by cold drawing high carbon pearlitic steel rod to large strains with several intermediate annealing or patenting heat treatments.

Some alloy design considerations were assessed to develop a dual-phase steel suitable for cold drawing into high strength wire. The effects of metallurgical variables such as martensite particle size, shape, volume fraction and ferrite grain size on controlling the strength-ductility balance were described, and their role during the wire drawing process characterized.

The dual-phase steel of composition Fe-2% Si-0.1% C, which has been developed according to the selected design guidelines, was

found to be the most promising material for high strength wire application. This steel could be continuously drawn to strength levels found in commercial high carbon pearlitic wires without any intermediate patenting treatments during the drawing process, resulting in reductions of production cost and operation complexity. The attractive properties found in the silicon containing dual-phase steel are attributed to its microstructural feature; fine, fibrous and disconnected lath martensite particles in a fine ferrite matrix.

This desirable dual-phase microstructure can be produced by austenitizing and quenching to form 100% martensite, followed by two phase annealing and subsequent quenching or in the as-rolled condition by rolling in the two phase region and quenching after controlled deformation in the austenite region. It is recommended that the quench after two phase annealing or finish rolling be as rapid as possible to prevent austenite pool shrinkage or decomposition prior to its transformation to martensite.

DESIGN OF LOW CARBON DUAL-PHASE STEELS FOR HIGH STRENGTH WIRE

Table of Contents

1. INTRODUCTION

Conventionally, high strength steel wire in use for tire cord, wire rope, prestressed concrete and springs, etc. has been made by cold drawing wire rod, which is manufactured by patenting the hot rolled rods of various carbon contents. Patenting is a heat treatment applied to wire rod and wire generally having a carbon content of 0.4 per cent and higher, the term being peculiar to the wire industry. The object of patenting is to obtain a fine lamellar pearlitic structure, which has high tensile strength with high ductility and thus impart to the wire rod the ability to withstand the severe distortions during the wire drawing process. This heat treatment consists of heating the as-received hot rolled rod above the critical temperature for a time long enough for complete transformation to austenite, followed by cooling in air or quenching to a bath of molten lead, or in some cases, in molten salts of a predetermined temperature where the austenite is transformed to the desired fine pearlitic structure (1-4).

Since the patenting process mentioned above is complex and expensive, wire rod manufacturers have sought to produce a fine pearlitic microstructure directly and in sequence with a rod rolling mill without the separate patenting treatment. Therefore, a number of processes have been developed to obtain a patented structure from the hot worked austenite by controlling the cooling rate of hot rolled rods (e.g., EDC, Stelmor process) and/or adding microalloying

elements (5-10). For example, in the Stelmor process, a rod on a single-strand basis from the finishing mill is rapidly water cooled to a predetermined temperature, formed into rod rings by a laying head and deposited on a conveyer in an overlapping pattern which provides uniform cooling at controlled rates. This process not only complements the higher rolling speeds of today's modern rod mills, but enables heavier weight coils to be produced.

After the wire rod is patented, it is then cold drawn to high strength wire of the desired diameter. If very high strength and/or small diameters are desired, the wire must be patented more than once before the desired size and properties are reached. For example, a typical manufacturing process of steel tire cord is shown in Fig. 1, which involves the two intermediate patenting treatments to obtain the required strength. Clearly the elimination of this patenting process during wire drawing as well as the addition of microalloying elements would be of significant economic value.

An alternative to high carbon pearlitic steel as wire rod which could be cold drawn in a simple drawing process without intermediate annealing or patenting treatments has been desired by wire manufacturers. The potential of a dual-phase steel, which was initially developed for cold formable sheet especially in automotive applications, has been demonstrated as starting wire rod for high strength wire in recent years by Thomas and Nakagawa (11,12).

Dual-phase steel is a new class of high strength low alloy (HSLA) steels characterized by a microstructure consisting of

inherently strong martensite particles embedded in a soft, ductile ferrite matrix. The major source of strengthening in the dual-phase steels arises from the presence of inherently strong martensite as a load carrying constituent in a soft ferrite matrix which supplies the system with the essential element of ductility.

Since the introduction of dual-phase steel (13-15), considerable research effort has been directed toward understanding and improving this steel as reported at five symposia on this subject (16-20). This dual-phase steel is produced by a variety of thermal and thermomechanical treatments, all of which involve cooling a composite of ferrite and austenite at a rate sufficient to transform austenite to martensite. The resulting mixture is analogous to that of a composite and the concept of fiber-reinforced composite strengthening is thus useful in qualitatively understanding dual-phase steels (11). Empirically, it has been found that the mechanical properties appear to follow a law of mixtures (21-24). For example, the general expression for the ultimate tensile strength (σ_c) of dual phase steels approximating to a fiber-reinforced composite model is given by

$$\sigma_c = \sigma_\alpha(1 - V_m) + \sigma_m V_m$$

where σ_α is the stress in ferrite at the ultimate tensile strain of martensite, σ_m is the tensile strength of martensite, and $(1 - V_m)$ and V_m are their respective volume fractions. However, deviations

from the above equation can occur when third phase precipitates especially in the ferrite matrix are present (25-28).

The characteristics of dual-phase steels are low yield strength, continuous yielding behavior, high initial work hardening rate and good ductility. Because of these properties, dual-phase steels are regarded as attractive materials, particularly for applications where both formability and strength are required. Figure 2 shows typical stress-strain curves of dual-phase steels (29). For comparison, a stress-strain curve of a ferrite-pearlite steel is included.

The low yielding and the absence of discontinuous yielding in dual-phase steels has been explained in terms of both the residual stresses and high dislocation density in the ferrite matrix surrounding the martensite particles (30,31). The lattice shear and volume expansion accompanying the austenite to martensite transformation (32,33) during cooling from ferrite + austenite region causes a distortion between the product martensite and the ferrite matrix. This distortion generates residual stresses (34,35) and introduces a high density of mobile dislocations into the ferrite regions adjacent to the martensite particles (13,36), causing yielding to occur at low stress levels. Yielding also occurs uniformly throughout the material because the heavily dislocated ferrite regions around the martensite particles which serve as slip initiation sites (due to the transformation induced residual stresses and mobile dislocations) are distributed uniformly

throughout the material, giving rise to continuous yielding behavior.

The early yielding is followed by a high initial work hardening rate. The rapid increase in work hardening at low plastic strains can be explained as follows. In the very early stages of deformation following yielding, the residual stresses are being eliminated (35) and the built-in mobile dislocations are being immobilized by dislocation-dislocation interactions or by gliding to a ferrite-martensite interface (31). Therefore, the stress required for continued plastic deformation must increase rapidly to a level adequate for the nucleation and propagation of new, mobile dislocations. In the later stages of deformation, the dual-phase steel essentially behaves as a particulate composite consisting of a ductile ferrite matrix containing hard martensite particles (37,38). During plastic deformation, the dual-phase steels develop a greater nonhomogeneous internal stress field in the ferrite matrix caused by unrelaxed plastic strain gradients between the ferrite and martensite. This effectively restrict dislocation motion and produces a higher rate of work hardening. The high work hardening rate of dual-phase steel provides a high tensile strength despite the low yield strength and increase the uniform elongation values by delaying the onset of necking in uniaxial tension tests. More importantly, it suppresses the onset of plastic instability in multiaxial metal forming operations to yield improved formability (39).

In the present work, an attempt has been made to utilize the characteristics of this dual-phase steel to produce high strength wire as an alternative to existing practice using pearlitic high carbon steels. Dual-phase steel was selected as the starting material for cold drawing into high strength steel wire because of its pronounced strain hardening rate and superior formability as mentioned before. The rapid strain hardening of this steel could provide an increase in strength with less cold reduction. Also, the superior formability of dual-phase steel could enable it to be drawn to large strains in a continuous, multipass drawing process without intermediate heat treatments. In general, the alloy composition and processing of dual-phase steels are quite simple and they can be varied to produce a wide range of microstructure and mechanical properties to fit the specific applications. These advantages are in addition to the simplicity and low cost of the wire drawing process.

To produce the high strength wire in one continuous, multipass cold drawing operation, it is a prerequisite that the starting dual phase steel for wire drawing should have a good combination of strength and formability. Since dual-phase steel is a composite, its mechanical properties would be influenced by metallurgical parameters such as the size, shape and volume fraction of martensite particles and the properties of the individual phases.

Therefore, one objective in the current research was to clarify the role of microstructural factors (size, shape, distribution and

volume fraction) of the constituents in dual-phase steels on their initial tensile properties and wire drawing behaviors, and from this to design a dual-phase steel of appropriate microstructure and properties for cold drawing into high strength wire. The other objective was to study the high strain deformation behavior of dual-phase steels during wire drawing in terms of the structure of highly deformed ferrite and martensite.

2. APPROACH

The adopted approach to develop a desirable dual-phase steel for the high strength wire application is primarily that of microstructural manipulation by heat treatment, alloying or combinations of both. In what follows, the design guidelines for developing a desirable dual-phase structure are outlined and in the subsequent section, the choice of heat treatments and alloying elements based on these principles is discussed.

2.1 Design Guidelines

(1) Volume fraction of martensite: According to the law of mixtures, the tensile strength of dual-phase steel is linearly proportional to the volume fraction of martensite present. The amount of martensite must exceed a lower limit in order to achieve a substantial contribution to strengthening and to eliminate yield point elongation (31,40). At the same time, there must not be so much martensite in the dual-phase steel where a crack in the martensite particles would propagate throughout the structure and lead immediately to its failure. Thus, an optimum range of volume fraction of martensite should be achieved so that the ferrite matrix can locally work harden and carry the transferred load.

(2) Size, shape and distribution of martensite particles: A fine scale of martensite particles is desirable. Although both the flow stress and the work hardening rate increase with decreasing

size of the martensite particle, recent investigations (41,42) showed that the work hardening rate increased more than the flow stress, which inherently increased the uniform elongation and hence the formability. With regard to shape factors, load transfer is most efficient when the second phase (martensite) is present in the form of fibers rather than spheres (43), which would tend to reduce void formation during the wire drawing process. This is primarily because the transfer of load occurs by shear acting along the martensite/ferrite interfaces and, for a given volume fraction and the same number of martensite particles, more interfacial area is available in the case of a fibrous morphology. In addition, connected martensite particles throughout the ferrite matrix should be avoided since they will be directly loaded at their ends. This will cause the particles to break in the early stage of plastic deformation and prevent the ferrite from contributing its full ductility.

(3) Properties of martensite: The inherently strong martensite in dual-phase steel is a diffusionless transformation product of carbon enriched austenite. In martensitic steels, the toughness drops with increasing carbon content as transformation substructure changes from dislocated lath martensite to twinned plate martensite (44,45). To ensure good toughness, dislocated lath martensite is desirable, so the carbon content in the martensite phase must not to exceed $\sim$ 0.4 wt.%.

(4) Properties of ferrite: The properties of the ferrite matrix are known to be responsible for the enhanced ductility of dual-phase steels (46). Therefore, the ferrite should be free of fine precipitates and interstitial alloying elements so as to maximize the ductility, and should possess a fine grain size for maximum strength. These metallurgical factors depend on selected alloying elements and heat treatment.

(5) Nature of interfaces: The stress in the continuous ferrite matrix is transferred to the strong martensite particles by shear forces which act at the ferrite/martensite interface. Hence, the nature of the interface is of critical importance. If carbide particles precipitate along the interface, they may cause local stress concentrations. These stress concentrations promote the formation of cracks within these carbides leading to the ultimate failure of the system. Therefore, the precipitation of carbide at the ferrite/martensite interface should be avoided. In addition, a high degree of coherency between the ferrite and martensite phases is desired. On the basis of thermodynamic considerations, a high energy interface is more likely to fail under stress than a low energy one, since the interfacial energy can supply some of the work for the separation of particles from the matrix.

2.2 Processing and Alloying Elements

The design guidelines discussed in the previous section suggest microstructural features which are desirable for dual-phase steels.

These microstructural features can be achieved through a combination of heat treatments and alloying. The choice of heat treatments and alloying elements will be discussed in this section.

2.2.1 Processing

The production of a dual-phase microstructure which consists of ferrite and martensite can be achieved by a variety of thermal and thermomechanical treatments, all of which involve cooling a composite of ferrite and austenite at a sufficient rate to transform austenite to martensite. In this study, two methods of processing have been investigated to produce desirable dual-phase steels for cold drawing into high strength wire.

A. Intermediate Quenching Process

This heat treatment consists of austenitizing and quenching to 100% martensite, followed by annealing in the (α+γ) region and then quenching to room temperature as shown in Fig. 3. During annealing in the two phase range, martensite transforms partially to austenite and the residual martensite becomes ferrite as the two phases attain the composition specified by the tie line corresponding to the annealing temperature. The alloy will then consist of low carbon ferrite and high carbon austenite phases. Upon quenching, a dual-phase steel of ferrite and martensite is produced through the austenite to martensite transformation.

This heat treatment was developed so as to fully exploit the characteristic nature of the initial martensite structure prior to subsequent annealing in the (α+γ) range. The initial martensite structure provides numerous heterogeneous nucleation sites for austenite during two phase annealing (14,47). Then the austenite grows along the initial martensite lath boundaries resulting, after quenching, in a fine fibrous distribution of martensite in a ferrite matrix. The volume fraction of martensite is controlled by the annealing temperature in the two phase region, increasing with the annealing temperature. The feasibility of this method was proved by Nakagawa and Thomas (12).

B. Controlled Rolling Process

Controlled rolling is one of the processing techniques that simultaneously improves the strength, ductility and toughness of the steel in the as-hot-rolled condition (48,49). This improvement in properties is mainly due to refinement of the microstructure, which is obtained by careful control of the rolling process variables, especially the amount of deformation and the deformation temperature. This process is also attractive from an economic point of view since dual-phase steels are produced directly from the rod mill without further processing.

The controlled-rolling process employed in this work was divided into three stages: deformation in the austenite recrystallization temperature region, deformation in the austenite

non-recrystallization region above Ar_3 temperature and deformation in the austenite-ferrite region. Fig. 4 illustrates schematically the three stages of the controlled rolling process along with the microstructural change accompanying the deformation in each stage.

a. First Stage: Deformation in the Austenite Recrystallization Region

The basic idea of the controlled rolling process is that the fine microstructure is achieved mainly through austenite grain size refinement. Therefore, the austenite grain size should be refined as much as possible by consecutive deformation and recrystallization in this high temperature range. The amount of deformation applied plays an important role on the recrystallized austenite grain size, which decreases rapidly, reaching a limiting value as the amount of deformation increases (50). Although deformation at a lower temperature produces smaller austenite grain size, it has been shown that the effect of temperature is slight (50).

It must also be emphasized that the recrystallization accompanying hot deformation does not occur under all conditions. On the contrary, it is necessary to apply more deformation than the critical amount required for completion of recrystallization. It has been shown that the critical amount of deformation for recrystallization generally increases with decreasing deformation temperature and decreases with refinement of initial austenite grain size. Below the critical amount of deformation, partial recrystallization occurs, producing a duplex austenite structure

comprising fine, recrystallized grains together with large deformed but unrecrystallized grains (50,51). This duplex austenite structure leads to a non-uniform structure after transformation and cannot be removed by subsequent rolling (52), thus partial recrystallization should be avoided.

b. Second Stage: Deformation in the Austenite Non-Recrystallization Region

In order to decrease grain size further, deformation in the austenite non-recrystallization region must be applied following deformation in the recrystallization region. This deformation produces elongated austenite grains with deformation bands within these grains (51). Both of these effects influence ferrite nucleation and size. Since austenite grain boundaries are the preferred sites for ferrite nucleation, the elongation of austenite grains increases the number of ferrite nucleation sites and inhibits the grain growth of ferrite. Deformation bands can also serve as nucleation sites. With an increasing amount of deformation, the austenite grains become more elongated, increasing their length-to-thickness ratio. Also, the number of deformation bands increases rapidly and their distribution becomes uniform, giving rise to fine and uniform ferrite grains.

c. Third Stage: Deformation in the Austenite-Ferrite Region

In this stage, ferrite nucleates from heavily deformed austenite during cooling and is itself deformed, giving rise to the formation of subgrains through recovery and/or recrystallization (53-55). Therefore, deformation in the two-phase region produces a structure consisting of elongated austenite (a fraction of elongated austenite might transform to ferrite during deformation) and fine recrystallized ferrite grains and subgrains. When this mixed structure is directly quenched after deformation, the dual-phase structure is developed in which the martensite particles are more or less unidirectionally aligned in the fine grained ferrite matrix.

2.2.2 Alloying Elements

Increasing the carbon content of steel is by far the most effective and economical way of raising the strength of steel. However, these significant gains in strength are generally accompanied by a deterioration of the toughness, because, in the martensitic steels, a high carbon content (>0.4 wt.%) causes microstructural twinning (44,45). To produce dislocated lath martensite in dual-phase steels with 20-50% martensite, the average carbon content in the initial alloy should be kept sufficiently low to be about 0.1 wt.% so that the carbon concentration in the martensite phase is approximately less than 0.4 wt.%.

Among the substitutional alloying elements, silicon was found to be the most favorable for controlling the design parameters of

interest, based on the following observations:

(1) Silicon broadens the (α+γ) range when added to the Fe-C system and increases the slope of the A_3 line, as shown in Fig. 7 (56). Therefore, small temperature variations in the two phase region do not significantly change the volume fraction and composition of the martensite produced, thereby assuring reproducibility of the materials. Especially in the contolled rolling process, the structure and properties of dual-phase steels are less sensitive to variation in the finish rolling temperature. The silicon containing steel is also desirable to produce dual-phase steels at finish-rolling temperatures commonly used in commercial mills (>900^{o}C).

(2) Silicon provides very effective solid solution strengthening in ferrite and reduces the carbon content of ferrite, which will lead to a "cleaner", more ductile ferrite (57). In cold drawn steel wires, it can reduce the amount of cold work necessary to achieve the same combinations of strength and ductility (58).

(3) Silicon improves the ferrite-martensite interface by inhibiting the formation of coarse carbides during the final quenching from the two phase region (30,59).

2.3 Wire Drawing

The principal function of wire drawing is to make wire of a specified size and to afford the necessary strength to the wire through work hardening. This is done by pulling a wire or rod of

initial radius (R_0) through a conical portion of a die, as shown in Fig. 8. While passing through the die, the wire deforms plastically and decreases to radius R_f. The pull and the nip of the die, together, stress the metal sufficiently for it to deform plastically within the confines of the die. However, the reduction in size attainable thereby is limited by the pull that the wire can sustain without breaking, so that the operation has to be repeated, usually a great many times.

One of the most common wire breaks that occur frequently during wire drawing practice is caused by central burst, also called chevroning or cup and cone fracture (60,61). Generally, the tendency for this metal working defect to occur increases as the reduction per pass and the strain hardening of the material decrease, and as the die angle and coefficient of friction increase. The wire during drawing can be divided into three regions, i) the rigid inlet, ii) plastically deforming workpiece and iii) the rigid, already deformed outlet. The velocity of the metal in the deforming region gradually increases from that of the inlet wire to that of the faster moving outlet wire. When the plastic deformation zone does not go up to the center of the wire, the rigid body associated with the exit touches the rigid body associated with the entrance. Since the exit velocity (V_f) is faster than that at the entrance (V_0), a fracture must initiate at the point of contact between the rigid inlet and the rigid outlet, causing a burst to form as shown in Fig. 9. This relieves the incompatibility between the two rigid

zones and allows sound flow to resume with uniform plastic deformation occurring between the two rigid zones. Eventually, the plastic zone narrows again to create another burst and the process repeats itself during drawing.

To prevent the occurrence of central burst during wire drawing, Avitzur presented a criterion that defines permissible combinations of the two process parameters; reduction of area and die cone angle (62). According to his diagram, a die of 6^{o} semicone angle being used in this work and a friction coefficient of 0.1 requires at least 37% reduction in area to be safe from central bursting. However, this is a conservative value that guarantees that central bursting will not occur; but is not necessarily the minimum value needed, especially for ductile and high strain hardening materials.

An analytical approach to prevent the central burst is to determine the homogeneity of the deformation by the parameter, Δ, used by Backofen (63). Δ is defined as the ratio of the mean diameter or thickness, H, of the work material to the contact length, L, between tool and work material,

$$\Delta = H/L$$

For wire drawing, this ratio is given by

$$\Delta_W = \alpha(1 + \sqrt{1-r})^2/r$$

where α is the semi-die angle in radians, $r = 1 - (d_f/d_o)^2$ is the reduction in area, d_o is the diameter of the wire entering the die,

and d_f is the diameter of the wire exiting the die. Thus, Δ increases with decreasing reduction in area and increasing die angle. Homogeneous deformation is defined by a ratio of 1 or less and a ratio of 2 or greater produces very inhomogeneous deformation. According to this criterion, a reduction of 34% is required to give a Δ of 1 for a 6^0 semicone angle die being used.

The maximum attainable reduction per pass is the point where the drawing load exceeds the breaking strength of the wire at the exit of the die. This is given by Caddell (64) as:

$$r_{max} = 1 - e^{-\eta(n+1)}$$

where η is the efficiency of the drawing process taking into account friction and redundant work, and n is the strain hardening exponent, which is usually in the range of 0.20 to 0.35 for dual-phase steels (23,39). Thus, a theoretical maximum reduction per pass is 74%. However, this value is greatly reduced by η in actual processes and applies only to the first pass since the value of n decreases with strain (23).

It has been also shown that drawing practice applying heavy reduction in area per pass should be avoided, since this condition would increase the hydrostatic stress concentration on the central axis of the wire inside the plastic deformation zone (65). These tensile hydrostatic stresses would favor formation of cup and cone wire breaks due to void coalescence into microcracks. Therefore, an analytically approached value of 34% reduction per pass was

eventually used in this work rather than a conservative empirical value of 37% reduction per pass as the minimum to prevent central burst.

3. EXPERIMENTAL PROCEDURE

3.1 Material Preparation

The materials used in this investigation are high purity Fe/0.1C/X where X is Si or Mn. The alloy codes and the chemical compositions are listed in Table 1. The alloys were prepared and provided by Nippon Kokan K.K., Japan. They were vacuum induction melted and cast in 110 lb ingots. After soaking at 1250°C for 3 hours and hot rolling, the billet was cut into smaller pieces and hot open die forged into bars of 0.6 inch in diameter and 6.5 feet long.

3.2 Measurement of Phase Transformation Temperatures

To roughly assess the ranges of the (α+γ) field, phase transformation temperatures were measured using a Theta Dilatronic III R dilatometer. A schematic of a specimen used in this experiment is shown in Fig. 10. Each specimen was heated to 1150°C and held for 10 minutes before cooling to room temperature. Since the pressure of the specimen chamber was maintained below 10^{-5} torr, the specimen surface was well protected from oxidation. A programmed linear heating and cooling rate of 125°C/min was used. Transformation temperatures were determined as first deviation points from linearity on dilation and temperature versus time charts. The experiment was repeated on the same specimen until consistent data were obtained.

3.3 Heat Treatment

In order to produce desirable dual-phase microstructure, two kinds of heat treatments (intermediate quenching and controlled rolling processes) have been carried out in this investigation as mentioned in the previous chapter. For comparison, and in order to study the effect of size and shape of martensite particles on the initial properties and drawing behavior of dual-phase steels, other heat treatments (intercritical annealing and step quenching processes) were conducted, which will be described later in this section.

3.3.1 Intermediate Quenching Process

Oversized tensile test specimens and wire rods of 0.25 inch diameter were machined from the as-received bars. These were then heat treated in a vertical tube furnace under a flowing argon atmosphere according to the schedule shown in Fig. 3. Samples were austenitized for 30 minutes at 1150^{o}C for the 2% Si steels and at 1100^{o}C for the 1.5% Mn steel and subsequently quenched into agitated iced brine. After obtaining a fully martensitic structure, the specimens were annealed in the (α+γ) two phase region for 10 minutes and once again quenched into agitated iced brine. The two phase annealing temperatures were chosen so as to obtain the required volume fraction of martensite as shown in Table 3.

3.3.2 Controlled Rolling Process

The controlled rolling process employed in this research was three step rolling which involved rolling in the austenite recrystallization region, rolling in the austenite non-recrystallization region, and rolling in the ($\alpha+\gamma$) two-phase region (Fig. 4). For the 2% Si steel, an as-received bar of 0.6 inch diameter was soaked at 1150°C for 30 minutes and hot rolled 50% in one pass at 1100°C, hot rolled 30% in one pass at 1020°C and then hot rolled 35% in one pass at 950°C on two-high reversing bar mills. The 1.5% Mn steel was hot rolled 50% at 1000°C after being soaked at 1100°C for 30 minutes, followed by hot rollings 30% at 850°C and 35% at 740°C. After finish rolling to a final diameter of 0.25 inch, all rods were quenched into agitated iced brine.

Finish rolling temperatures were chosen to be near the Ar_3 temperature, measured under an unstrained condition to obtain the desired mechanical properties (66). During the rolling operation, the temperature was monitored by a thermocouple inserted at the midpoint of the cross section of the rod.

3.3.3 Intercritical Annealing Process

Oversized blanks for tensile test specimens and wire rods were machined down to 0.25 inch in diameter and heated directly into the ($\alpha+\gamma$) two phase field in a vertical tube furnace under a flowing argon atmosphere (Fig. 5). After annealing for 10 minutes at

various temperatures, the specimens were dropped through the bottom of the furnace into agitated iced brine.

3.3.4 Step Quenching Process

This heat treatment was designed to intentionally obtain a coarse dual-phase microstructure as shown in Fig. 6. The oversized tensile test specimens and wire rods were austenitized for 30 minutes at 1150^{o}C for the 2% Si steels and at 1100^{o}C for the 1.5% Mn steels, and then transferred directly to an adjacent furnace at the desired two phase temperature. After holding for 10 minutes in the two phase regions, the specimens were directly quenched into agitated iced brine.

3.4 Wire Drawing

Heat treated rods of 0.25 inch diameter and 4 inch long were machined to a diameter of 0.217 inch (5.5 mm). They were then pointed by swaging and drawn through carbide or diamond dies of 6^{o}-8^{o} semicone angle lubricated with Dupont Vydax Freon-Teflon dispersion. The drawing schedule used in this experiment had a moderately high reduction of 35% per pass in the early stages where central bursting is a greater problem as mentioned in the previous chapter and gradually decreased to 22% per pass in the later stages to reduce the drawing load while remaining in a region which is apparently safe from central bursting. The drawing schedule used is presented in Table 9. Drawing was always done in the same direction

since pass reversal results in poorer properties and higher residual stress (67). The usual drawing speed was 1.2 inch/sec, resulting in a strain rate of 3/sec in the larger sizes to 33/sec in the smaller sizes.

3.5 Mechanical Testing

3.5.1 Tensile Testing

Tensile properties of the dual-phase steels in the as-heat-treated condition were determined using cylindrical tensile specimens as shown in Fig. 11. They were machined to final dimension from the oversized heat-treated blanks according to the ASTM specification (68). Tensile testing was carried out at room temperature on an Instron testing machine at a strain rate of 0.04/minute. Total elongations were determined by measuring the difference in distance between gauge length marks before and after testing with an optical microscope equipped with a Vernier translating stage having a precision of 0.001 inch. The reduction in area was calculated from measurements of the gauge section diameter before and after tensile testing. The other tensile properties were determined from the load-displacement curve recorded by the testing machine. The yield strengths were determined by the 0.2% offset method.

A tensile test of the drawn wires was performed at room temperature on an Instron testing machine at strain rates of 0.005-0.02/minute. The 4 inch long wires of larger than 0.0362 inch in

diameter were tested in self tightening wedge grips. In this case, the gauge diameter was machined to give approximately 90% of the original cross sectional area to prevent failure in the grips. Smaller diameter wires were tested using drum type grips, in which fine wire was wrapped around the drum, then tightened with a screw. The values of tensile properties reported are averages of at least two tests.

3.5.2 Microhardness Testing

Vickers microhardness testing was done on transverse sections of drawn wire with a Buehler Micromet microhardness tester using a 50 gm load. Wire specimens for this test were prepared in the same manner as those for optical metallography. Values reported are the average of at least ten measurements.

3.6 Metallography

3.6.1 Optical Metallography

Samples for optical metallography were cut from heat treated rods or drawn wires under flood cooling. After mounting in either Bakelite or Koldmount, the specimens were hand ground successively on wet silicon carbide paper from 240 grit to 600 grit. The final polishing was done using 1 micron diamond paste on a polishing wheel with kerosene as a lubricant. After the microstructural features were revealed by etching in a 2% Nital solution, the microstructures were observed and recorded with a Zeiss Ultraphot II metallograph.

The volume percent of martensite particles was determined by standard quantitative metallography using the linear intercept method (69).

3.6.2 Scanning Electron Microscopy

Specimens for scanning electron microscopy were prepared in the same manner as those for optical metallography and then a thin film of gold was evaporated onto the SEM specimen to reduce the effects of specimen charging. They were observed in an ISI DS-130 scanning electron microscope operated at 20 kV. The fracture morphology was thoroughly examined on the fracture surfaces of broken tensile specimens. Fracture surfaces selected for examination were ultrasonically cleaned and stored in a desiccator until examination.

3.6.3 Transmission Electron Microscopy

Thin foils for transmission electron microscopy of the as-heat treated steels were obtained from the same heat treated rods used for the preparation of specimens for optical metallography. Slices of approximately 15 mils thick were cut from these rods under flood cooling to minimize specimen heating. These slices were then chemically thinned to 4 mils in a solution of H_2O_2 containing 4% HF at room temperature. Then discs of 3 mm in diameter were punched from these slices, followed by grinding to a thickness of about 2 mils on wet silicon carbide paper of 600 grit and cleaned with acetone. The thin discs were electropolished in a twin jet

electropolishing apparatus at room temperature using a solution of 75 grams CrO_3, 400 ml CH_3COOH and 21 ml of distilled water. Polishing potentials of 35-50 volts were used. The thin foils were then examined with a Philips EM 301 transmission electron microscope at an accelerating voltage of 100 kV.

TEM specimens for longitudinal sections of the drawn wires were made by mechanical grinding and polishing two sides of the wire to make a thin strip of 1 mil thick and as wide as the original wire diameter. Samples were then mounted on 3 mm oval hole copper grids using a liquid adhesive containing colloidal silver in suspension. Final thinning to a thickness transparent to electrons was achieved by ion milling in a liquid nitrogen cooled holder. Argon ions accelerated by a 6 kV potential incident at an angle of 20-25 degrees were used for sputtering. As perforation was approached, the angle of incidence was generally decreased to approximately 15 degrees to maximize the amount of the thin wedge area produced.

Transverse sections of the drawn wires were made by nickel plating the wire to a total diameter of 3 mm and slicing off 12 mil thick discs with an Isomet low speed saw. These discs were then hand ground on wet silicon carbide papers to a thickness of 2 mils and jet polished as above.

4. RESULTS

4.1 Phase Transformation Temperatures

The measured phase transformation temperatures by dilatometry are tabulated in Table 2. The temperature intervals between Ac_1 and Ac_3 allow a rough assessment of the boundaries of the ($\alpha+\gamma$) phase field for the intermediate quenching and intercritical annealing treatments, and those between Ar_1 and Ar_3 for the step quenching and controlled rolling treatments. The results of the transformation temperature experiments show that Si opens up the ($\alpha+\gamma$) range while Mn contracts it. These findings are in agreement with the Fe/Si/C and Fe/Mn/C phase diagrams reported in the literature (70,71).

Extensive isothermal experiments were conducted to determine the annealing temperatures in the ($\alpha+\gamma$) range for each alloy. Table 3 shows the results of the annealing temperatures in the ($\alpha+\gamma$) range corresponding to the respective volume fraction of martensite.

4.2 Microstructure

4.2.1 Initial Microstructure

Upon annealing in the ($\alpha+\gamma$) region, the alloy will separate into a mixture of austenite phase with a high carbon content and ferrite phase with a low carbon content. The relative proportion of each phase depends on the tie line specified by the annealing temperature.

The formation of either the ferrite or the austenite during two phase annealing determines the final microstructure of dual-phase steels. Thus the dual-phase structure is highly dependent upon the starting microstructure present prior to two phase annealing. As expected, there are considerable differences in the resulting morphologies which were obtained by various heat treatments. The results of the metallographic studies are summarized in this section.

A. Intermediate Quenching Process

The initial as-quenched martensitic structures before being subjected to the two phase annealing in this treatment are shown in Fig. 12. The prior austenite grain is partitioned into several packets which consist of parallel highly dislocated laths, typical of low-carbon martensite. Each lath forms directly from an independent homogeneous shear, and successive shear transformations produce a packet (72). The lath boundaries are typically of low angle character, whereas the packet boundaries are usually high angle (44,73).

Figure 13 shows a typical transmission electron micrograph of the initial microstructure prior to two phase annealing, which was found to be predominantly dislocated lath martensite with retained austenite films along the lath boundaries. The existence of retained austenite was expected since its presence in such low carbon steels had been detected earlier (30,74). Indexing of the

selected area diffraction pattern indicates that the crystallographic relation between austenite and martensite is the Kurdjumov-Sachs orientation relationship $<111>_{\alpha}//<1\bar{1}0>_{\gamma}$, confirming the previous observations that have been made on various carbon steels (45,74).

Figure 14a shows the dual-phase microstructures developed in 2% Si steels after two phase annealing. In these scanning electron micrographs, the needle-like particles of light contrast correspond to the martensite phase and the darker background to the ferrite phase. The microstructure of the silicon containing dual-phase steel consists of a fine, fibrous distribution of martensite particles in a ferrite matrix, which reflects the influence of the initial martensitic structure before two phase annealing. During annealing in the ($\alpha+\gamma$) region, the austenite nucleates at and grows along the initial martensite lath boundaries forming the parallel acicular pools within the prior packet and then transforms to fine, fibrous martensite particles upon quenching to room temperature.

The dual-phase microstructure of the 1.5% Mn alloy subjected to the intermediate quenching process is shown in Fig. 14b. As can be seen in this micrograph, martensite particles exhibit a continuous network along the prior austenite grain boundaries with an acicular morphology in the interior of the prior austenite grains. This clearly indicates that during annealing in the ($\alpha+\gamma$) region, formation of austenite from the initial martensitic structure starts at the prior austenite grain boundaries and also, at the martensite

lath boundaries. The austenite formed at prior austenite grain boundaries adopted a mixture of grain boundary allotriomorphs and idiomorphs. This feature is not present in the case of the silicon containing dual-phase steels.

The volume fraction of martensite for each structure as determined by the line intercept method is given in Table 3. As expected from the tie-line-construction for the corresponding phase diagram, the volume fraction of martensite increases with annealing temperature in the ($\alpha+\gamma$) field.

The substructure of the martensite in these dual-phase steels (Figs. 15 and 16) also consists of dislocated lath martensite and does not differ significantly from the initial martensitic structure, except for some areas which contain fine internal twins due to the increase of carbon content in the austenite phase during two phase ($\alpha+\gamma$) annealing. The substructure of the ferrite region shows the formation of subgrains and a high dislocation density in the ferrite regions adjacent to the martensite particles. During the two phase annealing process, a high density of dislocations (order of 10^{12}) which is inherited from the initial martensitic structure undergoes recovery, recrystallization and grain growth, resulting in subgrain formation in the ferrite areas. In addition, subsequent quenching from the two phase field results in the generation of a high density of fresh dislocations in the ferrite region near the martensite islands. These dislocations result from the volume expansion of 3-4% and the shape change associated with

the austenite-to-martensite transformation. It is well known that the origin of low yield strength and continuous yielding behavior, which are the characteristics of dual phase steels, are attributed to these fresh, mobile dislocations (30,31).

B. Intercritical Annealing Process

In the intercritical annealing process, the starting microstructure is mainly hypoeutectoid ferrite with pearlite. Upon two phase annealing, austenite nucleates at the ferrite-cementite boundary in pearlite and grows at the expense of the pearlite and ferrite (75,76). Thus, the resulting structure after quenching to room temperature is fine globular martensite along the ferrite grain boundaries as shown in Fig. 17. The volume fraction of martensite is essentially the same as that of the intermediately quenched counterpart at the same two phase annealing temperature. Careful transmission electron microscopy studies also showed that the substructures of ferrite and martensite are very similar to those of the intermediately quenched specimens.

C. Controlled Rolling and Step Quenching Processes

For both heat treatments, the initial phase before two phase annealing is austenite. Upon decreasing the temperature to the two phase region, ferrite nucleates at the prior austenite grain boundaries and grows into the austenite (77,78). The microstructure thus depends on the prior austenite grain size.

Figure 18 shows the dual-phase microstructure in the alloys S and M1 developed by the step quenching process. In these scanning electron micrographs, the gray areas correspond to the martensite phase and the darker background to the ferrite phase. The microstructural features are two phase aggregates of large, blocky shaped martensite islands in the coarse ferrite matrix, which show the influence of the coarse austenite grain size before two phase annealing.

For the controlled rolling process, the second phase is more or less unidirectionally aligned in the fine grained ferrite matrix. A typical microstructure of dual-phase steels, developed in this process is shown in Figs. 19 and 20. During the controlled rolling process, the coarse austenite obtained by soaking in the austenite region is broken into small recrystallized austenite grains through deformation in the austenite recrystallization region. By continuous deformation at a lower austenite temperature, the fine austenite grains are elongated with the deformation bands in the austenite interior. During cooling through the Ar_3 temperature and finish rolling in the $(\alpha+\gamma)$ phase, just below the Ar_3 temperature, the nucleation of ferrite occurs exclusively at deformation bands as well as at elongated austenite grain boundaries leading to a fine grained structure. When the finish rolled rod is directly quenched into agitated iced brine, a dual-phase structure is produced as shown in Fig. 19. Transmission electron microscopy studies revealed that the nature of the second phase is predominantly dislocated lath

martensite. The ferrite areas of dual-phase steels produced by the controlled rolling process consist of fine recrystallized ferrite as shown in Fig. 21.

4.2.2 Drawn Microstructure

To study the structure of highly deformed dual-phase steels by the wire drawing process and to correlate the relationship between the mechanical properties and microstructure of as-drawn dual-phase steel wire, the microstructural development in longitudinal and transverse sections for various diameters of dual-phase steel wire were examined with the scanning and transmission electron microscopes.

The progression of the dual-phase structure as the reduction in area by wire drawing was increased up to 97% or a true drawing strain up to 3.6 is shown in Fig. 22. In these scanning electron micrographs, the brighter phase is martensite in the darker background of the ferrite matrix. The initial dual-phase microstructure (Fig. 22A) was produced by the intercritical annealing process to produce equiaxed martensite particles, thus simplifying the deformation studies. These micrographs clearly show that both the ferrite and the martensite phases in the dual-phase steels deform well, but to greatly varying degrees. In the early stages of plastic deformation of dual-phase steels, strong martensite particles do not deform with the soft ferrite matrix. As deformation proceeds further, mobile dislocations in the ferrite

matrix impeded by the martensite particles will start to cut through the semi-coherent martensite particles on the slip systems that are common to ferrite and martensite, leading to the deformation of the martensite particles. Fig. 22B shows that all of the martensite particles were aligned with the wire axis after being drawn to a true strain of 1.2 or 70% reduction in area. However, many of the smaller particles were still equiaxed, indicating that they had not begun to deform at this point.

Figure 23 shows the microstructures of drawn dual-phase steel wire on a longitudinal section at a drawing strain of 3.6 or after 97% reduction in area. The initial microstructure before wire drawing was produced by the intermediate quenching, the intercritical annealing and the controlled rolling processes to obtain fine grained dual-phase steels. These micrographs show again that the ferrite and martensite phases in the fine grained dual-phase steels deform well. Figures 23B and 23C show that there are more non-deformed martensite particles in the drawn structures developed from the intercritically annealed and controlled rolled dual-phase steels than that of the intermediately quenched specimen shown in figure 23A. This behavior presumably results from the difference in shape of the martensite particles, the crystallographic relationship between the martensite and ferrite phases, and the substructure of martensite, which will be discussed later.

The drawn structure on a longitudinal section at a drawing strain, 2.8 of the coarse dual-phase steel produced by the step quenching process is shown in Fig. 24. This scanning electron micrograph clearly shows large void formations at the interface between the martensite particles and the ferrite matrix. These voids that form at the ferrite-martensite interface during wire drawing will eventually coalesce to cause failure at the die exit during subsequent drawing steps.

In order to assess the strain undergone by each constituent, i.e., ferrite and martensite phases during wire drawing deformation, microhardness testing was done on the transverse cross section of drawn wire of various diameters. The microstructure of the step quenched specimen was sufficiently coarse to allow accurate microhardness measurements of the individual phase after wire drawing. The Vickers microhardness value of each ferrite and martensite phase as a function of true drawing strain is presented in Table 8 and is plotted in Figs. 25 and 26.

These figures clearly demonstrate that the hardness of the ferrite increases rapidly at the early stage of deformation, while the hardness of the martensite is slightly increased. However, at the later deformation stage, the hardness value of the martensite starts increasing with less increase in ferrite value. Evidently, it is implicit that the deformation is concentrated first in the ferrite matrix, causing it to flow around the martensite particles. While reaching its maximum capacity for being strained, the ferrite

matrix obviously transfers strain across the ferrite-martensite interface leading to deformation of the martensite islands. Therefore, strain is distributed more uniformly, resulting in superior formability of the dual-phase steels.

The plastic deformation of iron at room temperature begins with formation of fairly straight dislocation lines if the strain is less than 1% (79,80). After 1% strain, interactions of dislocations occur and dislocations begin to cluster inside individual grains, and these clusters eventually join together to form a cell structure as the amount of deformation is increased. Cells can be seen after about 3.5% strain. After more than about 9% strain, the substructure consists of well-developed cells separated by boundaries with a high density of dislocation tangles called cell walls. These dislocations are believed to cluster into cell walls in order to decrease the elastic energy of the system (81-83). As the plastic strain increases during wire drawing, the cells begin to elongate along the drawing direction and decrease in scale whereas the misorientation between cells increases. At this point, the flow stress of the system is found to be linear with d^{-m} where d is the scale of the cellular substructure and m is ½ or 1, depending mainly on the nature of the substructure (84-87).

When longitudinal sections of the drawn wires were observed in the transmission electron microscope, the elongated cellular substructure developed in the direction of drawing, as expected. The cell dimension perpendicular to the drawing direction was

observed to decrease with increasing drawing strain, resulting in a corresponding increase in strength of the as-drawn dual-phase steel wire.

Figure 27 is a typical transmission electron micrograph in a longitudinal section of a drawn dual-phase steel wire after a 94% reduction in area, i.e., at a drawing strain of 2.8. The elongated darker areas correspond to the deformed martensite phases and the lighter areas to the deformed ferrite matrix. The higher magnification view of the deformed ferrite and martensite phases are also shown in Fig. 28. It is noted from these micrographs that the highly deformed ferrite flows around the martensite particles and develops in cellular substructures approximately 1200Å wide aligned with the wire axis, whereas the cellular substructure of the deformed martensite is less defined in comparison with those of the deformed ferrite. Another example of a heavily deformed dual-phase microstructure is shown in Fig. 29, which shows that the deformed martensite phase consists of a much finer cellular substructure when compared to those of the deformed ferrite matrix. This particular microstructure was found in the intermediately quenched specimen after a 97% reduction in area by wire drawing. The delay of cellular substructure formation and its fine scale in the deformed martensite phase seems to be due to a higher "lattice friction stress" (inherent lattice resistance to dislocation motion) in the martensite, which is predicted by Holt's theory of dislocation cell formation (82). As in most BCC materials (88,89), it was also found

that dual-phase steels develop a strong <110> texture during wire drawing as shown in Fig. 30.

In BCC crystals of a <110> orientation like dual-phase steel wires, two of the <111> slip directions lie perpendicular to the wire axis so that slip involving these two directions cannot contribute to the imposed elongation and reduction of the wires. Slip in the other two <111> directions permits the necessary elongation, but can only cause a thinning of the cells in one of their transverse dimensions, leading to plane strain on a local scale instead of axisymmetric flow. As a result, the cells must curl around each other to maintain contact with one another, resulting in a curved and ribbon shaped cell structure in the transverse sections (86,88,89).

The wavy appearance on a transverse section due to the predominant <110> texture developed in the dual-phase steel wire was observed in the scanning electron microscope (Fig. 31). It was also observed in the transmission electron microscope that the cellular substructure became curved and ribbon shaped in a transverse section of the drawn wires (Fig. 32).

4.3 Mechanical Properties

4.3.1 Initial Properties

As already mentioned, the tensile testing of as-heat treated steels was conducted at room temperature using subsize cylindrical tensile specimens of 0.5 inch gauge length (Fig. 11). All of the

tensile stress-strain curves obtained were typical of the plastic flow behavior of dual-phase steels (Fig. 2); the yield is continuous and the initial rate of work hardening is high.

The room temperature tensile properties of the 2% Si dual-phase steels with different martensite morphology (related to different heat treatments) are summarized in Table 4A. Fig. 33 shows the variation of yield and tensile strengths of these dual-phase steels as a function of martensite volume fraction. The general trend shown in this figure is that the strength of dual-phase steel follows the law of mixtures, increasing linearly with the volume fraction of martensite, as demonstrated in many dual-phase systems (21-24). From this figure, one also notes that the ultimate tensile strength values of the silicon containing dual-phase steels are determined to a large extent by the volume fraction of martensite, not by the martensite morphology. However, the comparison of the 0.2% offset yield strengths reveals some difference for the dual-phase steels developed by different heat treatments when the amount of martensite is similar. The specimens subjected to the controlled rolling and step quenching processes are characterized by higher yield strength compared to the specimens given the intermediate quenching or intercritical annealing treatments, although the ultimate tensile strengths are similar.

The variations of uniform and total elongations with respect to volume fraction of martensite for the silicon containing steels are plotted in Fig. 34, demonstrating the validity of the two phase

mixture rule for elongation. It is also noted from this figure that the step quenched specimens with coarse martensite particles result in very poor uniform and total elongation compared to the other microstructures at the same volume fraction of martensite.

The tensile properties of the manganese containing dual-phase steels produced by different heat treatments, but each with similar volume fraction of martensite, are listed in Table 4B and are plotted in Figs. 35 and 36. From the table and plots, one can see that the step quenched specimen with coarse, blocky microstructure has the lowest yield and ultimate tensile strengths, and also the lowest ductility. These results are in agreement with those previously published (90).

An important observation was that the step quenched silicon containing steel shows higher yield strength than the intermediately quenched or intercritically annealed specimens at the same amount of martensite as mentioned above. In contrast, the manganese containing steel given the step quenching process has a lower yield strength than other dual-phase steels. This difference will be discussed later in the next chapter. It is noted from Table 4 that the silicon containing dual-phase steels have better combinations of strength and ductility than the manganese containing dual-phase steels, which is consistent with the results previously reported(57,91,92).

The fracture surface of broken tensile specimens was examined by a scanning electron microscope and microfractographs are shown in

Fig. 37. For the specimens given the intermediate quenching treatment, the entire fracture surface revealed the typical 'cup and cone' ductile aspect of fracture during tensile testing, as shown in Fig. 37A. The fracture surfaces of controlled rolled and intercritically annealed specimens were found to exhibit similar ductile fracture. By contrast, in the step quenched specimens having a coarse dual-phase microstructure, cleavage fracture predominated as revealed by well defined facets, although some isolated areas of dimple fracture were found (Fig. 37B).

4.3.2 Drawing Properties

The drawing limit for all the steels corresponds to the maximum drawing strain the wire can sustain before the repeated occurrence of breakage at the die exit. The drawability for the various dual-phase steels based on the drawing limit is listed in Table 5. The role of the morphological factors on the drawability can be found by comparing the different specimens subjected to the different heat treatments. The dual-phase steels with fine, fibrous martensite particles produced by the intermediate quenching or the controlled rolling process show the best drawability, followed by intercritically annealed specimens. The step quenched specimens with a coarse microstructure are shown to have the poorest drawing properties. A comparison of the three intermediately quenched silicon containing alloys (specimens SIQ2, SIQ2, SIQ3) shows that the drawing limit decreased with the volume fraction of martensite.

One can also notice that the manganese containing dual-phase steel has a poor drawability compared to the silicon containing steel given the same heat treatment.

4.3.3 Drawn Properties

Table 6 lists the tensile properties of the drawn wires at a drawing strain of 0.44 and indicates that 0.2% offset yield strength is almost the same as the tensile strength. The tensile strengths of the dual-phase steel wires with initially different microstructures and compositions at different drawing strains are summarized in Table 7. This tensile data shows that dual-phase steels produced by the intermediate quenching process or the controlled rolling process could be drawn up to a drawing strain of 6 for higher tensile strength levels of 380-400 ksi (2620-2760 MPa)

The variation of the tensile strength of the 2% Si dual-phase steel wire given the controlled rolling process with respect to the wire diameter is plotted in Fig. 38. This figure shows that the tensile strength of the dual-phase steel wire increases linearly with $D^{-\frac{1}{2}}$ where D is the wire diameter after a rapid increase in early stages of deformation. This flow curve agrees well with results from wire drawing experiments by Embury and Fisher (84). We can also observe the similar trend in the manganese containing dual-phase steel wire given the controlled rolling process (Fig. 39).

Figure 40 shows the tensile strengths of dual-phase steel wires with different volume fractions of martensite as a function of wire

diameter. The silicon containing dual-phase steels before the drawing process were obtained by the intermediate quenching process. As mentioned already in Section 4.3.1, in the as-heat treated condition, the initial dual-phase steel with higher volume fraction of martensite has higher tensile strength. The difference in tensile strength generally remains the same throughout the range of the plot. This shows that the increase in tensile strength as a function of drawing strain was similar between the two specimens with different volume fractions of martensite.

A schematic of the drawing procedure and resulting tensile strengths for both a low carbon dual-phase steel with fine, fibrous microstructure in this investigation and a conventional high carbon pearlitic steel wire is shown in Fig. 41 for comparison. One notes that three patenting treatments may be required for the high carbon pearlitic steel wire (dashed line) to produce a tire cord, whereas only an initial heat treatment is required in the low carbon dual-phase steel case (solid line). This results in a reduction in the complexity of the operation as well as reductions in production cost and energy consumption. Consequently, dual-phase steels with fine, fibrous martensite particles show high promise as a new economical starting material for cold drawing into high tensile strength wires.

5. DISCUSSION

5.1 Correlation between Initial Microstructure and Tensile Properties

Empirically, the mechanical properties of dual-phase steels can be understood in terms of a composite consisting of a ductile matrix (ferrite) and a strong second phase (martensite). Therefore, the important metallurgical parameters affecting the mechanical properties of the dual-phase steels are: (1) properties of the ferrite and martensite phases, (2) size, shape and distribution of martensite in the ferrite matrix, and (3) volume fraction of martensite. These structural features are determined by the annealing temperature in the ($\alpha+\gamma$) region, the transformation path and the chemical composition of the alloy.

The tensile test data for the as-heat treated dual-phase steels listed in Table 4 and Fig. 33 confirms the results of previous works (21-24) that the tensile strength of a dual-phase steel is to a first approximation linearly dependent upon the martensite volume fraction by the two phase mixture rule,

$$\sigma = \sigma_m V_m + \sigma_\alpha (1 - V_m)$$

where V_m is the martensite volume fraction, σ_m is the ultimate tensile strength of the martensite, and σ_α is the stress carried by the ferrite matrix when the dual-phase steel is strained to its

ultimate tensile stress. Even if this mixture rule describes the extreme case where the strong phase particles are continuous and unidirectionally aligned in the direction of the applied stress, it is confirmed empirically that this equation holds as a fairly good approximation of the tensile behavior of the dual-phase steels. However, it was noted that suitable modifications which take account of the size, shape and distribution of the martensite particles are necessary for more quantitative correlations (93).

From Fig. 33, it is clear that, in the 2% Si dual-phase steels, the step quenched and the controlled rolled specimens show higher yield strength compared to the intermediately quenched specimens, although the tensile strengths are similar at approximately the same volume fraction of martensite. Contrarily, in the manganese bearing dual-phase steels with similar volume fraction of martensite (Fig. 35), the specimen given the step quenching process is characterized by lower yield and tensile strengths compared to the intermediately quenched or the intercritically annealed specimens, which is consistent with the result previously reported(90).

Earlier experimental studies on dual-phase steels showed that the yield strength is primarily determined by the flow strength of ferrite matrix, which is controlled by the mean free path in the ferrite according to the Hall-Petch equation (30). Therefore, the step quenched specimens with a coarse microstructure exhibit a lower yield strength compared to the specimens with a fine microstructure, produced by the intermediate quenching process or the intercritical

annealing process. This is verified in the present investigation for the 1.5% Mn dual-phase steels. However, the reverse result was found in the silicon containing dual-phase steels, which is contrary to the Hall-Petch equation. As a plausible explanation, it is possible that the lower yield strength in the silicon bearing specimen with a fine microstructure is related to the softening of the ferrite matrix.

Romig and Salzbrenner (94) investigated the partitioning of silicon between the ferrite and martensite phases in the intermediately quenched or the step quenched dual-phase steels of Fe-1.75% Si-0.09% V-0.1% C. For alloys given the intermediate quench treatment, it was found that the martensite to (ferrite + austenite) transformation proceeds under classical diffusion control (95,96), thus giving rising to more partitioning of silicon in the ferrite phase. Mathematical descriptions of such isothermal diffusion controlled transformations have been presented in the literature (97-99). Conversely, during the step quenching treatment, the austenite to (ferrite + austenite) reaction proceeded purely under carbon control. Thus, carbon partitioned between the ferrite and the austenite, but the silicon did not. This observation led to the formulation of the paraequilibrium or the no-partition local equilibrium condition (100,101). It is apparent, therefore, that the intermediately quenched specimen has more silicon content in the ferrite than the step quenched specimen. Because of the repellent interaction between silicon and carbon

(102), silicon forces carbon atoms to migrate from the ferrite phase and this depletion of carbon in turn softens the ferrite in the intermediately quenched dual-phase steel. As a result, the intermediately quenched specimen exhibits a lower yield strength compared to the step quenched specimen although the former has a smaller mean free path. It should be noted that since carbon is such an effective solid solution strengthening element (approximately 50 times more effective than silicon), even small changes in the solubility of carbon are likely to affect the strength of the ferrite phase.

Supporting evidence of the repellent interaction between silicon and carbon is available from several sources. Darken (103) investigated the silicon-carbon interaction using a diffusion couple fabricated from a high silicon steel and a plain carbon steel, both with similar carbon contents. After a high temperature anneal for a period of days, carbon had diffused from the high silicon steel to the plain carbon steel, significantly raising the carbon content of the latter. It has been reported that the maximum solubility of carbon in ferrite decreases in the presence of silicon by Petrova et al. (104).

As shown in Figs. 34 and 36, specimens with a coarse dual-phase microstructure produced by the step quenching exhibit much smaller values of elongation and reduction in area than other specimens with a fine microstructure at the similar volume fraction of martensite. Fig. 37 also shows that the step quenched specimen fractured

primarily by cleavage indicating premature failure of the system at the early stage of deformation, while the fracture surface of the dual-phase steel with a fine microstructure contains only a dimple structure, typical of ductile shear failure.

In the early stage of plastic deformation of a dual-phase steel, plastic flow starts in the soft ferrite while the martensite remains elastic and mobile dislocations in the ferrite are impeded by the adjacent martensite particles. As further deformation proceeds, the dislocation density increases rapidly, giving rise to dislocation tangles at the martensite-ferrite interfaces. In this way, stresses are built-up in the ferrite regions adjacent to the martensite particles. Thus, these localized deformation and/or stress concentrations in the ferrite lead to fracture of the ferrite matrix which occurs by cleavage or void nucleation and coalescence depending on the microstructure of the dual-phase steel.

For dual-phase steel with a coarse microstructure, the average spacing between the martensite particles is large. Thus, during plastic deformation, the number of dislocations and stress concentrations in the ferrite region near the martensite particles increase rapidly, leading to void formation at the early stage of plastic deformation. However, the fine dual-phase structure has smaller spacing between martensite particles than the coarse microstructure at the same volume fraction of martensite. As a result, the density of dislocations and stress concentrations at the ferrite-martensite interface decrease. Thus, void formation occurs

at the later stage compared to the dual-phase steel with coarse microstructure.

Initial voids may grow through only one or two ferrite grains to produce microcracks (105) or they may propagate throughout the ferrite phase causing failure of the specimen depending on the microstructure. Whether or not the void extends beyond the microcrack stage is determined by the mean free path of the specimen. The fracture stress of a specimen which fails predominantly by cleavage fracture is proportional to $d^{-\frac{1}{2}}$, where d is the mean free path (106).

In the dual-phase steels given the intermediate quenching process or controlled rolling process, the mean free path is very small. Therefore, microcracks, if they form, are obscured by the extensive plastic deformation associated with the shear fracture of the ferrite. The fracture of these dual-phase structures occurs by void nucleation and coalescence due to localized deformation in the ferrite after large amounts of plastic deformation. In the step quenched specimens with the large mean free path, cleavage cracks propagate throughout the ferrite, resulting in premature failure with small amounts of plastic deformation.

This considerable difference in the void formation and propagation between the coarse and the fine dual-phase structures can explain a significant difference in the ductility of the as-heat treated dual-phase steels at room temperature. The foregoing discussion emphasizes that the ductility of dual-phase steel of a

given strength is largely dependent upon its morphology and grain size.

5.2 Drawability

Since a large part of the tensile strength of the dual-phase steel wire results from the cold drawing, the important factor is the maximum amount of cold drawing which can be put into the as-heat treated dual-phase steel to boost the strength. Drawability for several dual-phase steels studied in the present investigation is listed in Table 5, showing the microstructural influence on the drawing behavior of dual-phase steels.

In general, the fine, fibrous microstructure produced by the intermediate quenching process or the controlled rolling process shows the best drawability. In contrast, the coarse microstructure given the step quenching treatment has the poorest drawing limit. The drawability of the intercritically annealed specimen is intermediate. The role of the martensite volume fraction on the drawability can be found by comparing the three intermediately quenched silicon containing specimens (SIQ1, SIQ2, SIQ3), which shows that the drawing limit of the specimen with the lowest volume fraction of the martensite (SIQ1) is the highest. This may have been due to the fact that the volume fraction of the ductile ferrite matrix is the highest in this case. The role of the alloying element on the drawability is shown by the lower drawability of the

manganese containing dual-phase steel compared to the silicon containing steel given the same heat treatment.

As mentioned before, during the wire drawing process, the ferrite and martensite in the dual-phase steels deform continuously, but to greatly varying degrees. This difference in strain results in void formation at the ferrite-martensite interface, eventually leading to the ultimate failure of the wire at the die exit during subsequent drawing steps.

Generally, current criteria for void formation or decohesion at the interface of the hard particles in a ductile matrix are based upon consideration of local elastic energy storage, and normal stress at the particle-matrix interface (107-109). The elastic energy criterion is that the elastic energy which is stored in the plastically non-deformable particle and released during decohesion must be greater than or equal to the increase in energy due to the newly formed free surfaces. This is why the particle-matrix interfacial energy has such a strong influence on the nucleation role of voids (110). This criterion is more easily satisfied for large particles than for small particles (109). The second criterion is that the stress at the particle-matrix interface must exceed the tensile strength of that interface before the stored elastic energy can be released to form two new surfaces.

The inferior drawability in the step quenched specimen compared to other heat treated specimens can be solely attributed to its coarse microstructure. From a continuum mechanics viewpoint, this

is expected since the coarse martensite geometry in the coarse ferrite causes more severe inhomogeneous deformation and restricts initial plastic flow to a smaller fraction of the total volume of the ferrite matrix. Therefore, the energy criteria for void nucleation was more easily satisfied for the large martensite particles. Also, void propagation will occur at a faster rate with less plastic strain, as mentioned in the previous section.

As shown in Table 5, the drawability of the intermediately quenched specimen was higher than that of the corresponding intercritically annealed specimen (e.g., SIQ1 and SIA1). Since they were the same alloy annealed at the same temperature, there should be no differences in their martensite volume fractions and properties. Thus, these were not influencing factors. This difference in drawabilities between the two specimens can be related to their different void formation tendencies because of different microstructures, such as the nature of the ferrite-martensite interfaces and the shape of the martensite particles. Fig. 23 shows the drawn dual-phase microstructures of the intermediately quenched and the intercritically annealed specimens at a drawing strain of 3.6. It is apparent that the microstructure produced by the intercritical annealing process (Fig. 23B) is more susceptible to void formation than the microstructure developed by the intermediate quenching process (Fig. 23A).

As shown by Koo and Thomas (111), the martensite particles in the intermediately quenched specimen generally have the same

crystallographic orientation as the surrounding ferrite matrix. During two phase annealing in the intermediate quenching process, the austenite nucleates at and grows along the prior martensite lath boundaries and forms the acicular austenite as mentioned before. Upon quenching, the acicular austenite tends to transform back to the same variant as the previous martensite (112), which by this point has recovered or recrystallized to form the ferrite matrix. As a result, the crystallographic orientation of both the martensite and the ferrite is nearly the same and the ferrite-martensite boundaries are coherent or of very low angle. Thus, void formation at the ferrite-martensite interface is more difficult during wire drawing. This is because a low angle boundary is generally of low energy (113) and, as mentioned earlier, the interfacial energy has a very strong influence on void formation.

In contrast, the ferrite-martensite interface in the intercritically annealed specimen is generally of high angle at least part way around the martensite particles because the particles generally lie on ferrite grain boundaries or at grain junctions. Thus, the martensite particles can have a low angle interface with at most one of the neighboring ferrite grains and must have high angle boundaries with the rest. Therefore, void formation at the ferrite-martensite interface should be more difficult in the intermediately quenched specimen during wire drawing than in the intercritically annealed specimen.

In addition to the advantage of a lower energy ferrite-martensite interface, the martensite particles in the intermediately quenched specimen are acicular, whereas those in the intercritically annealed specimen are roughly equiaxial. Since fiber composite theory states that an elongated particle has a better load transfer with the matrix (43), there is less tendency for void formation in the intermediately quenched specimen. These differences in the nature of the ferrite-martensite interface and the shape of the martensite particles can explain the increase in deformability of martensite particles and better drawability for the intermediately quenched specimen than for the intercritically annealed specimen.

The specimen subjected to the controlled rolling process has the high angle boundaries between the ferrite and martensite phases similar to the intercritically annealed specimen. Nevertheless, the former reveals better drawability than the latter. This may have been due to a more favorable martensite morphology in the former case. The martensite particles of the specimen given the controlled rolling process are finer and fibrous compared to those of the intercritically specimen. Therefore, there is less tendency for void formation at the ferrite-martensite interfaces, accounting for better drawability for the controlled rolled specimen.

The inferior drawability of the manganese containing dual-phase steel to the silicon containing steel given the similar heat treatment could be explained as follows. In experimental results of substitutional alloying element partitioning in dual-phase steels

(114), it was found that manganese partitions more in the martensite region, especially adjacent to the ferrite-martensite interface, than in the ferrite region, whereas silicon partitions more in the ferrite region than in the martensite region. In the manganese containing steel, the hardness of martensite adjacent to the ferrite-martensite interface is enhanced due to the segregated manganese elements while that of ferrite is reduced. This may induce greater plastic incompatibility between the ferrite and the martensite, resulting in void formation at the interface at a relatively lower drawing strain in this case. However, the silicon containing steel shows an opposite tendency to that of the manganese steel, and so the difference of the hardness between ferrite and martensite is much lower. Therefore, it can be suggested that a silicon containing dual-phase steel has better drawability than a manganese steel given the similar heat treatment. However, the manganese steel given the controlled rolling process shows similar drawability to that of the silicon steel because there is less tendency of manganese partitioning between ferrite and martensite in this case.

In addition to the effect of alloying element partitioning, the drawability difference could be related to the difference in the martensite morphology between the silicon and the manganese containing specimens given the intermediate quenching process as mentioned in Section 4.2.1A. As shown in Fig. 14, while the martensite particles in the silicon containing dual-phase steel are

discontinuous throughout the matrix, those of the manganese containing dual-phase steel form a continuous network along the prior austenite grain boundaries as an inevitable product of the phase transformation in this system with an acicular morphology in the interior of the prior austenite grains. These large martensite particles along the prior austenite grain boundaries are preferred void nucleation sites since they do not have the optimum interfacial relationship with the surrounding ferrite matrix. Once voids nucleate at these sites, they could easily coalesce in a relatively early stage prior to appreciable plastic deformation of the ductile ferrite matrix since they form a continuous network.

As a plausible explanation for the absence of martensite particles along the prior austenite grain boundaries observed in the silicon containing dual-phase steels, two possibilities were suggested by Koo (30). First, it is likely that the prior austenite grain boundary can be decorated by the formation of ferrite allotriomorphs during quenching after solution treatment. This occurs since silicon is one of the most potent alloying elements which increase the rates of nucleation and growth of proeutectoid ferrite allotriomorphs (115). As a result, the initial martensite structure prior to the two phase annealing may be associated with a thin layer of ferrite allotriomorph along the prior austenite grain boundary. As a consequence, upon subsequent annealing in the two phase region, the ferrite phase inherited from the initial martensite structure may prevent the nucleation and growth of

austenite along the prior austenite grain boundaries. The second possibility is related to the occurrence of silicon segregation along the prior austenite grain boundaries in the initial martensitic structure prior to the two phase annealing. Therefore, during two phase annealing, austenite nucleation at the prior austenite grain boundaries will be prevented by the repellent interactions between carbon and preoccupied silicon atoms at the boundaries (102), and will occur only at the initial martensite lath boundaries.

In addition to the role of various metallurgical parameters on the drawing behavior of dual-phase steel, as discussed above, the control of martensitic substructure is particularly important for superior drawability. If the dual-phase microstructure contains twinned plate martensite (Fig. 42), there is an increase in the void formation tendency between the ferrite-martensite interface during the drawing process (Fig. 43) since the twinned martensite is non-deformable. Therefore, the presence of twinned martensite is detrimental to the drawability of a dual-phase steel and leads to the failure of the dual-phase steel in an early stage of plastic deformation. To prevent the occurrence of the twinned martensite, the carbon content of the austenite phase should be approximately less than 0.4 wt.% during two phase annealing. In addition, the quenching after two phase annealing or finish rolling should be rapid enough to prevent further austenite pool shrinkage or decomposition prior to its transformation to martensite, which would

result in high carbon plate martensite or carbide formation at the edge of a predominantly lath martensite particle.

5.3 Drawn Properties

Over the last two decades considerable effort has been directed towards understanding the development of microstructure and the strengthening mechanism in metals deformed at large strains, and the field has been extensively reviewed most recently by Gil Sevillano et al. (116). In the earlier work for various ferrous steels by Embury and Fisher (84), they found that a cellular dislocation substructure is developed during wire drawing and the nature of this dislocation substructure consists of elongated cells almost free from dislocations separated by walls of densely tangled dislocations. These walls are known to block the movement of slip dislocations in a manner analogous to grain boundaries and are referred to as cell walls or substructural barriers. It was noted that, as the drawing strain is increased, the mean distance between the cell walls perpendicular to the drawing direction, i.e., the cell dimension is progressively reduced. Quantitative measurements of the flow stress and the cell dimension indicated that the flow stress of heavily deformed material, σ_f, can be related to the spacing between the cell walls by an equation of the Hall-Petch type:

$$\sigma_f = \sigma_0 + k\, d^{-\frac{1}{2}}$$

where d is the dimension of the cell structure and k is a constant which includes a geometrical factor relating the mean slip distance to the observed values of d. Embury and Fisher suggested that the spacing between cell walls (d) normal to the wire axis is continuously reduced and remains proportional to the wire diameter (D) so that one can write:

$$d_o/d_\varepsilon = D_o/D_\varepsilon$$

where the subscripts refer to initial dimensions and those after a true drawing of ε. Therefore, the flow stress of the cold drawn wire is also proportional to the reciprocal of the square root of the drawn wire diameter ($D_\varepsilon^{-\frac{1}{2}}$).

The model proposed by Embury and Fisher is restrictive in the sense that it assumes that the number of cells remains unchanged during the total range of wire drawing and the cells are elongated axisymmetrically, whereas in fact the deformation mode corresponds more nearly to plain strain due to textural effects (86). Langford and Cohen have examined this premise in detail by carefully investigating the scale and morphology of the cell structure in drawn pure iron in both the longitudinal and transverse sections. It was observed in the transverse section that the cells become curved and ribbon shaped due to plain strain flow imposed by the <110> wire texture and the relationship of flow stress to the inverse of the cell dimension (d^{-1}) is obeyed over a wide range of drawing strains.

However, it has been shown that, for two-phase materials, the <110> wire texture has no net effect on the average scale of cells (117). This is because, although the <110> wire texture causes the swirled appearance of the microstructure on transverse sections, the resulting strength inhomogeneities cause further inhomogeneous deformation which defeats the effect of the internal shape change on the scale of the microstructure, converting the plane strain elongation to axisymmetric elongation. Therefore, the correlation observed between the strength of drawn wire (σ) and the cell dimension (d) is of the form, $\sigma \propto d^{-\frac{1}{2}}$, which is similar to the equation proposed by Embury and Fisher, and the average cell dimension is simply reduced in direct proportion to the change in wire diameter.

The variation in tensile strength in dual-phase steel wire with respect to the wire diameter is shown in Figs. 38-40. These figures show that the tensile strength is inversely proportional to the square root of the wire diameter ($D^{-\frac{1}{2}}$) after a rapid increase in early stages of deformation. As shown in Figs. 25 and 26, both the ferrite and martensite phases in dual-phase steel deform well with increasing drawing strain so that the cell dimensions of deformed ferrite and martensite are continuously decreased according to the macroscopic shape change of the wire. It is reasonable to suggest that the flow stress of deformed ferrite and martensite is governed by these relationships:

$$\sigma_{\alpha\varepsilon} \propto (d_{\alpha\varepsilon})^{-\frac{1}{2}} \propto (D_\varepsilon)^{-\frac{1}{2}} \quad \text{and} \quad \sigma_{m\varepsilon} \propto (d_{m\varepsilon})^{-\frac{1}{2}} \propto (D_\varepsilon)^{-\frac{1}{2}}$$

where $d_{\alpha\varepsilon}$ and $d_{m\varepsilon}$ are the cell dimensions of deformed ferrite and martensite, respectively, D_ε the wire diameter at a drawing strain of ε. Thus, it is anticipated that the tensile strength of dual-phase steel wire is related to the wire diameter by the relationship, $\sigma_\varepsilon \propto D_\varepsilon^{-\frac{1}{2}}$ since the flow stress of dual-phase steel wire follows the mixture rule (Fig. 40),

$$\sigma_\varepsilon = \sigma_{\alpha\varepsilon} V_\alpha + \sigma_{m\varepsilon} V_m$$

where V_α and V_m are the volume fractions of ferrite and martensite, respectively.

Figures 38-40 also show a rapid strain hardening in the early stages of deformation. This behavior presumably results because at the beginning of deformation, cell dimensions decrease more rapidly than they would if they were merely to follow the macroscopic shape change due to a higher cell multiplication rate in the low strain region. At large strains, however, the average cell dimension is simply reduced in direct proportion to the change in the wire diameter, if no dynamic recovery occurs.

As can be seen from Fig. 40, the dual-phase steel wire with higher martensite volume fraction had higher tensile strength, as expected. The difference in tensile strength generally remained the same throughout the range of the plot, showing that the strain hardening rate was similar for the dual-phase steels with different martensite volume fractions. In dual-phase steels, it has been

shown that the strain hardening rate increases linearly with the martensite volume fraction (23). Also, the strain hardening rate was found to be sensitive to the carbon content of the martensite phase, being substantially higher for steels with higher carbon content due to the greater plastic incompatibility of the harder particles with the ferrite matrix and from the higher residual stress associated with their lower transformation temperature.

From the Fe-C phase diagram (Fig. 7), it is noted that, during the two phase annealing, the carbon content of the austenite phase decreases as the annealing temperature increases, where the carbon content of the bulk material is constant. This means that the specimen with higher martensite volume fraction has lower carbon content in the martensite phase than that with lower martensite volume fraction. Thus, the increase of the work hardening rate with higher martensite volume fraction would compensate for the decrease of the work hardening rate with lower carbon content in the martensite. From this consideration, the similar work hardening rate of dual-phase steels of a given composition with different martensite volume fractions can be understood.

6. SUMMARY

The investigation has been aimed at designing desirable dual-phase steels for cold drawing into high strength wire. Based on the results of this research on the microstructure-mechanical property relationships of dual-phase steel and drawn wire from dual-phase steel, the major findings are summarized below.

1. Dual-phase steel can be designed and processed as an economical starting material for drawing into high strength steel wire.
2. The dual-phase steel of composition Fe-2% Si-0.1% C, which has been developed according to the selected design guidelines, was found to be the most promising material for drawing wire to high tensile strength.
3. This steel can be continuously drawn to strength levels found in commercial high carbon pearlitic steel wires without any intermediate patenting treatments during the drawing process. This results in a reduction in the complexity of the operation as well as reducing production cost and energy consumption.
4. This attractive dual-phase steel for drawing into high strength wire, which has a microstructure of fine, fibrous and disconnected lath martensite particles in fine ferrite matrix can be produced by either the intermediate quenching process or the controlled rolling process.

5. The intermediate quenching process consists of austenitizing and quenching to form 100% martensite, followed by two phase annealing and subsequent quenching. The martensite volume fraction can be varied by the two phase annealing temperature.
6. The controlled rolling process consists of deforming above and below the austenite recrystallization temperature after austenitizing, followed by finish-rolling in the two phase region and quenching. Processing variables such as the amount of deformation and the deformation temperature should be carefully controlled to obtain the optimum microstructure. This process is suitable for commercial rod mills provided a quenching system is available.
7. A very rapid quench after two phase annealing or finishing rolling is necessary to produce the desirable ferrite-lath martensite microstructure. Slow or delayed quenching can cause austenite pool shrinkage or decomposition above the Ms temperature, resulting in a region of microtwinned martensite or carbide at the edge of a predominantly lath martensite particle, which is undesirable for wire drawing.
8. From the study of as-heat treated dual-phase steels with different shape, size and volume fraction of martensite particles, the following observations were made:
   a) The volume fraction of martensite governs the strength and the ductility according to the two phase mixture rule, as previously demonstrated in many dual-phase steels.

b) In addition to the martensite volume fraction, the martensite morphology influences the tensile properties of dual-phase steel. A fine particle size of martensite is required to improve the ductility of dual-phase steels of a given strength.

9. From the study of the drawing behavior of dual-phase steels with different martensite morphologies and volume fractions, the following observations were made:

   a) The drawing limit is decreased as the martensite volume fraction increases.

   b) The drawability of dual-phase steel also depends on the shape, size, substructure of martensite and on the nature of the ferrite-martensite interface. A microstructure consisting of fine, fibrous lath martensite with coherent ferrite-martensite interfaces is desirable for higher drawability.

10. The tensile strength is linear with the reciprocal of the square root of the wire diameter (which is related to the scale of the cellular substructure) after a rapid increase in the initial stages of deformation.

11. The dual-phase steel wire with higher martensite volume fraction shows higher tensile strength levels throughout the range of various wire diameters investigated. However, the work hardening rate of drawn wire approaches a single value, independent of the martensite volume fraction.

ACKNOWLEDGEMENTS

The author would like to express his deepest appreciation to Professor Gareth Thomas for his continued guidance, encouragement and support throughout the course of this investigation. He also extends his sincere appreciation to Dr. R. M. Fisher, Center for Advanced Materials, Lawrence Berkeley Laboratory, for his valuable discussions and advice. Thanks are also due to Professor S. Kobayashi and Dr. R. M. Fisher for their critical review of this manuscript.

The author would like to thank former and present colleagues for their advice, assistance, and friendship necessary to complete graduate study. The technical assistance provided by the support staff of the Materials and Molecular Research Division of the Lawrence Berkeley Laboratory, especially J. Holthuis, D. Krieger, W. Wong and G. Pelatowski is gratefully acknowledged. Nippon Kokan K.K., Japan, graciously supplied the alloys used in this investigation. Special thanks are extended to M. M. Penton for typing this manuscript.

Finally, the author is grateful to his family, especially his wife, Bongsook, who showed her love and endurance during his graduate study.

This work was supported by the Director, Office of Energy Research, Office of Basic Energy Sciences, Division of Materials Sciences of the U.S. Department of Energy under Contract No. DE-AC03-76SF00098.

REFERENCES

1. H. E. McGannon (ed.), The Making, Shaping and Treating of Steel, 9th ed., United States Steel, Pittsburgh, PA (1971).
2. A. B. Dove (ed.), Steel Wire Handbook, Vol. 2, The Wire Association, Inc., Branford, CT (1968).
3. R. H. Hertzog, Wire (Oct. 1958), p. 1176.
4. J. A. Hubeli, Wire Journal (Nov. 1981), p. 82.
5. D. Lewis, Wire and Wire Products (Oct. 1957), p. 32.
6. K. Takeo et al., Tetsu-to-Hagane, Vol. 60 (1974), p. 2135.
7. A. Shummer, SEAISI Quart. (Oct. 1978), p. 6.
8. V. J. Vitelli, Wire Journal (July 1972), p. 53.
9. F. Pesche, M. Hollande, J. Le Quere and S. Tassin, Wire Journal International (July 1982), p. 86.
10. E. Forster and M. Klemm, Wire Journal International (May 1984), p. 56.
11. G. Thomas, Frontiers in Materials Techniques, M. A. Meyers and O. T. Inal (eds.), Elsevier Science Publishers B. V., The Netherlands (1985), p. 89.
12. A. H. Nakagawa and G. Thomas, Metall. Trans., Vol. 16A (1985), p. 831.
13. S. Hayami and T. Furukawa, Microalloying 75, Union Carbide Corp., New York, NY (1977), p. 311.
14. J. Y. Koo and G. Thomas, Mat. Sci. and Eng., Vol. 24 (1976), p. 187.

15. M. S. Rashid, SAE Preprint No. 760206, G. M. Corp., Warren, MI (1976).

16. A. T. Davenport (ed.), Formable HSLA and Dual-Phase Steels, TMS-AIME, Warrendale, PA (1979).

17. Dual Phase and Cold Pressing Vanadium Steels in the Automobile Industry, Proc. of Seminar in Berlin, Vanadium Intl. Tech. Comm. (1978).

18. R. A. Kot and J. W. Morris (eds.), Structure and Properties of Dual-Phase Steels, TMS-AIME, Warrendale, PA (1979).

19. R. A. Kot and B. L. Bramfitt (eds.), Fundamentals of Dual-Phase Steels, TMS-AIME, Warrendale, PA (1981).

20. B. L. Bramfitt and P. L. Mangonon, Jr. (eds.), Metallurgy of Continuous-Annealed Sheet Steel, TMS-AIME, Warrendale, PA (1982).

21. J. Y. Koo and G. Thomas, Metall. Trans., Vol. 8A (1977), p. 525.

22. R. G. Davies, Metall. Trans., Vol. 9A (1978), p. 671.

23. G. R. Speich and R. L. Miller, Structure and Properties of Dual-Phase Steels, R. A. Kot and J. W. Morris (eds.), TMS-AIME, Warrendale, PA (1979), p. 145.

24. J. Y. Koo, M. J. Young and G. Thomas, Metall. Trans., Vol. 11A (1980), p. 852.

25. P. K. Costello, M.S. Thesis, University of California, Berkeley, LBL-8628 (1978).

26. T. J. O'Neill, M.S. Thesis, University of California, Berkeley, LBL-9407 (1979).

27. R. H. Hoel and G. Thomas, Scripta Met., Vol. 15 (1981), p. 867.

28. J. S. Gau, J. Y. Koo, A. H. Nakagawa and G. Thomas, Fundamentals of Dual Phase Steels, R. A. Kot and B. L. Bramfitt (eds.), TMS-AIME, Warrendale, PA (1981), p. 47.

29. A. Nakagawa, J. Y. Koo and G. Thomas, Metall. Trans., Vol. 12A (1981), p. 1965.

30. J. Y. Koo, Ph.D. Thesis, University of California, Berkeley, LBL-6657 (1977).

31. J. M. Rigsbee and P. J. Van der Arend, Formable HSLA and Dual-Phase Steels, A. T. Davenport (ed.), TMS-AIME, Warrendale, PA (1979), p. 56.

32. C. L. Magee and R. G. Davies, Acta Met., Vol. 20 (1972), p. 1031.

33. J. M. Moyer and G. S. Ansell, Metall. Trans., Vol. 6A (1975), p. 1785.

34. G. Tither and M. Lavite, J. of Metals, Vol. 27 (Sep. 1975), p. 15.

35. W. C. Leslie and R. J. Sober, Trans. ASM, Vol. 60 (1967), p. 459.

36. K. R. Kinsman, G. Das and R. F. Hehemann, Acta Met., Vol. 25 (1977), p. 359.

37. B. Karlsson and B. D. Sundstrom, Mat. Sci. and Eng., Vol. 16 (1974), p. 161.

38. L. Anand and J. Gurland, Acta Met., Vol. 24 (1976), p. 901.

39. M. S. Rashid and E. R. Cprek, Formability Topics - Metallic Materials, ASTM STP 647, B. A. Niemeier, A. K. Schmieder and J. R. Newby (eds.), ASTM (1978), p. 174.

40. A. R. Marder, Metall. Trans., Vol. 12A (1981), p. 1569.

41. N. K. Balliger and T. Gladman, Met. Sci., Vol. 15 (1981), p. 95.

42. C. A. N. Lanzillotto and F. B. Pickering, Met. Sci., Vol. 16 (1982), p. 371.

43. G. E. Dieter, Mechanical Metallurgy, 2nd ed., McGraw-Hill, New York, NY (1976).

44. S. K. Das and G. Thomas, Metall. Trans., Vol. 1 (1970), p. 325.

45. G. Thomas, Battelle Colloquium on Fundamental Aspects of Structural Alloy Design, R. I. Jaffee and B. A. Wilcox (eds.), Plenum Publishing Co. (1977), p. 331.

46. R. G. Davies, Metall. Trans., Vol. 9A (1978), p. 41.

47. M. R. Plichta and H. I. Aaronson, Metall. Trans., Vol. 5 (1974), p. 2611.

48. Microalloying 75, Union Carbide Corp., New York, NY (1977).

49. T. Tanaka, Intl. Metals Rev., No. 4 (1981), p. 185.

50. T. Tanaka, N. Tabata, T. Hatomura and C. Shiga, Microalloying 75, Union Carbide Corp., New York, NY (1977), p. 107.

51. I. Kozasu, C. Ouchi, T. Sampei and T. Okita, Microalloying 75, Union Carbide Corp., New York, NY (1977), p. 120.

52. J. J. Irani, D. Burton, J. D. Jones and A. B. Rothwell, Strong Tough Structural Steels, The Iron and Steel Institute, London (1967), p. 110.

53. P. L. Mangonon, Jr. and W. E. Heitmann, Microalloying 75, Union Carbide Corp., New York, NY (1977), p. 59.

54. P. E. Repas, Microalloying 75, Union Carbide Corp., New York, NY (1977), p. 387.

55. R. B. G. Yeo, A. G. Melville, P. E. Repas and J. M. Gray, J. of Metals, Vol. 20 (June 1968), p. 33.

56. J. E. Hilliard and W. S. Owen, J. Iron and Steel Inst., Vol. 172 (Nov. 1952), p. 268.

57. R. G. Davies, Metall. Trans., Vol. 10A (1979), p. 113.

58. G. Langford, P. K. Nagata, R. J. Sober and W. C. Leslie, Metall. Trans., Vol. 3 (1972), p. 1843.

59. R. F. Hehemann, Phase Transformation, ASM (1970), p. 410.

60. B. Avitzur, J. Eng. for Ind., Trans. ASME, Vol. 90, Series B, No. 1 (Feb. 1968), p. 79.

61. Z. Zimerman and B. Avitzur, J. Eng. for Ind., Trans. ASME, Vol. 92, Series B, No. 1 (Feb. 1970), p. 135.

62. B. Avitzur, Wire Journal (Nov. 1974), p. 77.

63. W. A. Backofen, Deformation Processing, Addison-Wesley, Reading, MA (1972).

64. R. M. Caddell and A. G. Atkins, J. Eng. for Ind., Trans. ASME, Vol. 91, Series B, No. 3 (Aug. 1969), p. 664.

65. S. Brandal and H. Valberg, Wire Journal International (Mar. 1982), p. 64.

66. T. Furukawa, M. Tanino, H. Morikawa and M. Endo, Trans. ISIJ, Vol. 24 (1984), p. 113.

67. H. Majors, Jr., Trans. ASME, Vol. 77 (1955), p. 37.

68. Annual Book of ASTM Standards, Designation E8-69, (1973), p. 196.

69. E. E. Underwood, Metals Handbook, 8th ed., Vol. 8, ASM, Metals Park, OH (1973), pp. 37-47.

70. E. C. Bain and H. W. Paxton, Alloying Elements in Steel, 2nd ed., ASM, Metals Park, OH (1961).

71. Metals Handbook, 8th ed., Vol. 8, ASM Metals Park, OH (1973).

72. G. Krauss and A. R. Marder, Metall. Trans., Vol. 2 (1971), p. 2343.

73. C. A. Apple, R. N. Caron and G. Krauss, Metall. Trans., Vol. 5 (1974), p. 593.

74. B. V. N. Rao, J. Y. Koo and G. Thomas, 33rd Annual Proc. Electron Microscopy Soc. America, Claitors, Baton Rouge (1975), p. 30.

75. C. I. Garcia and A. J. De Ardo, Metall. Trans., Vol. 12A (1981), p. 521.

76. G. R. Speich, V. A. Demarest and R. L. Miller, Metall. Trans., Vol. 12A (1981), p. 1419.

77. P. G. Shewmon, Transformation in Metals, McGraw-Hill, New York, NY (1969).

78. H. I. Aaronson, H. A. Domian and G. M. Pound, Trans. TMS-AIME, Vol. 236 (1966), p. 753.

79. A. S. Keh and S. Weissmann, Electron Microscopy and Strength of Crystals, G. Thomas and J. Washburn (eds.), Interscience, New York (1963), p. 231.

80. W. C. Leslie, The Physical Metallurgy of Steels, McGraw-Hill, New York, NY (1981).

81. F. R. N. Nabarro, Z. S. Basinski and D. B. Holt, Adv. Phys., Vol. 13 (1964), p. 193.

82. D. L. Holt, J. Appl. Phys., Vol. 41 (1970), p. 3197.

83. D. Kuhlmann-Wildorf and J. H. Van De Merwe, Mat. Sci. and Eng., Vol. 55 (1982), p. 79.

84. J. D. Embury and R. M. Fisher, Acta Met., Vol. 14 (1966), p. 147.

85. J. D. Embury, A. S. Keh and R. M. Fisher, Trans. TMS-AIME, Vol. 236 (1966), p. 1252.

86. G. Langford and M. Cohen, Trans. ASM, Vol. 62 (1969), p. 623.

87. A. W. Thompson, Metall. Trans., Vol. 8A (1977), p. 833.

88. J. F. Peck and D. A. Thomas, Trans. TMS-AIME, Vol. 221 (1961), p. 1240.

89. W. F. Hosford, Jr., Trans. TMS-AIME, Vol. 230 (1964), p. 12.

90. X. L. Cai, J. Feng and W. S. Owen, Metall. Trans., Vol. 16A (1985), p. 1405.

91. K. Nakaoka, K. Araki and K. Kurihara, Formable HSLA and Dual-Phase Steels, A. T. Davenport (ed.), TMS-AIME, Warrendale, PA (1979), p. 126.

92. K. Nakaoka, Y. Hosoya, M. Ohmura and A. Nishimoto, Structure and Properties of Dual-Phase Steels, R. A. Kot and J. W. Morris (eds.), TMS-AIME, Warrendale, PA (1979), p. 330.

93. M. J. Young, M.S. Thesis, University of California, Berkeley, LBL-6620, 1977.

94. A. D. Romig, Jr. and R. Salzbrenner, Scripta Met., Vol. 16 (1982), p. 33.

95. J. B. Gilmour, G. R. Purdy and J. S. Kirkaldy, Metall. Trans., Vol. 3 (1972), p. 3213.

96. A. D. Romig, Jr. and J. I. Goldstein, Metall. Trans., Vol. 9A (1978), p. 1599.

97. D. E. Coates, Metall. Trans., Vol. 4 (1973), p. 2313.

98. J. I. Goldstein and E. Randich, Metall. Trans., Vol. 8A (1977), p. 105.

99. A. D. Romig, Jr. and J. I. Goldstein, Metall. Trans., Vol. 12A (1981), p. 243.

100. H. I. Aaronson and H. A. Domain, Trans. TMS-AIME, Vol. 236 (1966), p. 781.

101. R. C. Sharma, G. R. Purdy and J. S. Kirkaldy, Metall. Trans., Vol. 10A (1979), p. 1129.

102. K. J. Irvine and F. B. Pickering, J. Iron and Steel Inst., Vol. 201 (1963), p. 944.

103. L. S. Darken, Atom Movements, ASM, Metals Park, OH (1951).

104. E. F. Petrova, M. I. Lapshina and L. A. Shvartsman, Metallovedenie I Term. Obrabotka, No. 4 (1960), p. 22; English transl. Henry Butcher No. 5379.

105. G. T. Hahn, B. L. Averbach, W. S. Owen and M. Cohen, Fracture, B. L. Averbach, D. K. Felbeck, G. T. Hahn and D. A. Thomas (eds.), J. Wiley, New York (1959), p. 91.

106. W. S. Owen and D. Hull, Refractory Metals and Alloys II, Interscience, New York (1962), p. 1.

107. E. Smith, Acta Metall., Vol. 14 (1966), p. 991.

108. L. M. Brown and W. M. Stobbs, Philos. Mag., Vol. 23 (1971), p. 1201.

109. A. S. Argon, J. Im and R. Safoglu, Metall. Trans., Vol. 6A (1975), p. 825.

110. J. R. Fisher and J. Gurland, Met. Sci., Vol. 15 (1981), p. 193.

111. J. Y. Koo and G. Thomas, Formable HSLA and Dual-Phase Steels, A. T. Davenport (ed.), TMS-AIME, Warrendale, PA (1979), p. 40.

112. J. I. Kim, C. K. Syn and J. W. Morris, Jr., Metall. Trans., Vol. 14A (1983), p. 93.

113. W. T. Read, Jr., Dislocations in Crystals, McGraw-Hill, New York, NY (1953).

114. M. Ohmura, Ph.D. Thesis, University of California, Berkeley, LBL-20590 (1985).

115. K. R. Kinsman and H. I. Aaronson, Metall. Trans., Vol. 4 (1973), p. 959.

116. J. Gil Sevillano, P. van Houtte and E. Aernoudt, Prog. Mat. Sci., Vol. 25 (1980), p. 69.

117. G. Langford, Metall. Trans., Vol. 8A (1977), p. 861.

Table 1. Alloy Compositions (wt. %)

Alloy	C	Si	Mn	P	S	Sol.Al	N	Fe
S	0.08	1.90	0.32	0.004	0.004	0.033	0.0015	Bal.
M1	0.10	-	1.55	0.005	0.003	0.019	0.0015	Bal.
M2	0.08	0.25	1.08	0.004	0.005	-	-	Bal.

Table 2. Phase Transformation Temperatures ($^{\circ}$C)

Alloy	Ac_1	Ac_3	Ar_1	Ar_3
S	780	1030	710	950
M1	725	845	570	710
M2	740	870	600	750

Table 3. Volume Fraction of Martensite

A. Fe-Si-C Alloy

Alloy	Specimen	Heat Treatment	Annealing Temperature (°C)	Volume Percent Martensite
S	SHR	HR	950†	~ 20
S	SIQ1	IQ	910	~ 20
S	SIQ2	IQ	960	~ 40
S	SIQ3	IQ	1000	~ 50
S	SIA1	IA	910	~ 20
S	SIA2	IA	960	~ 40
S	SSQ1	SQ	880	~ 30
S	SSQ2	SQ	920	~ 50
S	SM	-	-	~ 100

HR : Controlled Rolling Process

IQ : Intermediate Quenching Process

IA : Intercritical Annealing Process

SQ : Step Quenching Process

† : Finish Rolling Temperature

Table 3. Volume Fraction of Martensite

B. Fe-Mn-C Alloy

Alloy	Specimen	Heat Treatment	Annealing Temperature (°C)	Volume Percent Martensite
M1	MIQ	IQ	750	~ 25
M1	MIA	IA	750	~ 25
M1	MSQ	SQ	650	~ 27
M1	MM	-	-	~ 100
M2	MHR	HR	740†	~ 20

IQ : Intermediate Quenching Process

IA : Intercritical Annealing Process

SQ : Step Quenching Process

HR : Controlled Rolling Process

† : Finish Rolling Temperature

Table 4. Summary of Tensile Properties

(As Heat Treated)

A. Fe-Si-C Alloy

Specimen	Yield. Strength ksi(MPa)	Tensile Strength ksi(MPa)	Uniform Elongation (%)	Total Elongation (%)	Reduction of Area (%)
SHR	80(552)	120(827)	15.3	26.5	65
SIQ1	71(490)	117(807)	12.4	22.7	55
SIQ2	83(572)	130(896)	10.0	20.0	53
SIQ3	91(627)	136(938)	8.7	18.6	53
SIA1	72(496)	121(834)	10.2	20.0	56
SIA2	83(572)	128(883)	10.0	19.0	-
SSQ1	83(572)	124(855)	9.6	15.3	36
SSQ2	98(676)	137(945)	7.0	12.0	28
SM	147(1014)	173(1193)	3.5	12.3	53

Table 4. Summary of Tensile Properties

(As Heat Treated)

B. Fe-Mn-C Alloy

Specimen	Yield Strength ksi(MPa)	Tensile Strength ksi(MPa)	Uniform Elongation (%)	Total Elongation (%)	Reduction of Area (%)
MIQ	59(407)	100(690)	13.0	20.0	40
MIA	60(414)	102(703)	11.0	18.5	41
MSQ	53(365)	91 (627)	11.5	17.0	32
MM	149(1027)	166(1145)	2.2	13.4	59
MHR	54(372)	97 (669)	18.0	30.0	71

Table 5. Drawability

Specimen	Minimum Diameter (inch)	Total Drawing Strain
SIQ1	<0.0105	>6.06
SHR	<0.0105	>6.06
MHR	<0.0105	>6.06
SIQ2	0.0136	5.54
SIA1	0.0172	5.07
SIA2	0.0221	4.57
SIQ3	0.0284	4.07
MIQ	0.0284	4.07
SSQ1	0.0526	2.83
SSQ2	0.0526	2.83
MIA	0.0526	2.83
SQM	0.0764	2.09

Table 6. Tensile Properties of Drawn Wires at a Drawing Strain of 0.44

Specimen	Yield Strength ksi(MPa)	Tensile Strength ksi(MPa)	Uniform Elongation (%)	Total Elongation (%)	Reduction of Area (%)
SHR	166(1145)	168(1158)	0.6	9.8	48
SIQ1	169(1165)	170(1172)	0.6	9.2	45
SIQ2	177(1220)	179(1234)	0.5	9.1	44
SIQ3	187(1289)	188(1296)	0.4	9.1	43
MIQ	151(1041)	155(1069)	0.7	6.6	23

Table 7. Tensile Strength of Dual-Phase Steel Wires

A. Controlled Rolling Process

Wire Dia. (inch)	Total Drawing Strain	Tensile Strength, ksi(MPa) SHR	MHR
0.217	0	120 (827)	97 (669)
0.174	0.44	168(1158)	-
0.119	1.20	205(1413)	176(1213)
0.0764	2.09	223(1538)	195(1345)
0.0526	2.83	245(1689)	-
0.0362	3.58	280(1930)	252(1738)
0.0195	4.82	340(2344)	307(2117)
0.0136	5.54	380(2620)	357(2462)
0.0105	6.06	407(2806)	380(2620)

Table 7. Tensile Strength of Dual-Phase Steel Wires

B. Intermediate Quenching Process

Wire Dia. (inch)	Total Drawing Strain	Tensile Strength, ksi(MPa) SIQ1	SIQ2	SIQ3
0.217	0	117 (807)	130 (896)	136 (938)
0.174	0.44	170(1172)	179(1234)	188(1296)
0.119	1.20	201(1386)	215(1482)	220(1517)
0.0764	2.09	217(1496)	233(1607)	245(1689)
0.0526	2.83	245(1689)	260(1793)	276(1903)
0.0362	3.58	271(1869)	287(1979)	300(2069)
0.0172	5.07	345(2379)	369(2544)	-
0.0136	5.54	375(2586)	395(2724)	-
0.0105	6.06	403(2779)	-	-

Table 7. Tensile Strength of Dual-Phase Steel Wires

C. Intercritical Annealing Process

Wire Dia. (inch)	Total Drawing Strain	Tensile Strength, ksi(MPa) SIA1	SIA2
0.0217	0	121 (834)	128 (883)
0.0119	1.20	207(1427)	220(1517)
0.0764	2.09	222(1530)	232(1600)
0.0526	2.83	255(1758)	270(1862)
0.0362	3.58	282(1944)	290(2000)
0.0221	4.57	-	339(2337)
0.0172	5.07	350(2413)	-

Table 7. Tensile Strength of Dual-Phase Steel Wires

D. Step Quenching Process

Wire Dia. (inch)	Total Drawing Strain	Tensile Strength, ksi(MPa) SSQ1	SSQ2
0.217	0	124 (855)	137 (945)
0.119	1.20	195(1345)	207(1427)
0.0764	2.09	215(1482)	230(1586)
0.0526	2.83	230(1586)	250(1724)

Table 8. Microhardness Data

A. Specimen SQS1 ($\sim$ 30% Martensite)

Wire Dia. (inch)	Total Drawing Strain	Ferrite	Martensite
0.217	0	230 ± 10	505 ± 10
0.142	0.85	330 ± 10	530 ± 10
0.119	1.20	350 ± 10	560 ± 10
0.0764	2.09	370 ± 10	600 ± 10
0.0526	2.83	385 ± 10	620 ± 15

Table 8. Microhardness Data

B. Specimen SQS2 ($\sim$ 50% Martensite)

Wire Dia. (inch)	Total Drawing Strain	Ferrite	Martensite
0.217	0	215 $\pm$ 10	420 $\pm$ 10
0.142	0.85	310 $\pm$ 15	460 $\pm$ 15
0.119	1.20	340 $\pm$ 10	490 $\pm$ 10
0.0764	2.09	375 $\pm$ 10	525 $\pm$ 10
0.0526	2.83	400 $\pm$ 10	540 $\pm$ 15

Table 9. Drawing Schedule

Pass No.	Wire Dia. (inch)	Reduction of Area per Pass (%)	Total Reduction of Area (%)	Total Drawing Strain
0	0.217	-	-	0
1	0.174	35.7	35.7	0.44
2	0.142	33.4	57.2	0.85
3	0.119	29.8	69.9	1.20
4	0.1019	26.7	77.9	1.51
5	0.0864	28.1	84.1	1.84
6	0.0764	21.8	87.6	2.09
7	0.0674	22.2	90.4	2.34
8	0.0596	21.8	92.5	2.58
9	0.0526	22.1	94.1	2.83
10	0.0465	21.8	95.4	3.08
11	0.0410	22.3	96.4	3.33
12	0.0362	22.0	97.2	3.58
13	0.0320	21.9	97.8	3.83
14	0.0284	21.2	98.3	4.07
15	0.0250	22.5	98.7	4.32
16	0.0221	21.9	99.0	4.57
17	0.0195	22.1	99.2	4.82
18	0.0172	22.2	99.4	5.07
19	0.0153	20.9	99.5	5.30
20	0.0136	21.0	99.6	5.54
21	0.0119	23.4	99.7	5.81
22	0.0105	22.1	99.77	6.06

FIGURE CAPTIONS

Fig. 1. Manufacturing process of steel tire cord.

Fig. 2. Stress-strain curves for a Fe/Mn/Si/V/0.1C steel with dual-phase microstructures of two different martensite volume fractions; and with a ferrite-pearlite microstructure (29).

Fig. 3. Schematic of the intermediate quenching process.

Fig. 4. Schematic of three stages of the controlled rolling process and change in microstructure with deformation in each stage.

Fig. 5. Schematic of the intercritical annealing process.

Fig. 6. Schematic of the step quenching process.

Fig. 7. Phase diagrams showing the expansion of the ($\alpha+\gamma$) range when silicon is added to the Fe-C system.

Fig. 8. Schematic of the wire drawing process.

Fig. 9. Schematic of the velocity fields in the wire under central burst conditions.

Fig. 10. Schematic of a dilatometry specimen for measuring phase transformation temperatures.

Fig. 11. Schematic of a subsize cylindrical tensile test specimen.

Fig. 12. Optical micrographs of the initial martensite structure before two phase annealing in the intermediate quenching process. (a) Specimen SM and (b) Specimen MIM.

Fig. 13. Transmission electron micrographs revealing the interlath retained austenite in the specimen SM.

(a) Bright field image.

(b) Corresponding dark field image where thin films of retained austenite reversed contrast when the (002) spot was used for imaging.

(c) Selected area diffraction pattern.

(d) Indexing of the diffraction pattern in (c), showing K-S relationship of martensite and austenite.

Fig. 14. Scanning electron micrographs of the dual-phase microstructures produced by the intermediate quenching process. (a) Specimen SIQ1 and (b) Specimen MIQ.

Fig. 15. Transmission electron micrograph of the dual-phase microstructure. M: martensite F: ferrite

Fig. 16. Transmission electron micrograph of the dual-phase microstructure of specimen SIQ1.

Fig. 17. Scanning electron micrograph of the dual-phase microstructure produced by the intercritical annealing process. Specimen SIA1.

Fig. 18. Scanning electron micrographs of the dual-phase microstructure produced by the step quenching process. (a) Specimen SSQ1 and (b) Specimen MSQ.

Fig. 19. Scanning electron micrograph of the dual-phase microstructure obtained by the controlled rolling process. Specimen SHR.

Fig. 20. High magnification scanning electron micrograph of the dual-phase microstructure of specimen SHR.

Fig. 21. Transmission electron micrograph showing the ferrite matrix of the dual-phase microstructure obtained by the controlled rolling process. Specimen SHR.

Fig. 22. Scanning electron micrographs of the drawn dual-phase microstructure on a longitudinal section as a function of the reduction in area (R.A.) by cold drawing.
Specimen SIA1 (A) 0% R.A. (ε = 0); (B) 70% R.A. (ε = 1.2); (C) 88% R.A. (ε = 2.1); (D) 97% R.A. (ε = 3.6).

Fig. 23. Scanning electron micrographs of the drawn dual-phase microstructure on a longitudinal section at ε = 3.6, i.e., after 97% R.A.
(A) Specimen SIQ1; (B) Specimen SIA1; (C) Specimen SHR.

Fig. 24. Scanning electron micrograph of the drawn dual-phase microstructure of specimen SSQ1 on a longitudinal section at ε = 2.8.

Fig. 25. Vickers hardness of ferrite and martensite as a function of drawing strain. Specimen SSQ1.

Fig. 26. Vickers hardness of ferrite and martensite as a function of drawing strain. Specimen SSQ2.

Fig. 27. Transmission electron micrograph of the drawn dual-phase microstructure on a longitudinal section at ε = 2.8. Specimen SIQ1.

Fig. 28. Transmission electron micrographs showing highly deformed ferrite (a) and martensite (b) on a longitudinal section at $\epsilon = 2.8$. Specimen SIQ1.

Fig. 29. Transmission electron micrographs showing highly deformed ferrite (a) and martensite (b) on a longitudinal section at $\epsilon = 3.6$. Specimen SIQ1.

Fig. 30. Transmission electron micrograph of the drawn dual-phase microstructure showing [110] wire texture on a longitudinal section at $\epsilon = 3.6$.

Fig. 31. Scanning electron micrographs showing the drawn dual-phase microstructure on a transverse section at $\epsilon = 2.8$. (a) Specimen SIQ1 and (b) Specimen SIA1.

Fig. 32. Transmission electron micrograph of the drawn dual-phase microstructure on a transverse section at $\epsilon = 2.8$. Specimen SIA1.

Fig. 33. Yield and ultimate tensile strengths as a function of martensite volume fraction for the silicon containing dual-phase steels.

Fig. 34. Uniform and total elongations as a function of martensite volume fraction for the silicon containing dual-phase steels.

Fig. 35. Yield and ultimate tensile strengths of the manganese containing dual-phase steels given different heat treatments.

Fig. 36. Uniform and total elongations, and reduction in area of the manganese containing dual-phase steels given different heat treatments.

Fig. 37. Scanning electron fractographs of broken tensile specimens. (A) Specimen SIQ1 and (B) Specimen SSQ1.

Fig. 38. Tensile strength of dual-phase steel wire as a function of wire diameter. Specimen SHR.

Fig. 39. Tensile strength of dual-phase steel wire as a function of wire diameter. Specimen MHR.

Fig. 40. Tensile strength of dual-phase steel wire as a function of wire diameter. Specimens SIQ1 and SIQ2.

Fig. 41. Comparison of the drawing schedule and resulting tensile strength for dual-phase steel wire and patented pearlitic steel wire.

Fig. 42. Transmission electron micrograph showing the presence of twinned martensite in the initial dual-phase microstructure.

Fig. 43. Scanning electron micrograph of highly deformed ferrite around non-deforming twinned martensite particles on a longitudinal section at $\varepsilon = 3.6$. Notice the void formation near the martensite-ferrite interface.

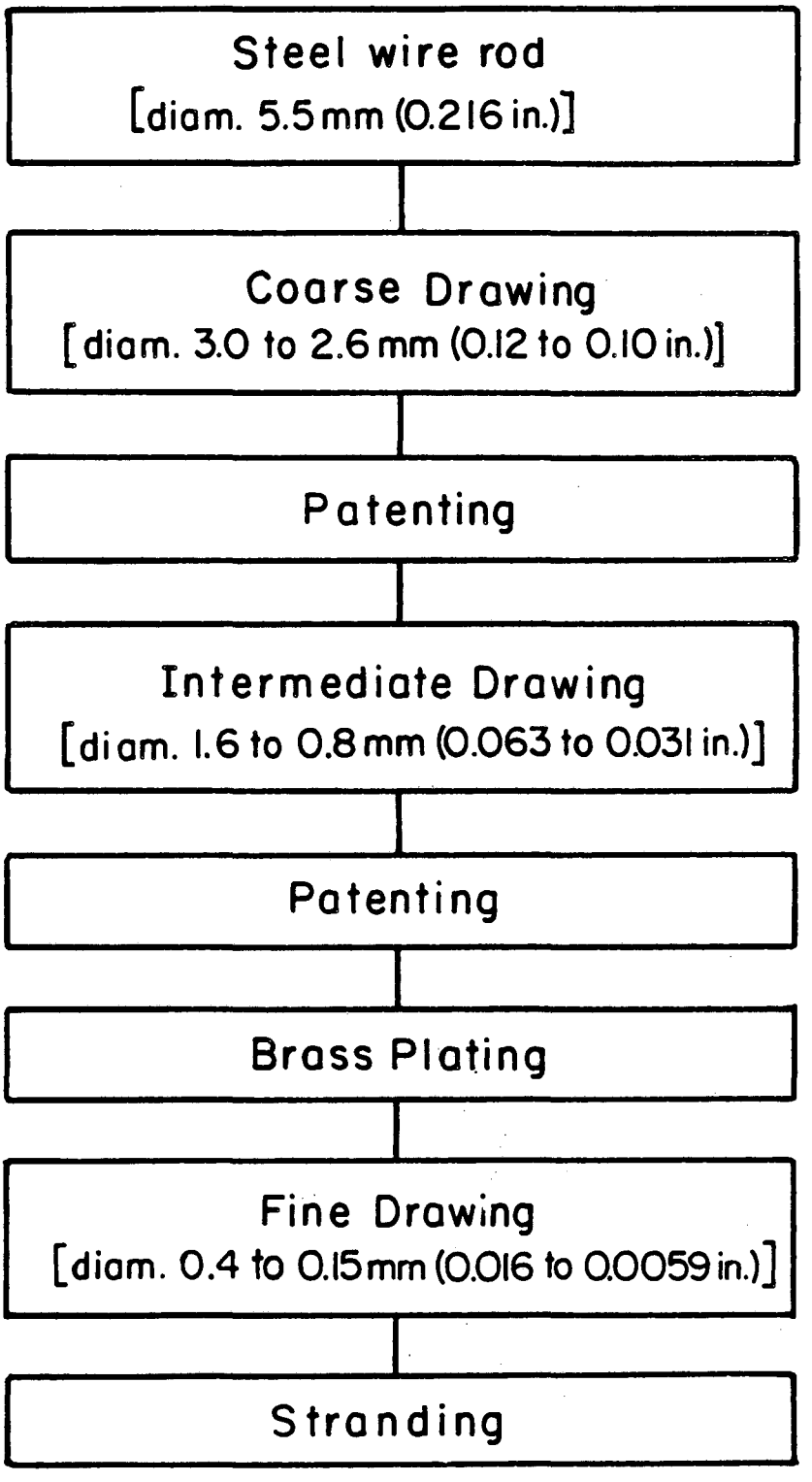

XBL 847-7217

Fig. 1

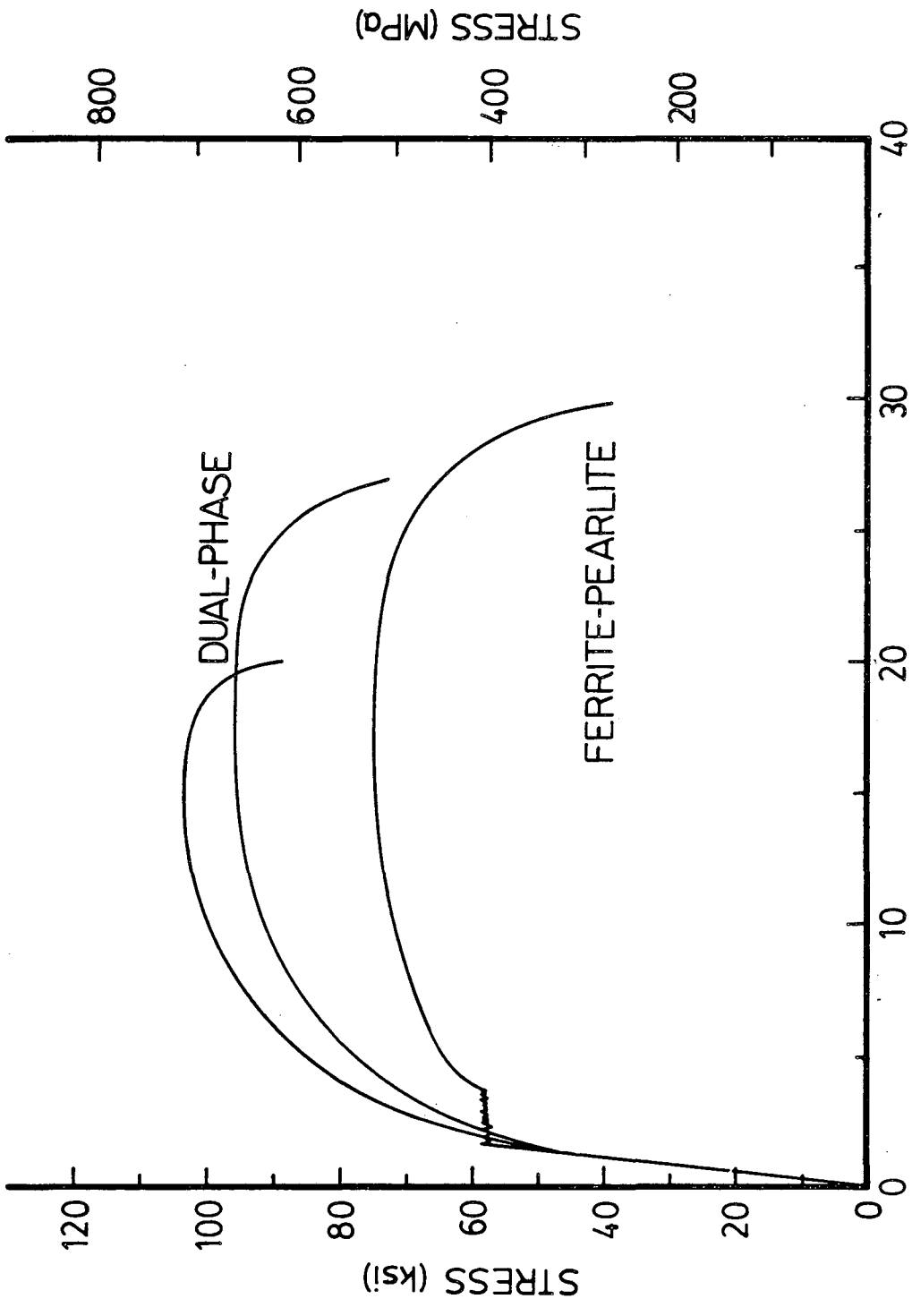

XBL 838-11019

Fig. 2

Intermediate Quenching Treatment

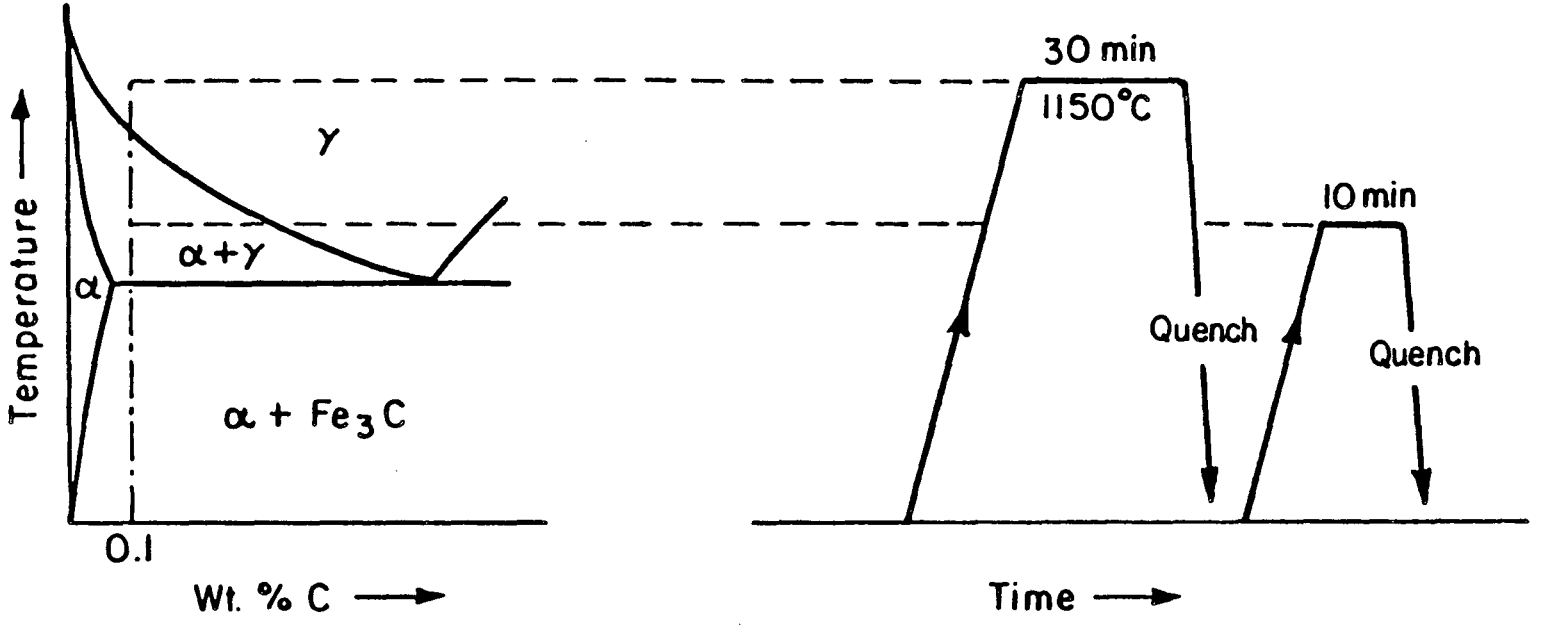

XBL 837-5986A

Fig. 3

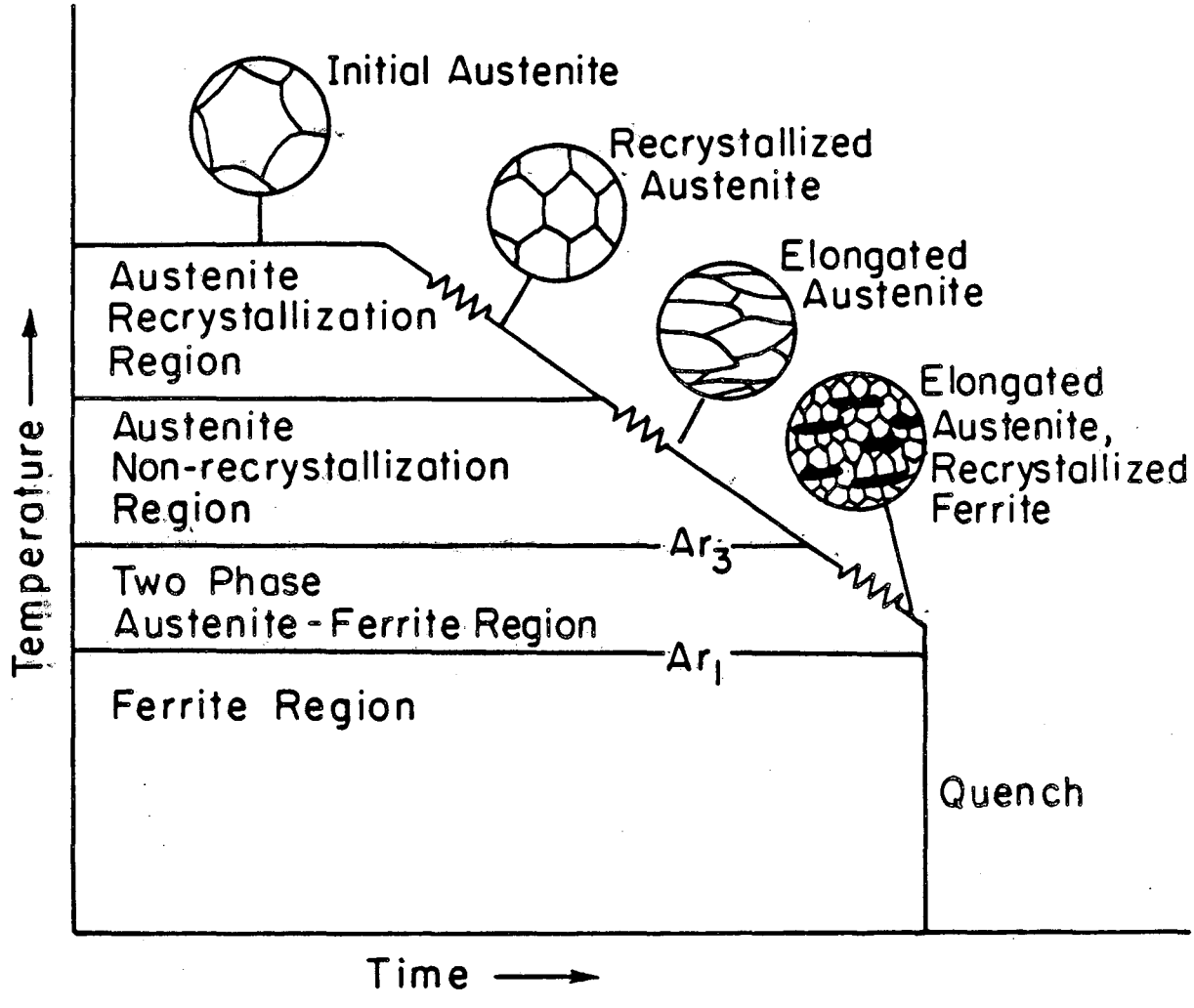
Initial Austenite
Recrystallized Austenite
Elongated Austenite
Elongated Austenite, Recrystallized Ferrite
Austenite Recrystallization Region
Austenite Non-recrystallization Region
Ar_3
Two Phase Austenite-Ferrite Region
Ar_1
Ferrite Region
Quench
Temperature
Time
XBL852-5872

Fig. 4

Intercritical Annealing Treatment

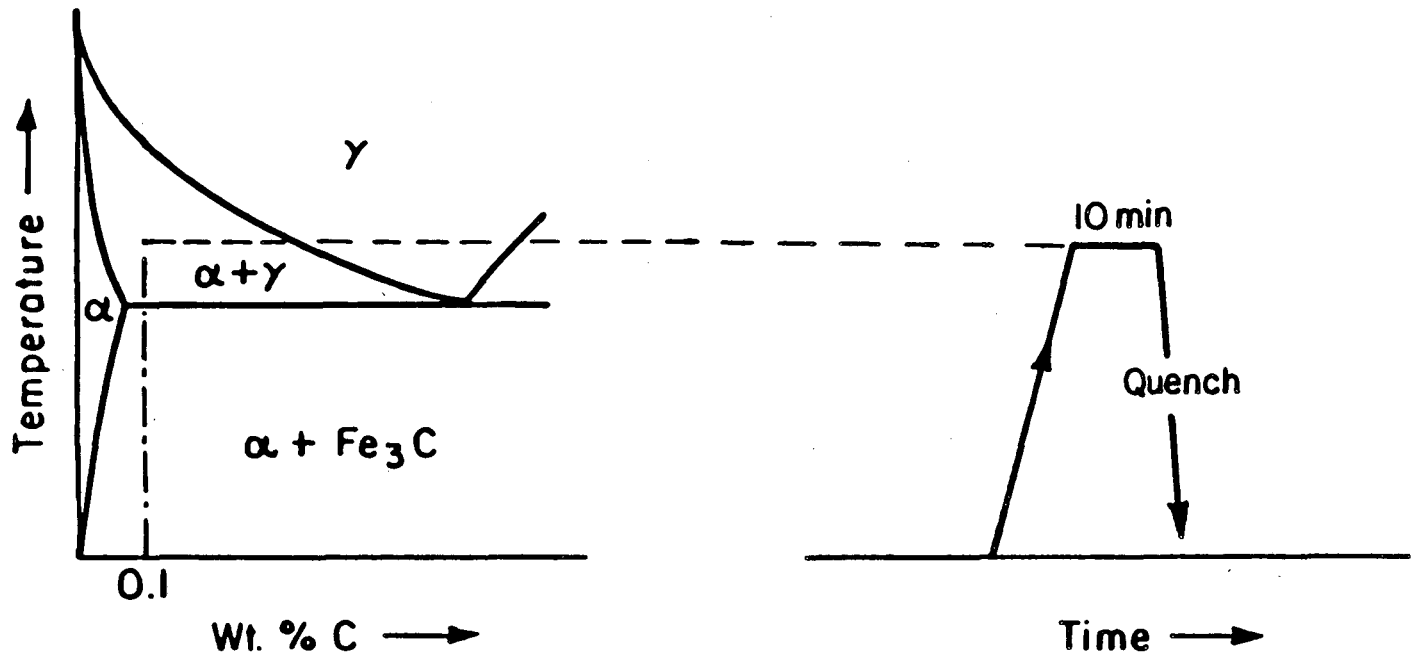

XBL 837-5986C

Fig. 5

Step Quenching Treatment

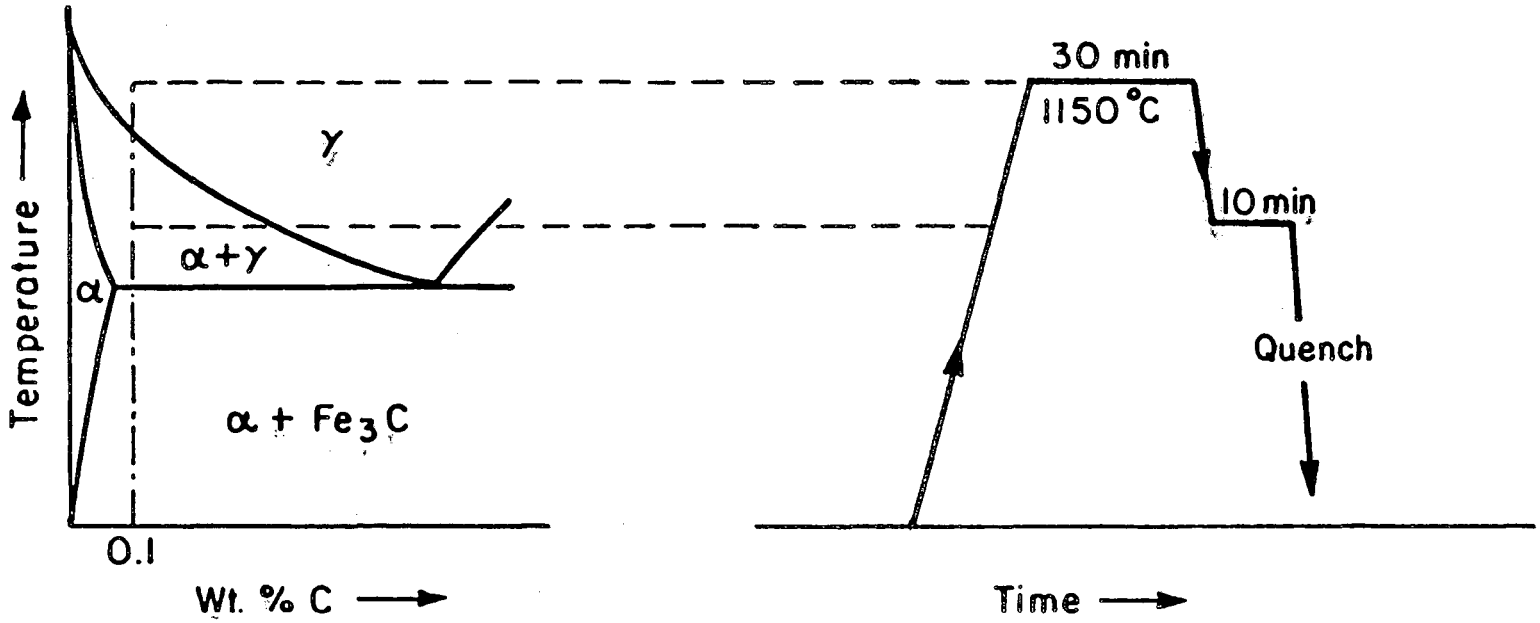

Fig. 6

Fe-RICH PORTION OF THE Fe-C PHASE DIAGRAM

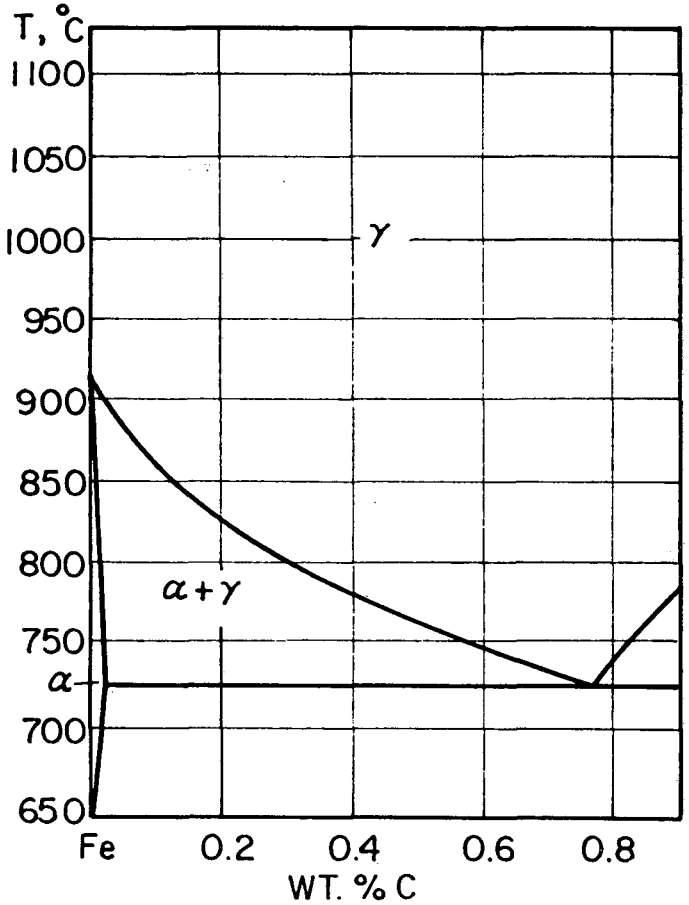

Fe-RICH PORTION OF THE 2.4 WT. % Si SECTION OF THE Fe-Si-C PHASE DIAGRAM

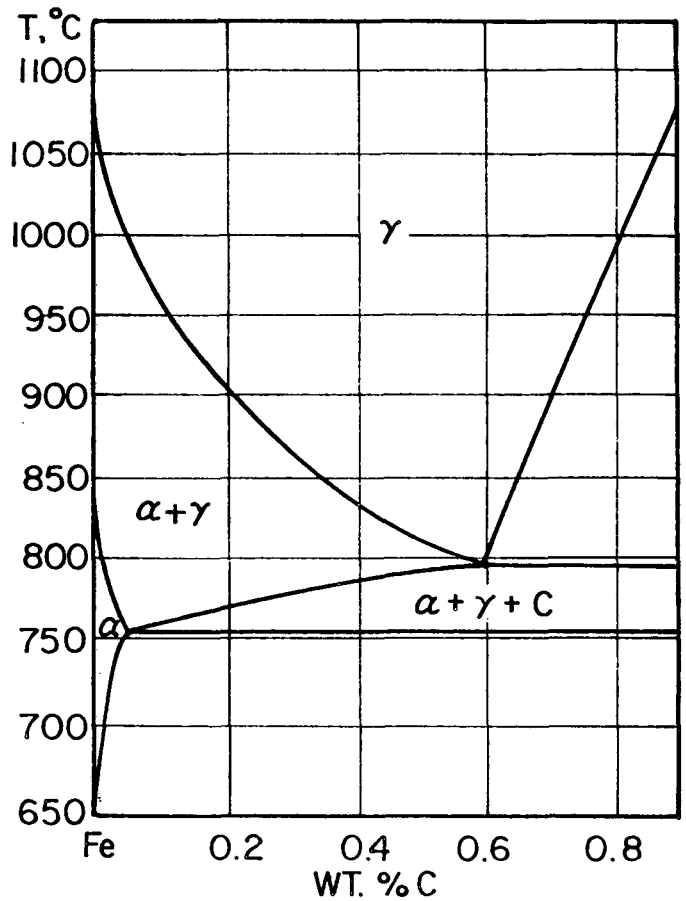

Fig. 7

XBL 761-6344

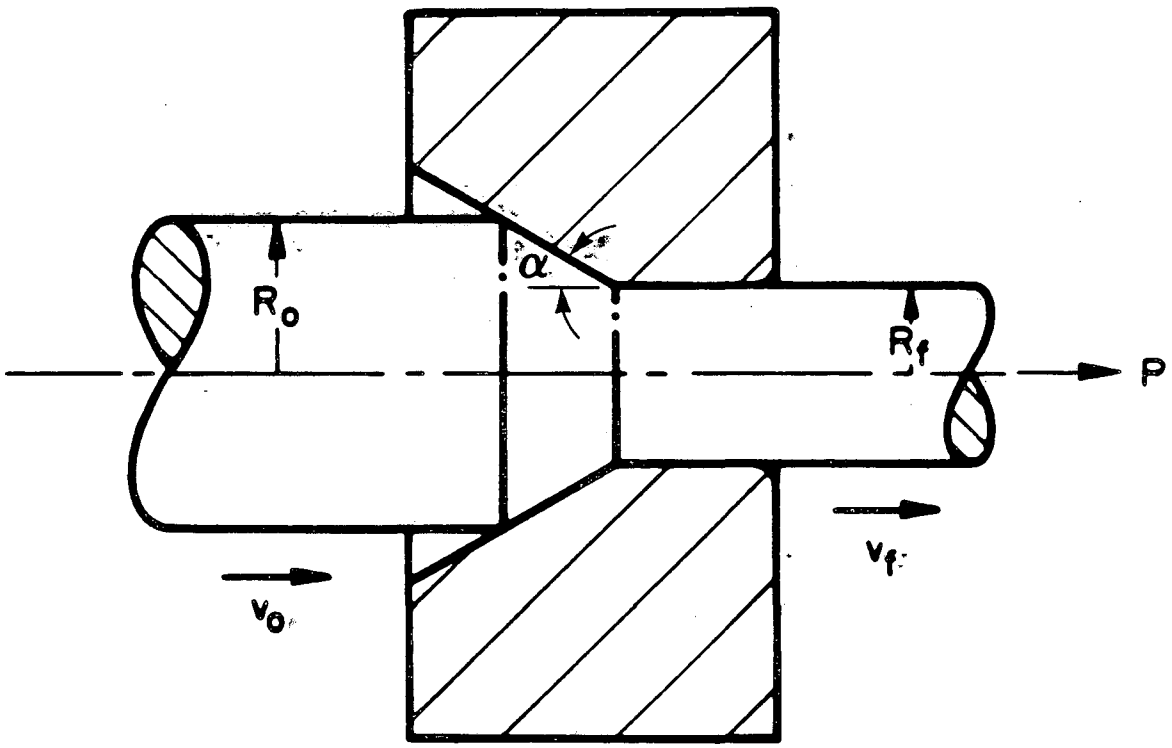

XBL 8610-8998

Fig. 8

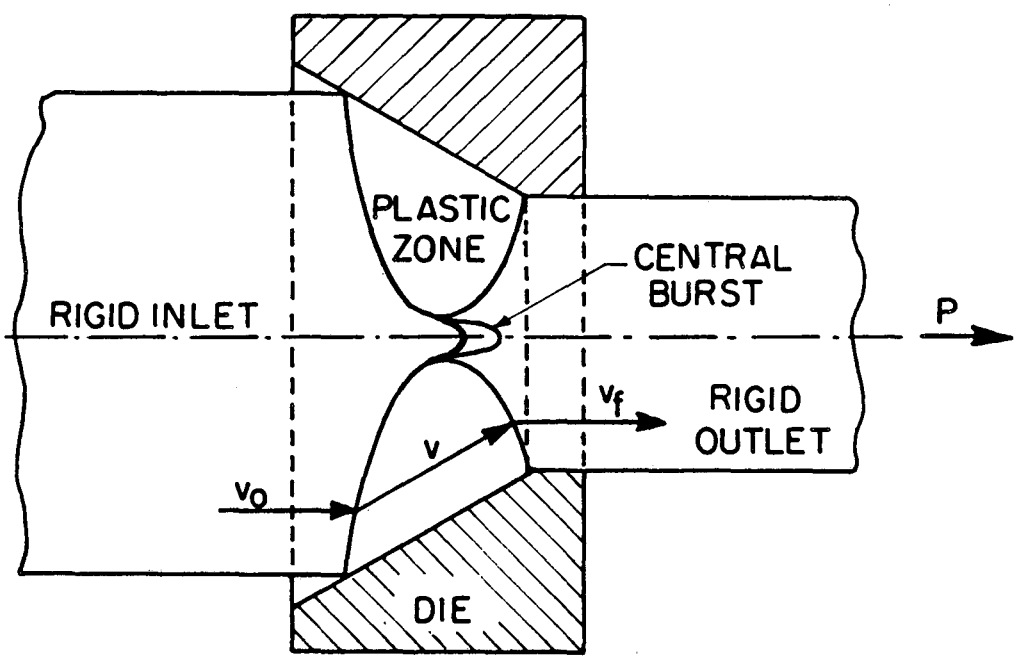

XBL832-5226

Fig. 9

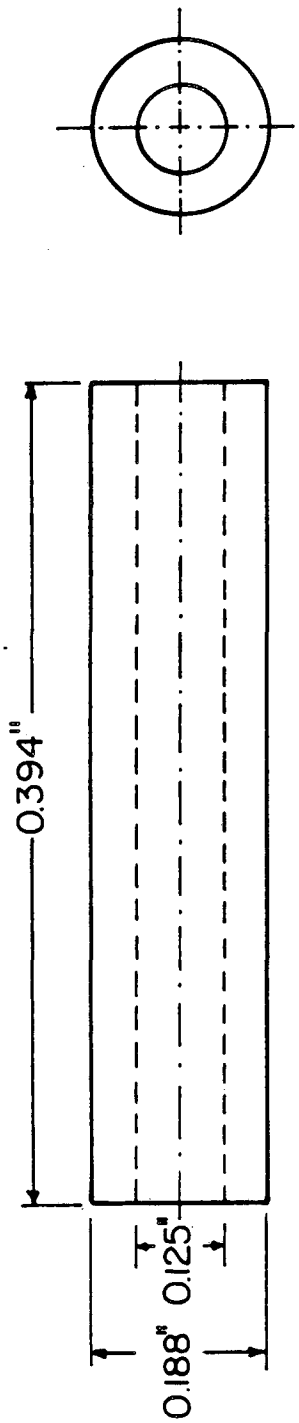

XBL 7910-7192

Fig. 10

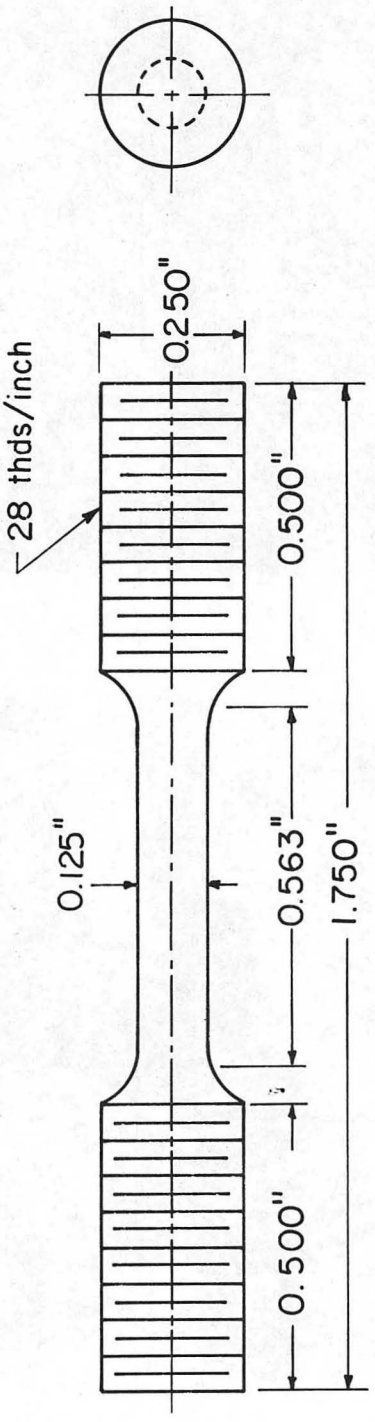

XBL 774-5354

Fig. 11

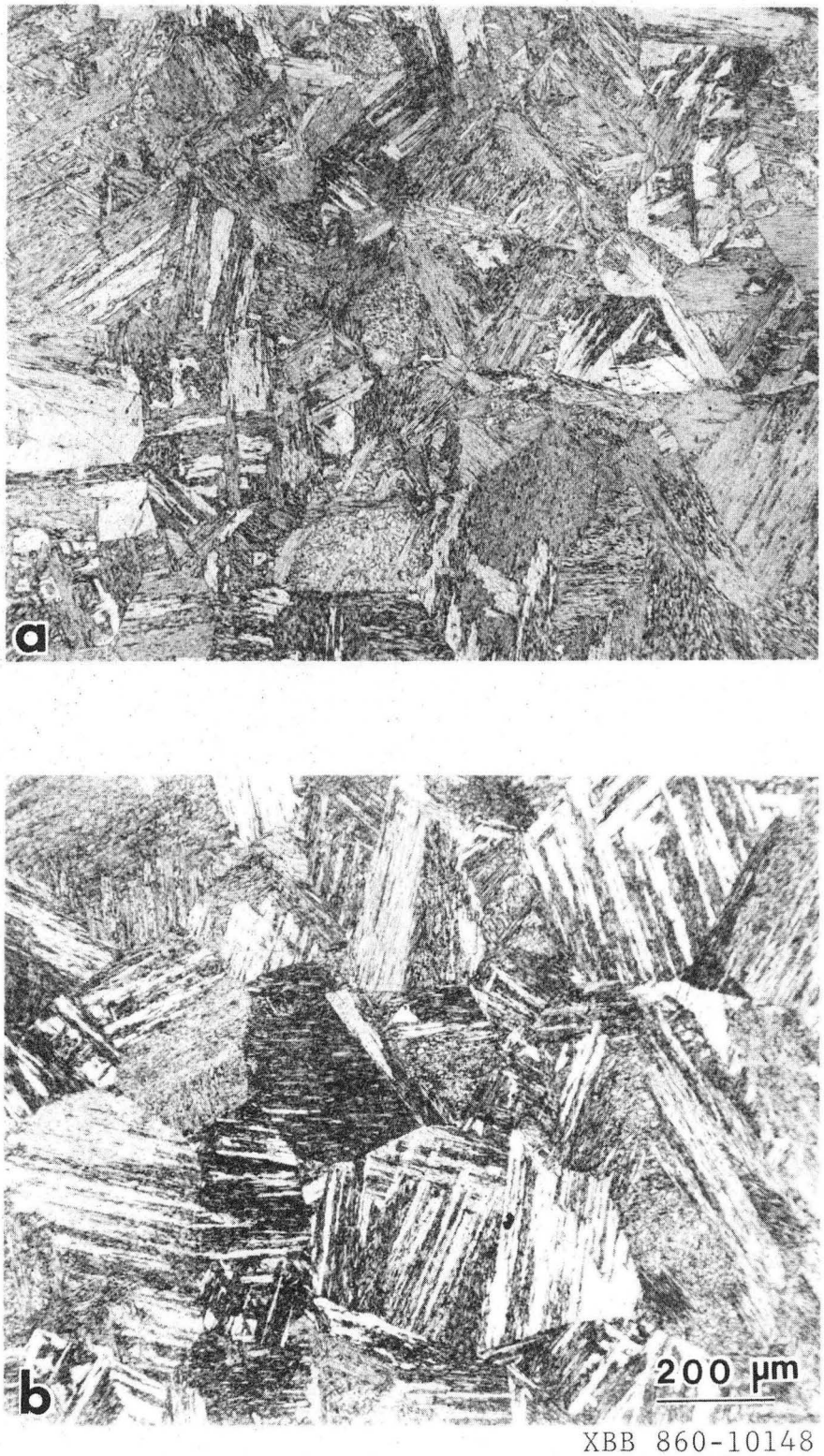

XBB 860-10148

Fig. 12

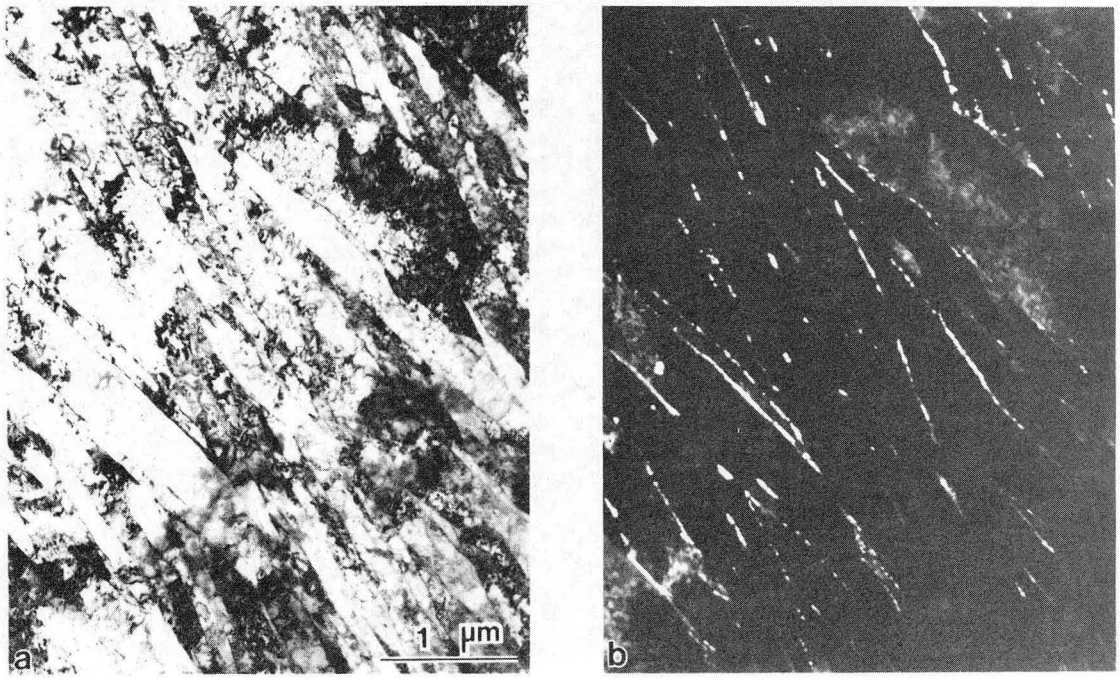

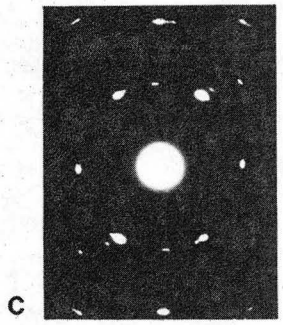

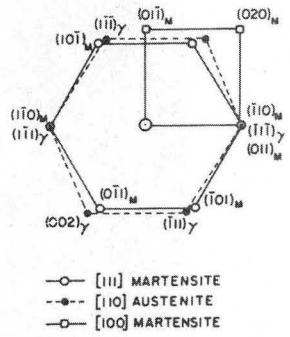

d

XBB 860-10315

Fig. 13

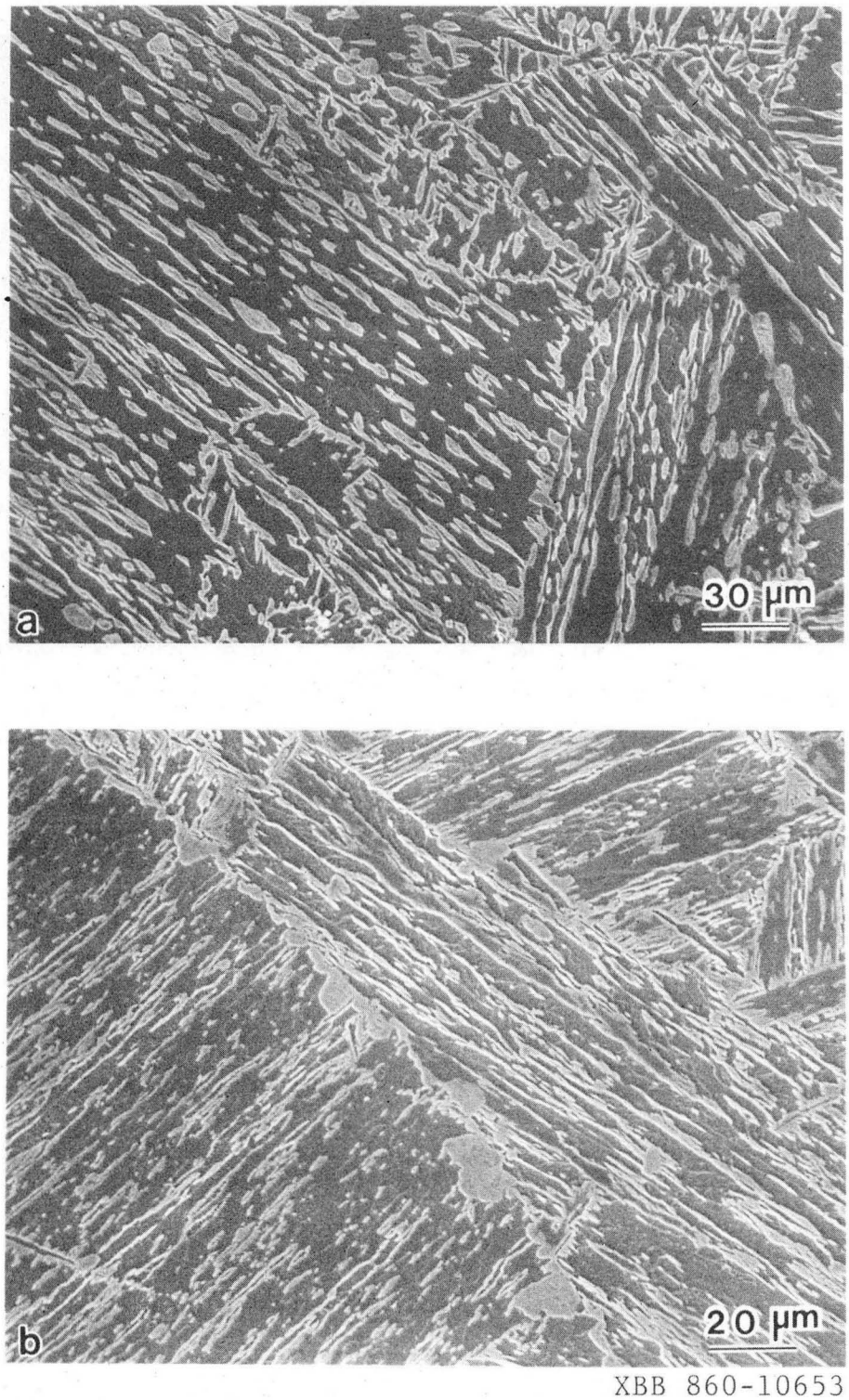

XBB 860-10653

Fig. 14

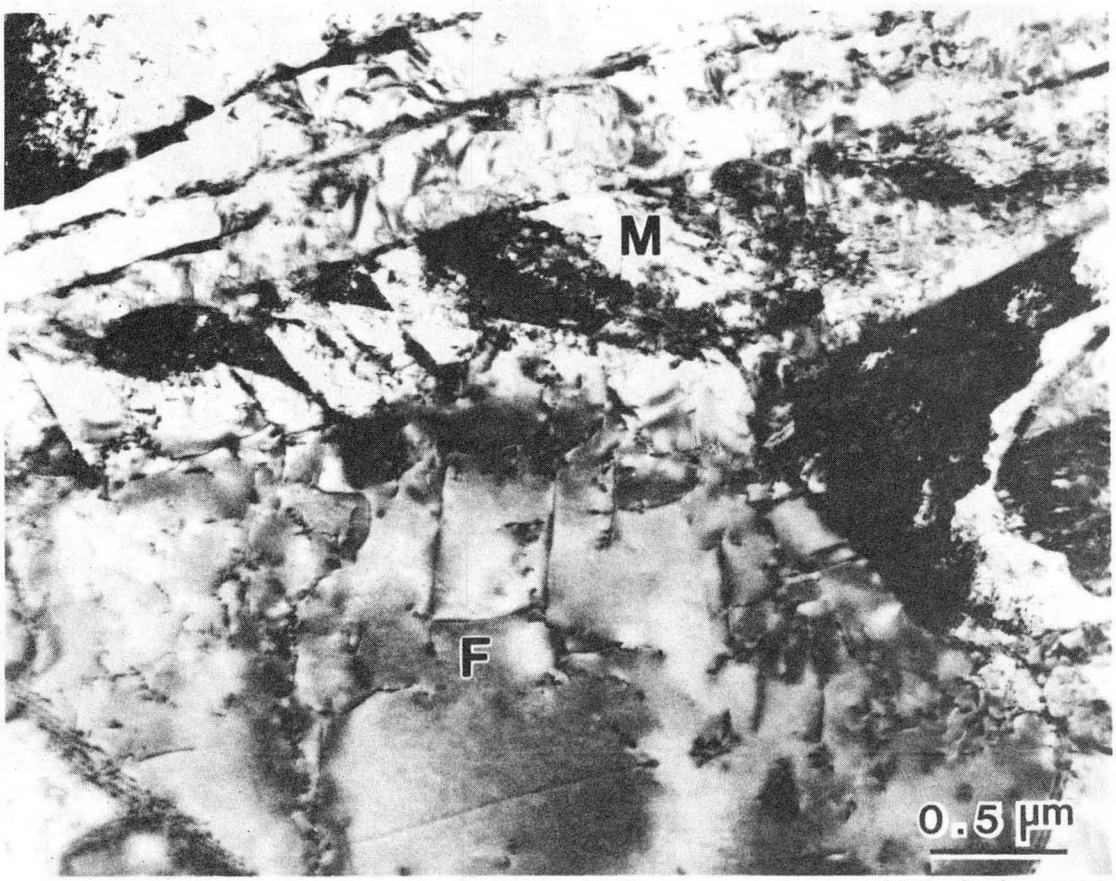

XBB 858-5976

Fig. 15

XBB 850-8429

Fig. 16

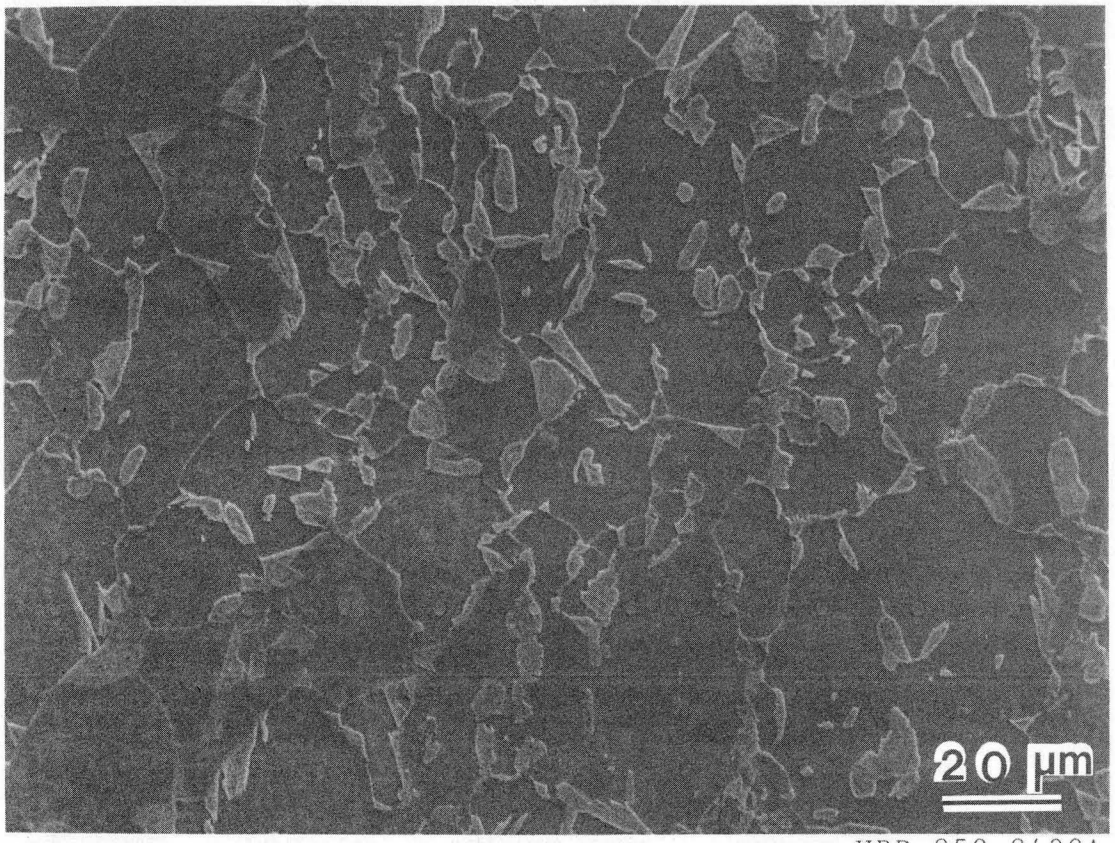

XBB 850-8430A

Fig. 17

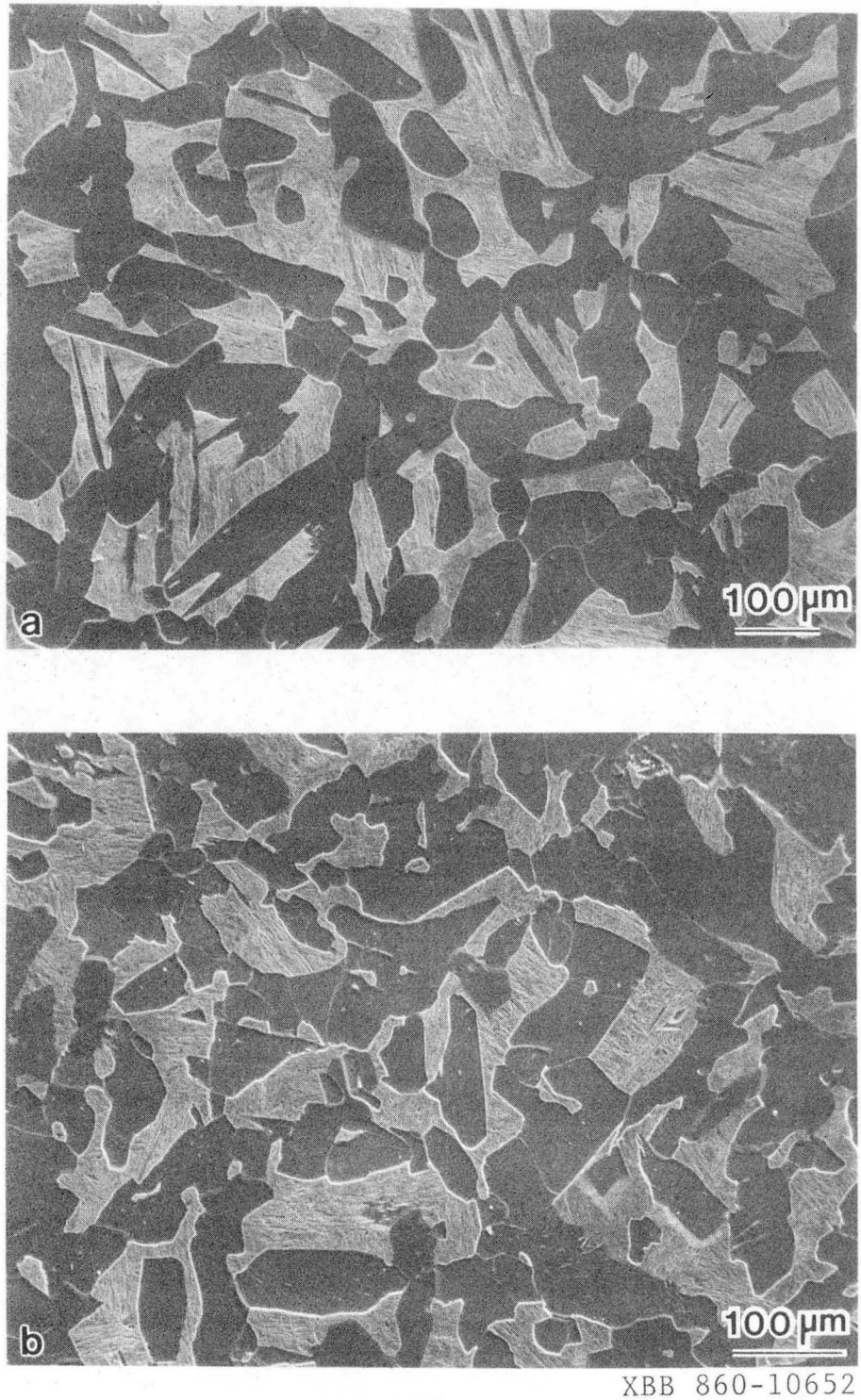

XBB 860-10652

Fig. 18

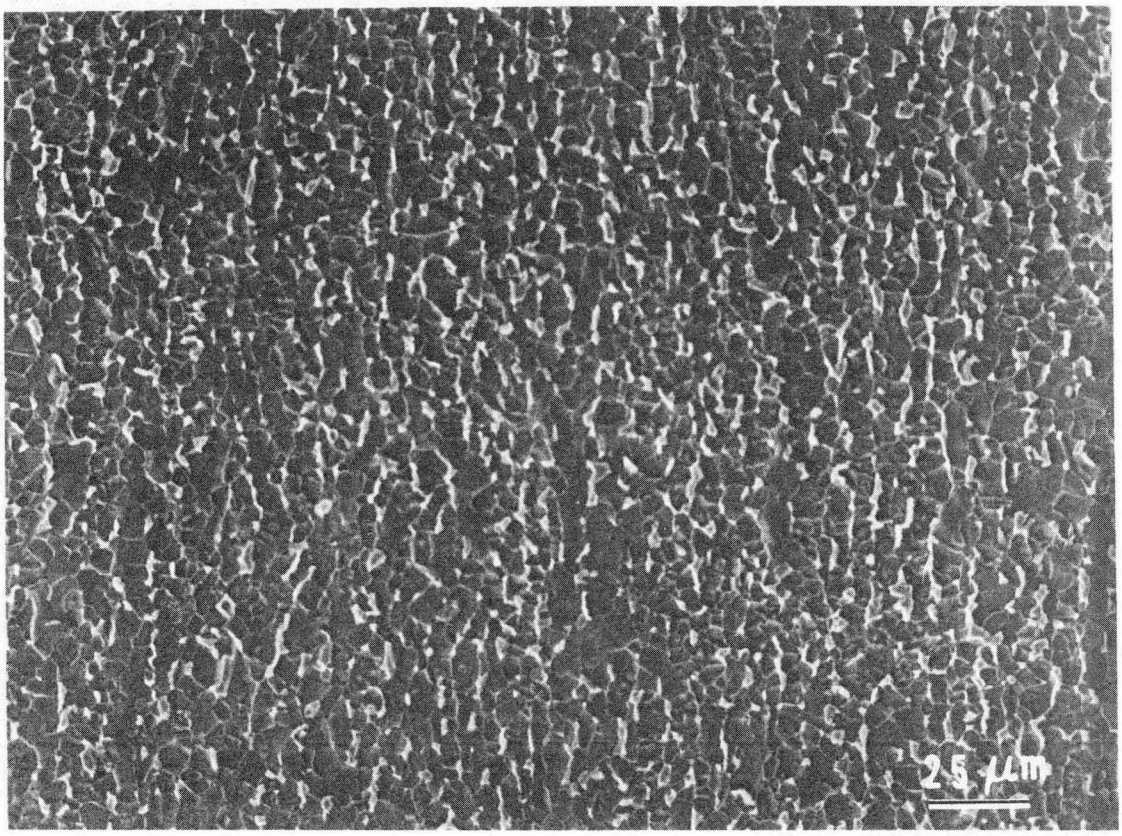

XBB 852-1508A

Fig. 19

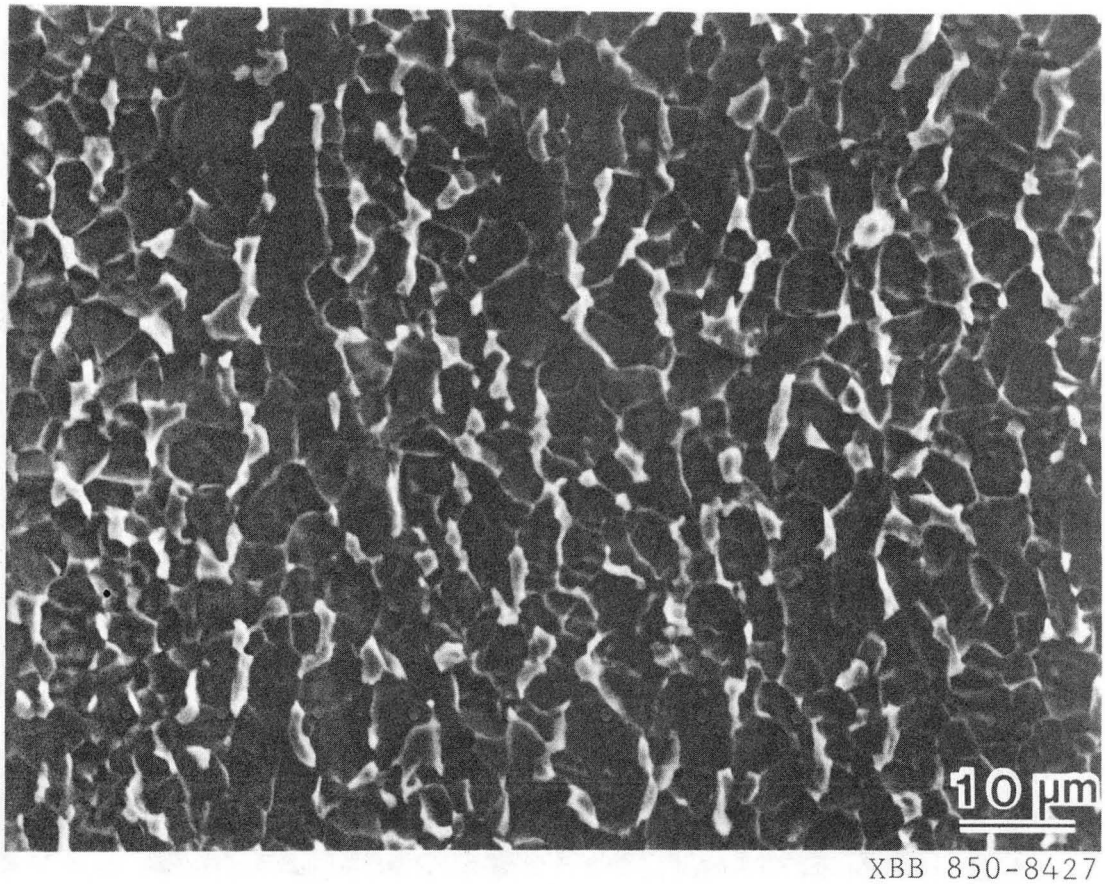

XBB 850-8427

Fig. 20

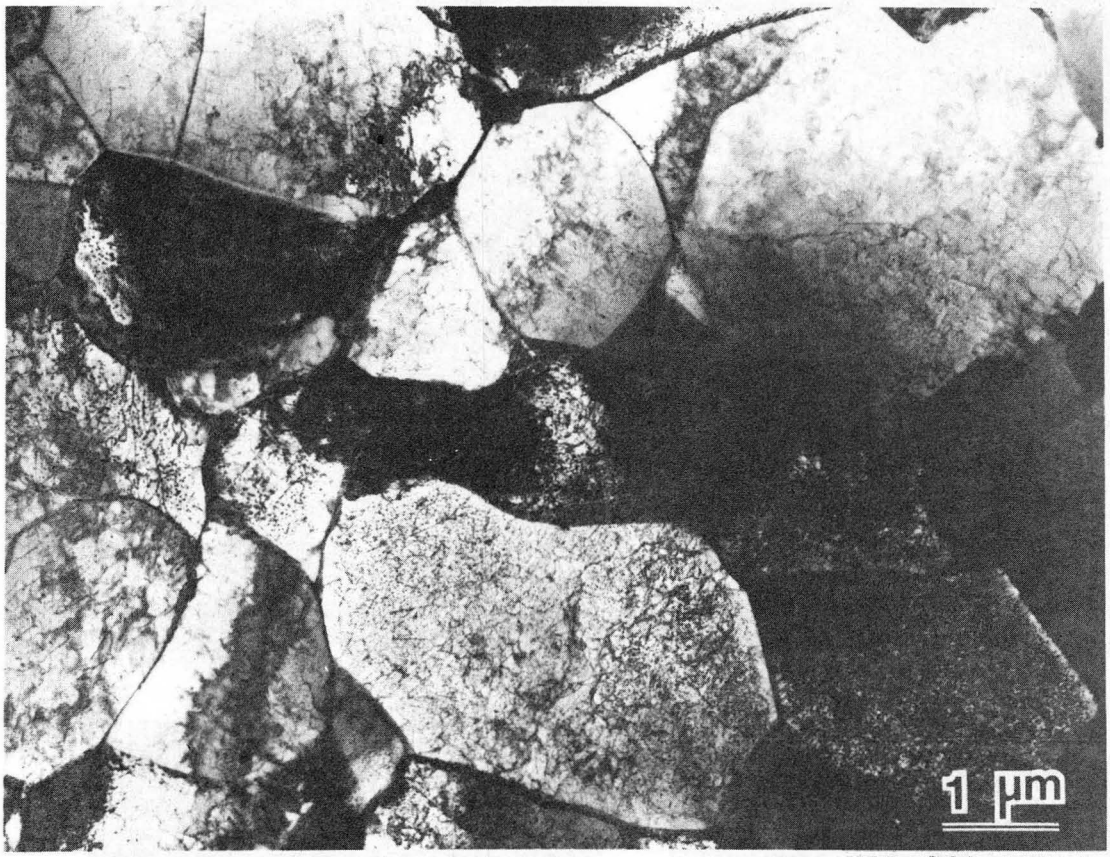

XBB 860-10145

Fig. 21

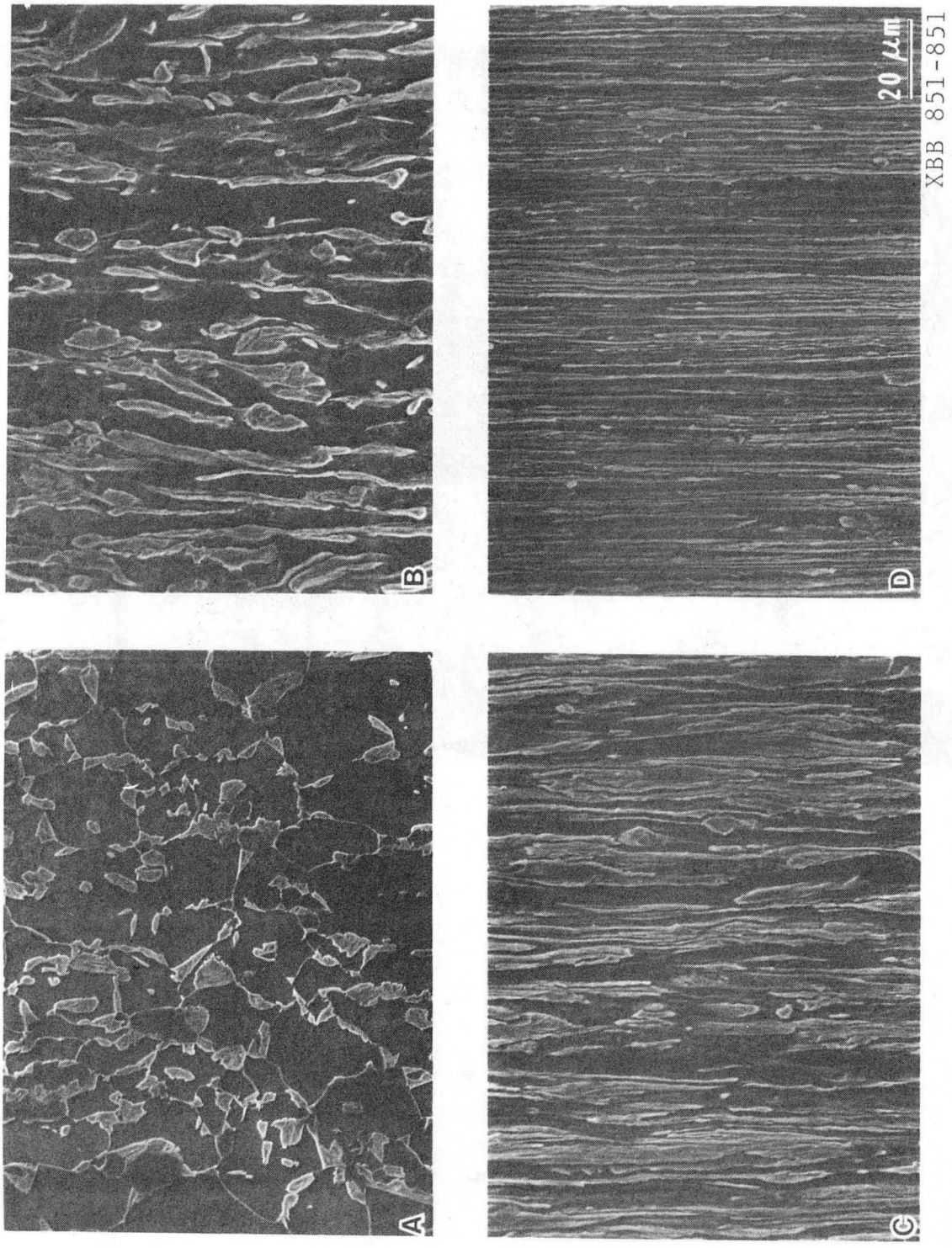

XBB 851-851

Fig. 22

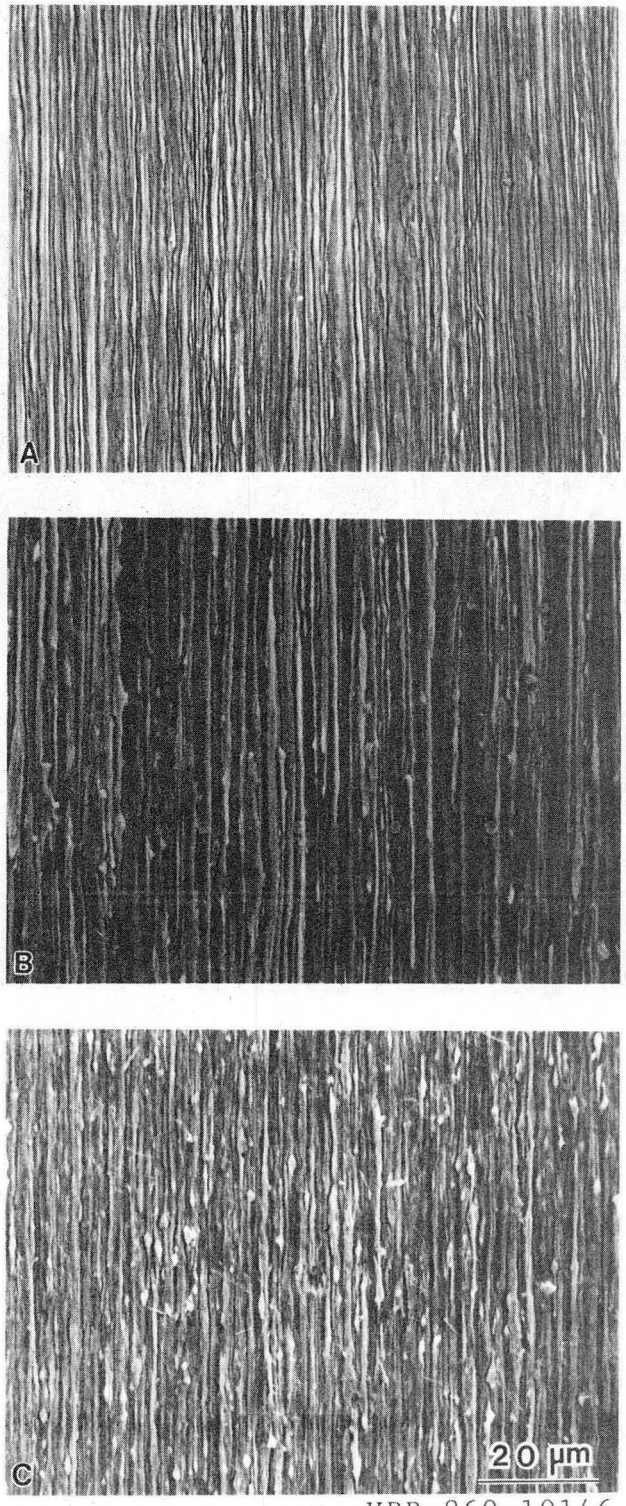

XBB 860-10146

Fig. 23

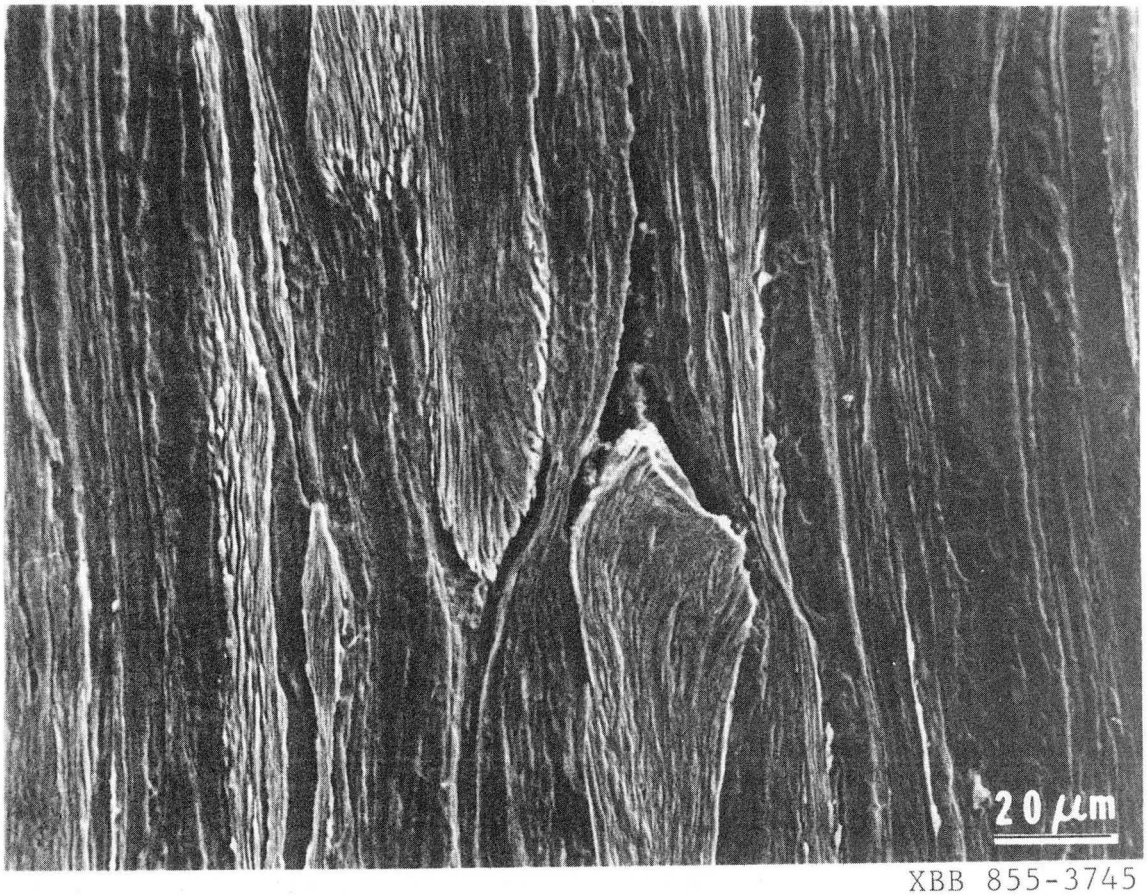

XBB 855-3745

Fig. 24

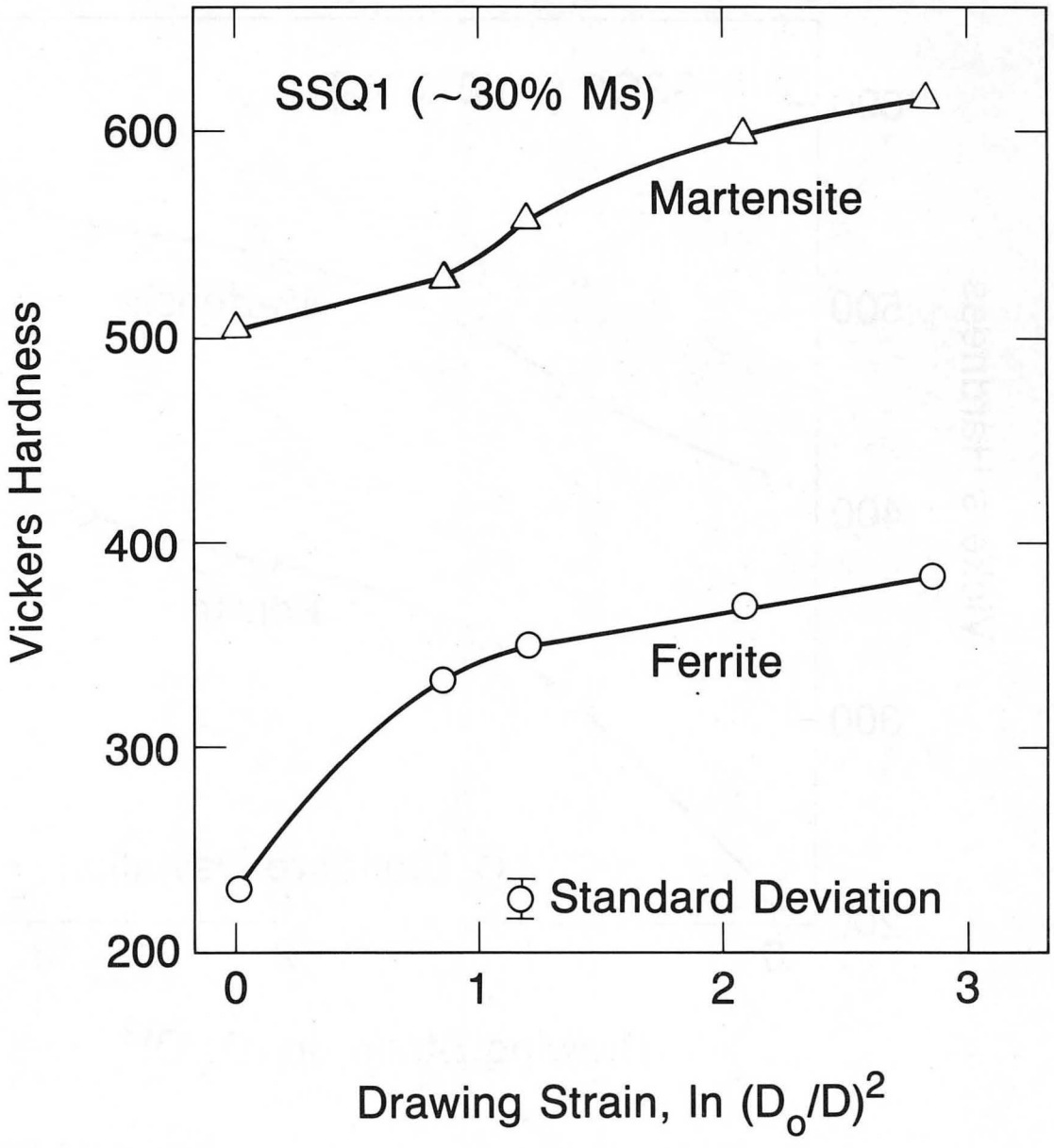

XBL 8611-6464

Fig. 25

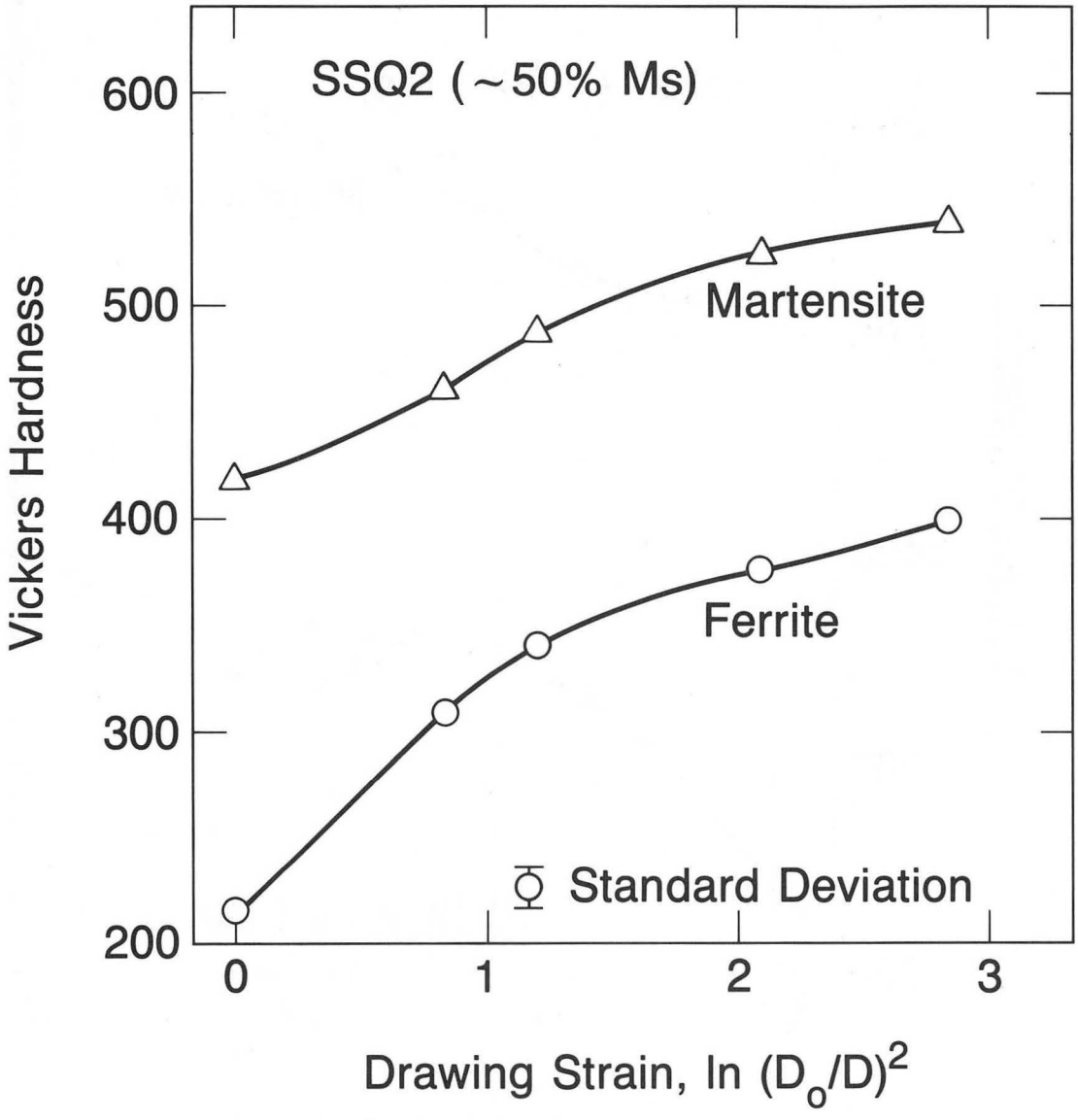

XBL 8611-6465

Fig. 26

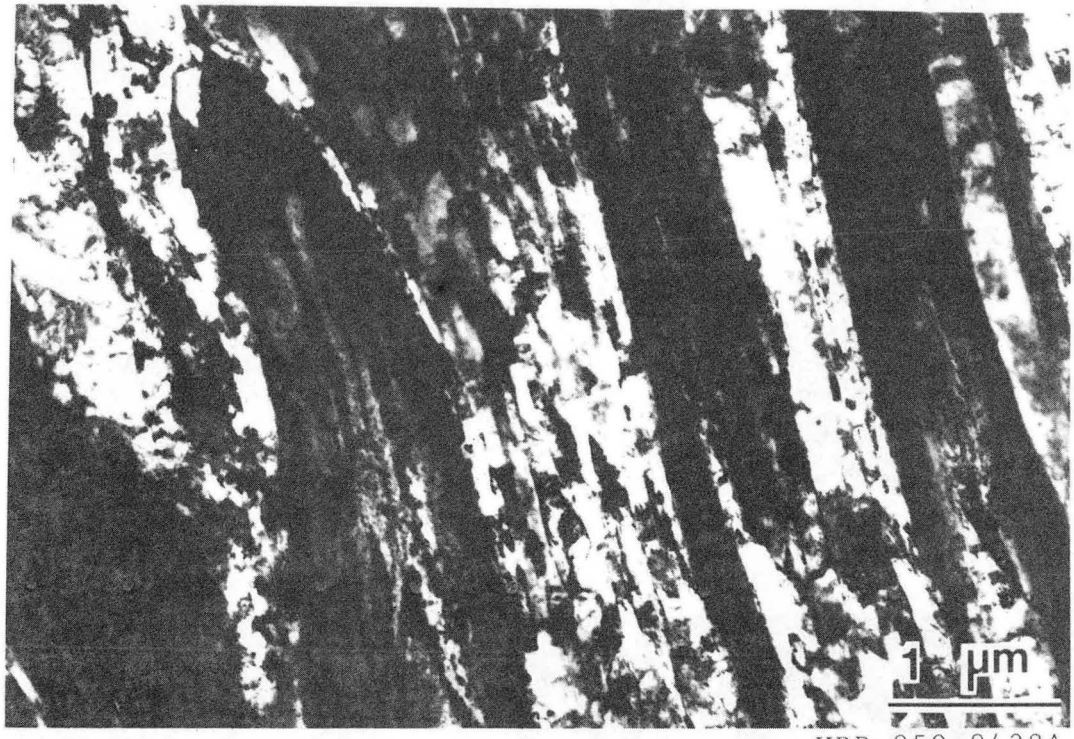

XBB 850-8432A

Fig. 27

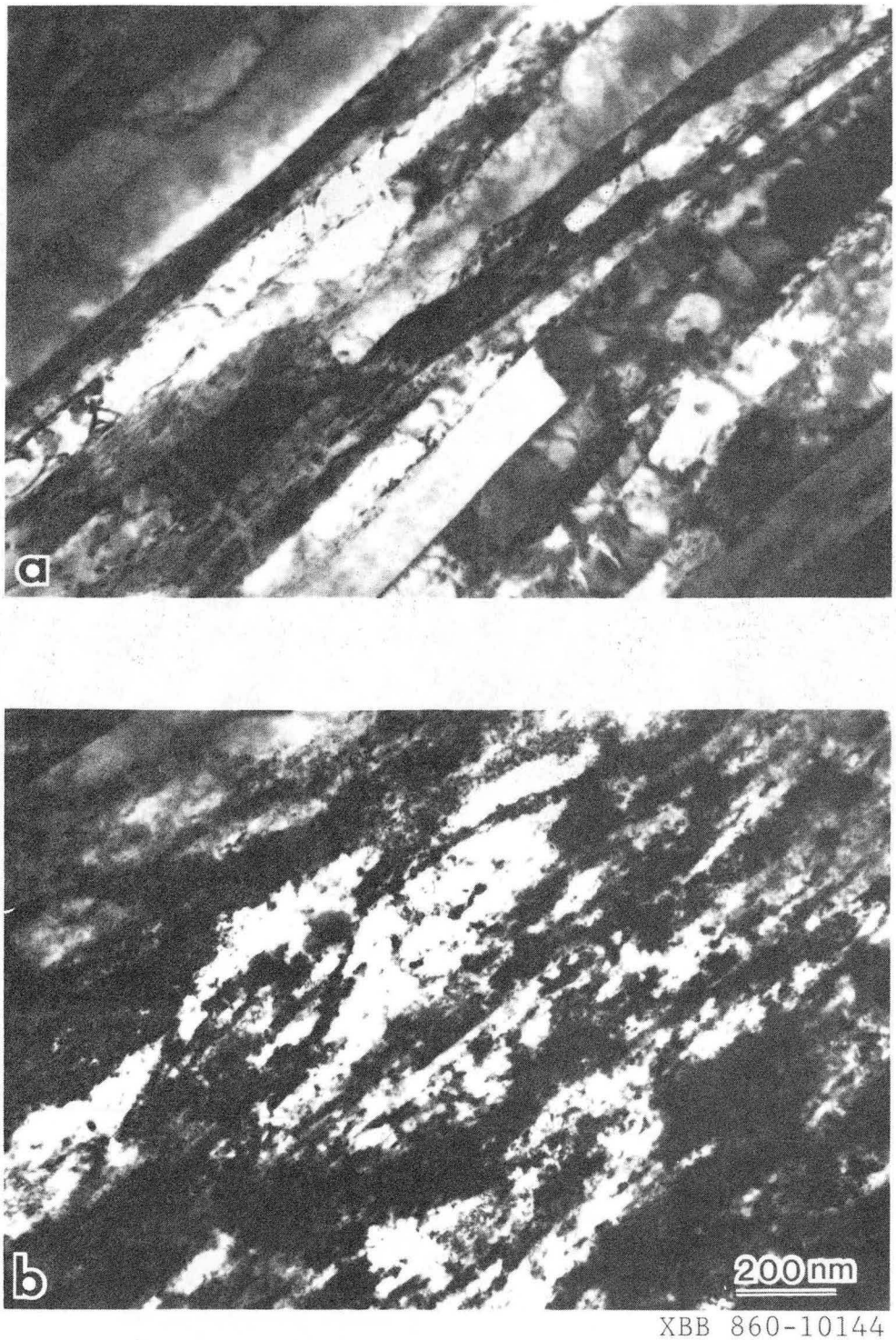

XBB 860-10144

Fig. 28

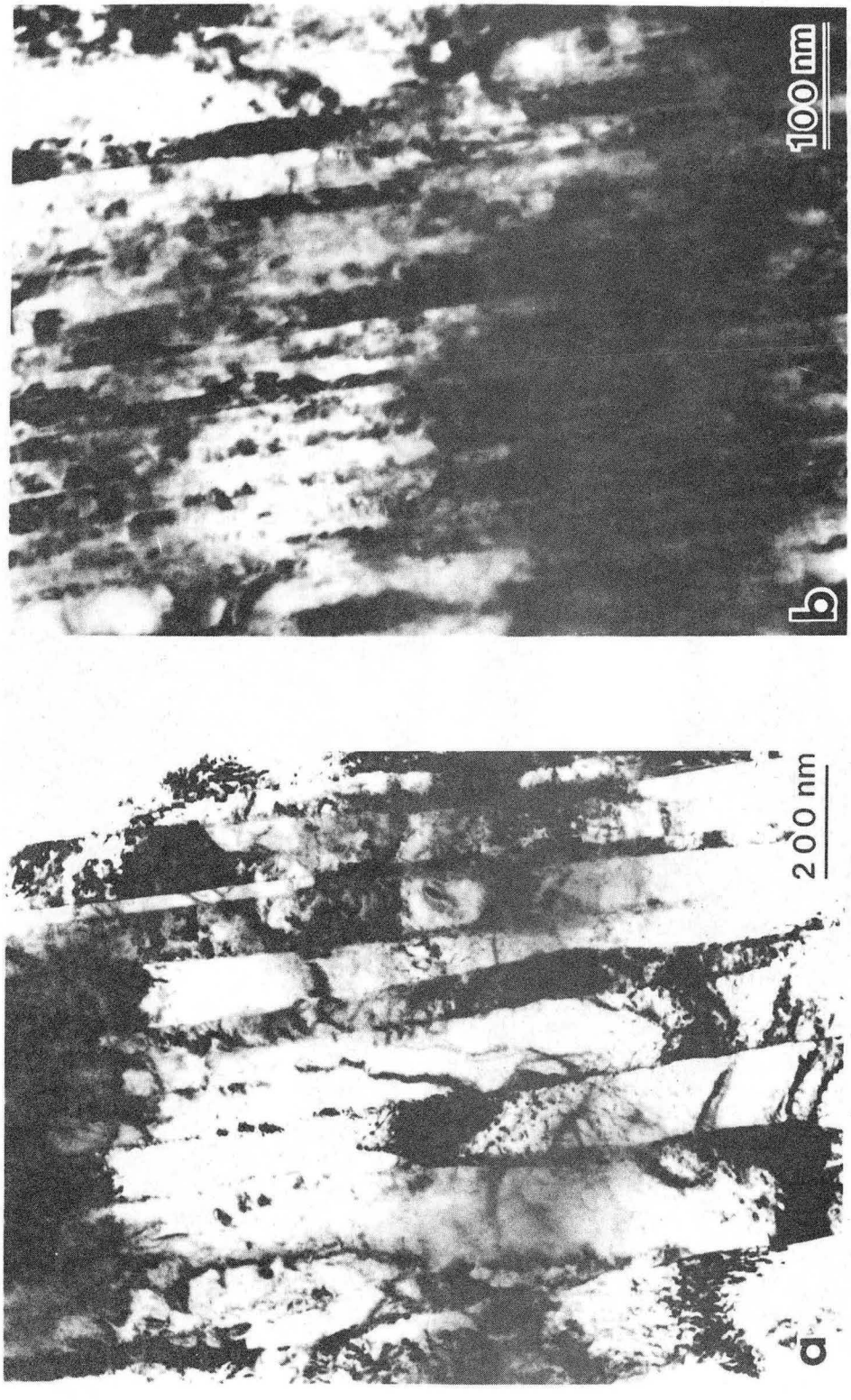

XBB 860-10142

Fig. 29

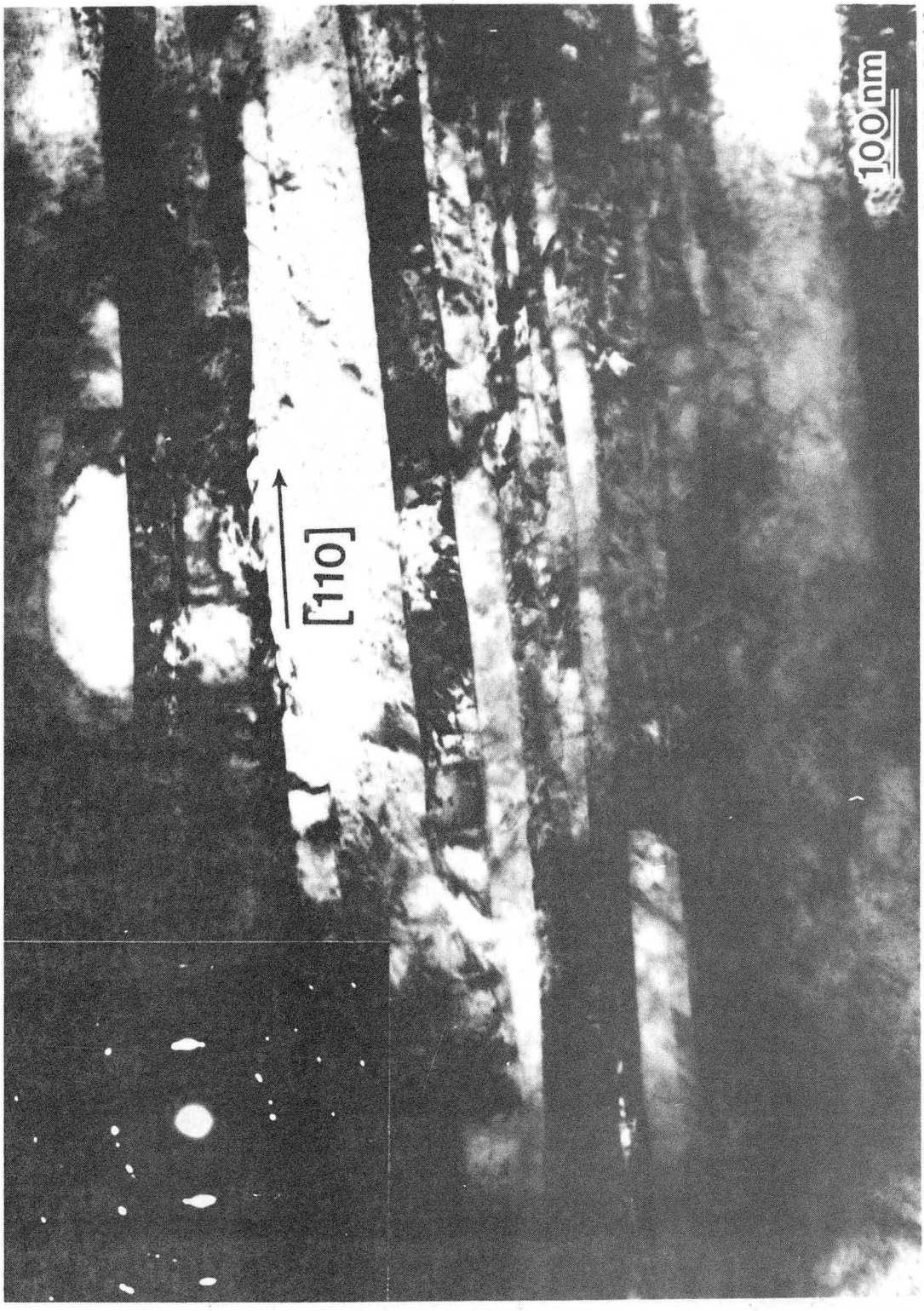

XBB 860-10143

Fig. 30

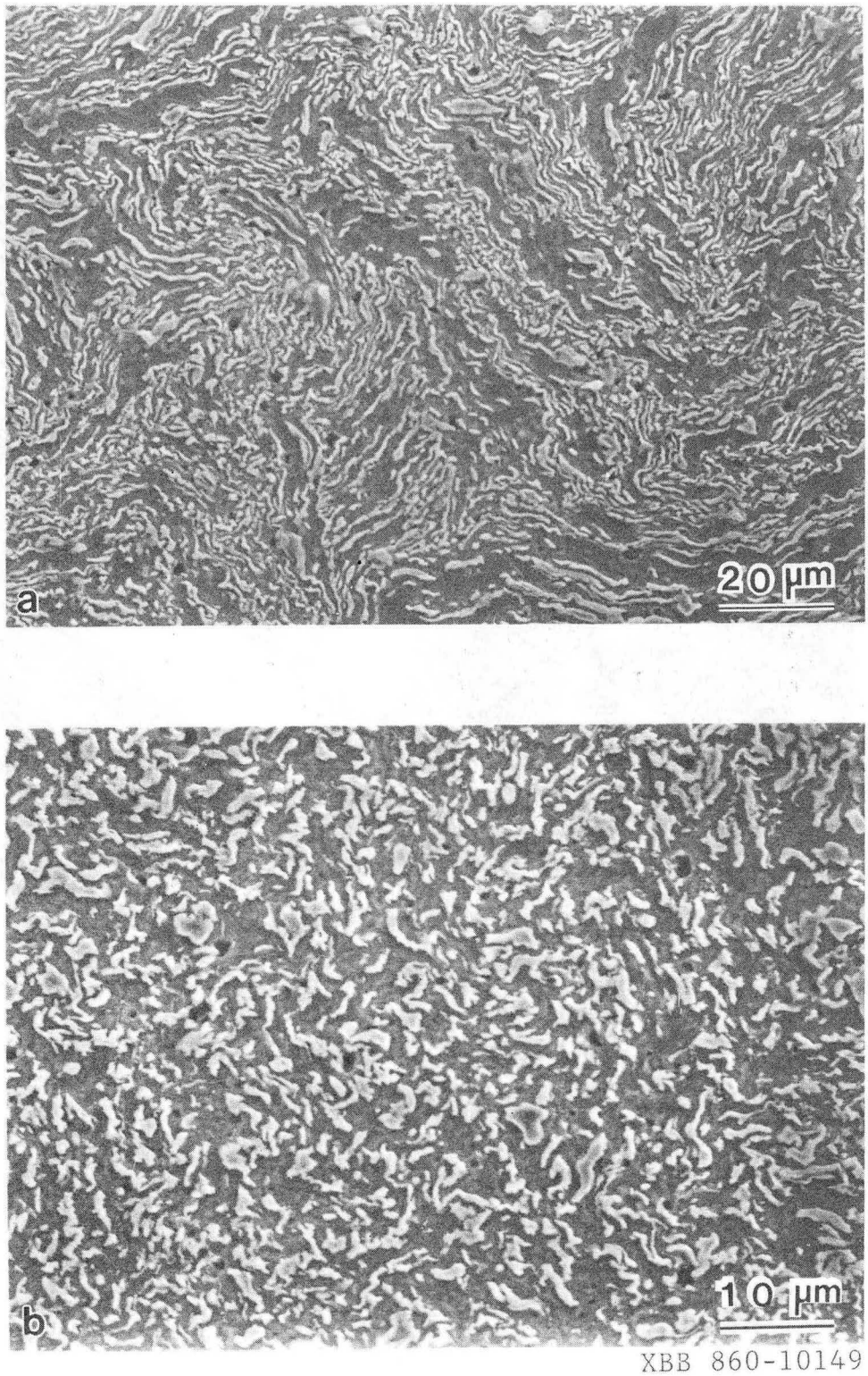

XBB 860-10149

Fig. 31

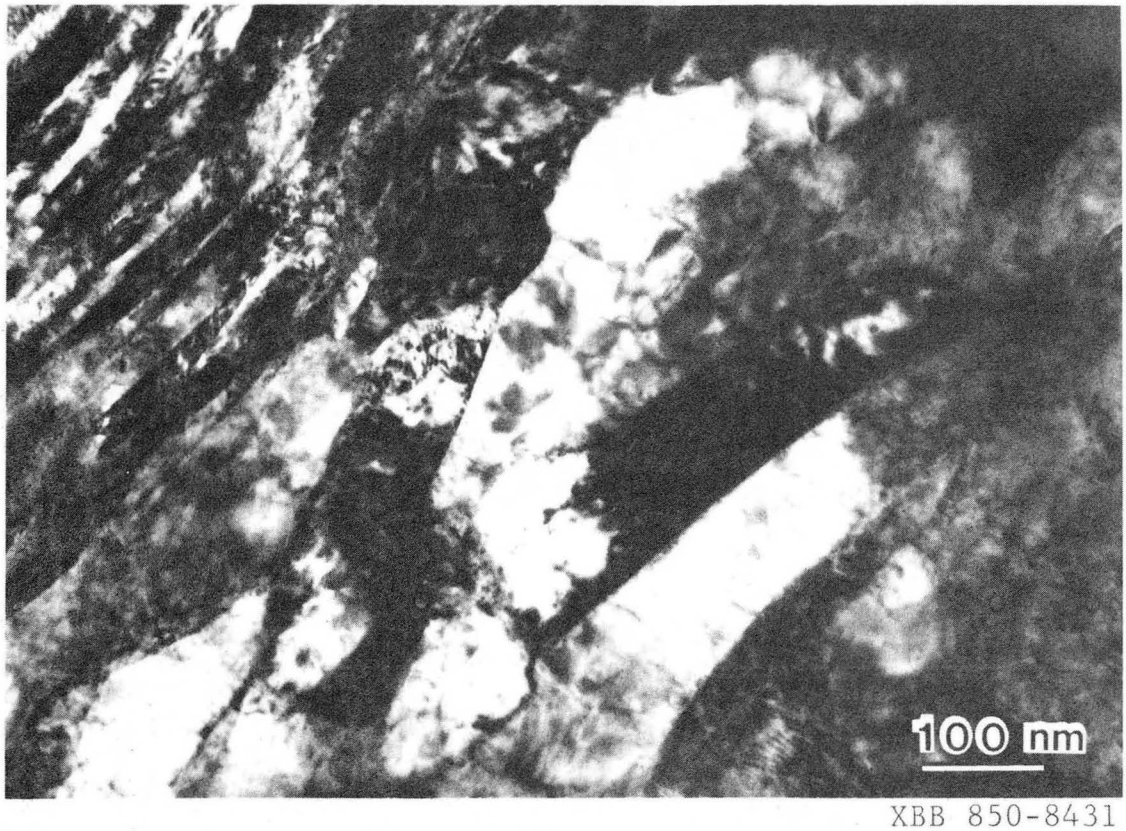

XBB 850-8431

Fig. 32

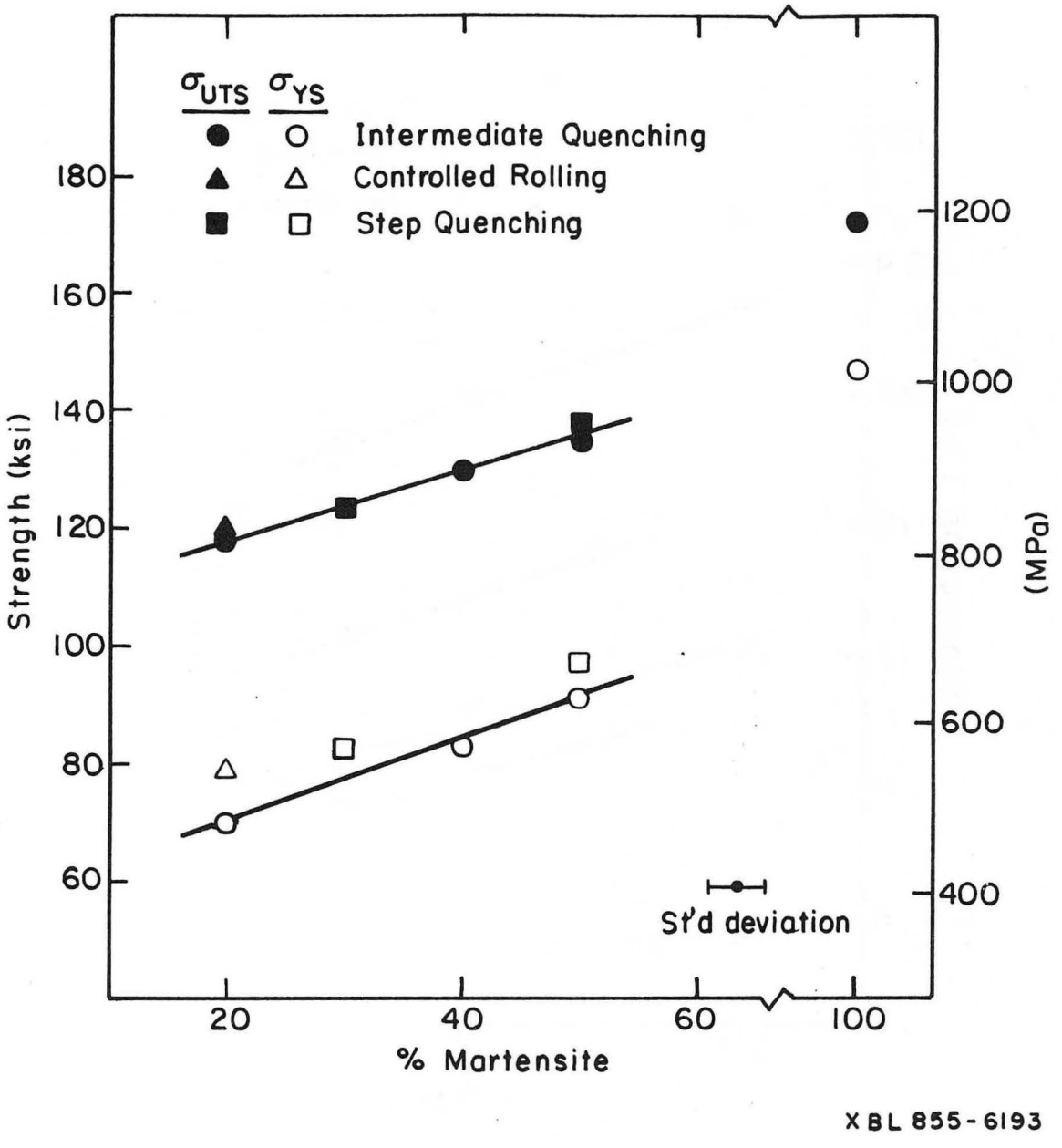
σ_{UTS} σ_{YS}
Intermediate Quenching
Controlled Rolling
Step Quenching
Strength (ksi)
180
160
140
120
100
80
60
1200
1000
800
600
400
(MPa)
St'd deviation
20
40
60
100
% Martensite
XBL 855-6193

Fig. 33

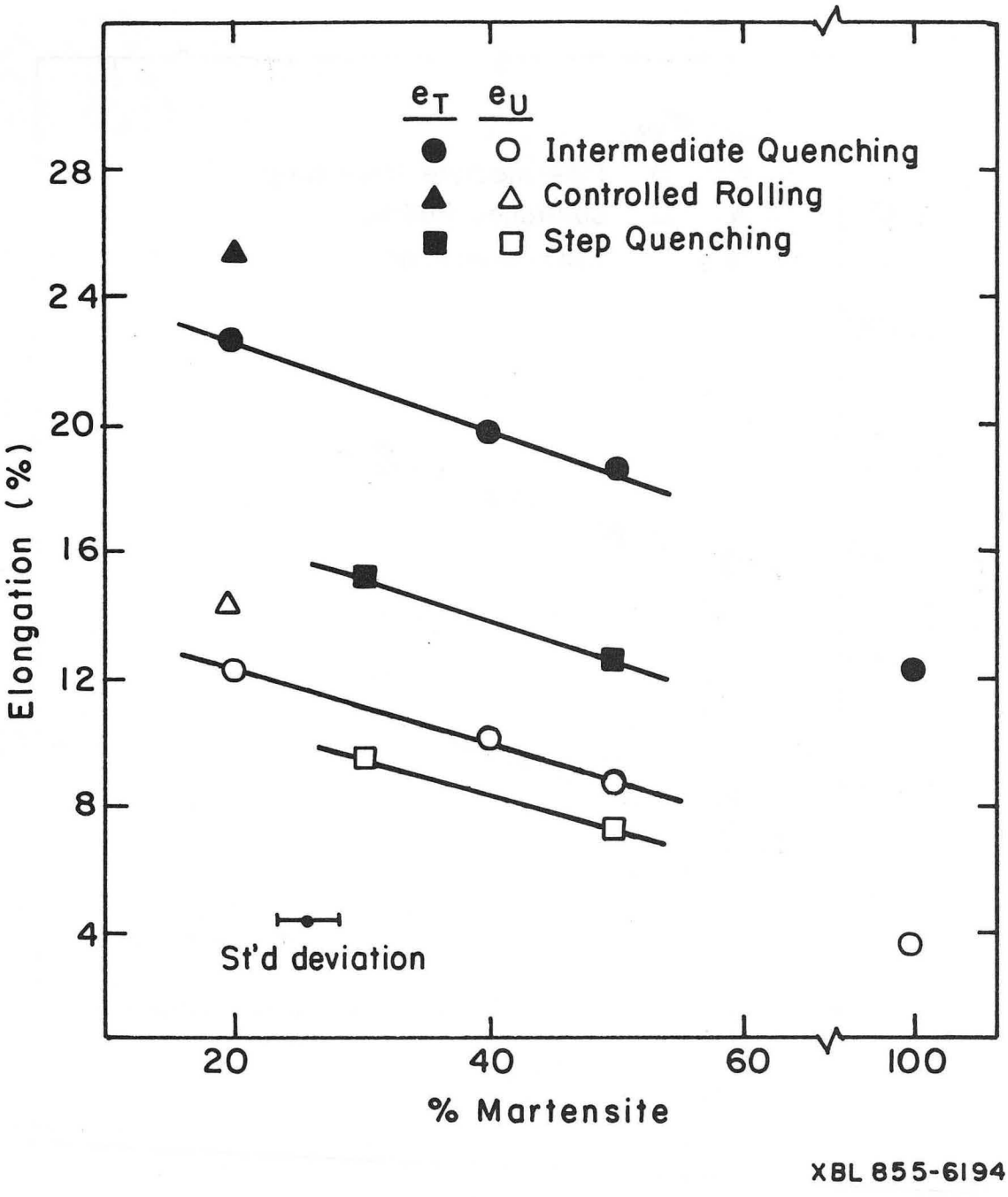
e_T e_U
Intermediate Quenching
Controlled Rolling
Step Quenching
28
24
20
16
12
8
4
Elongation (%)
St'd deviation
20
40
60
100
% Martensite
XBL 855-6194

Fig. 34

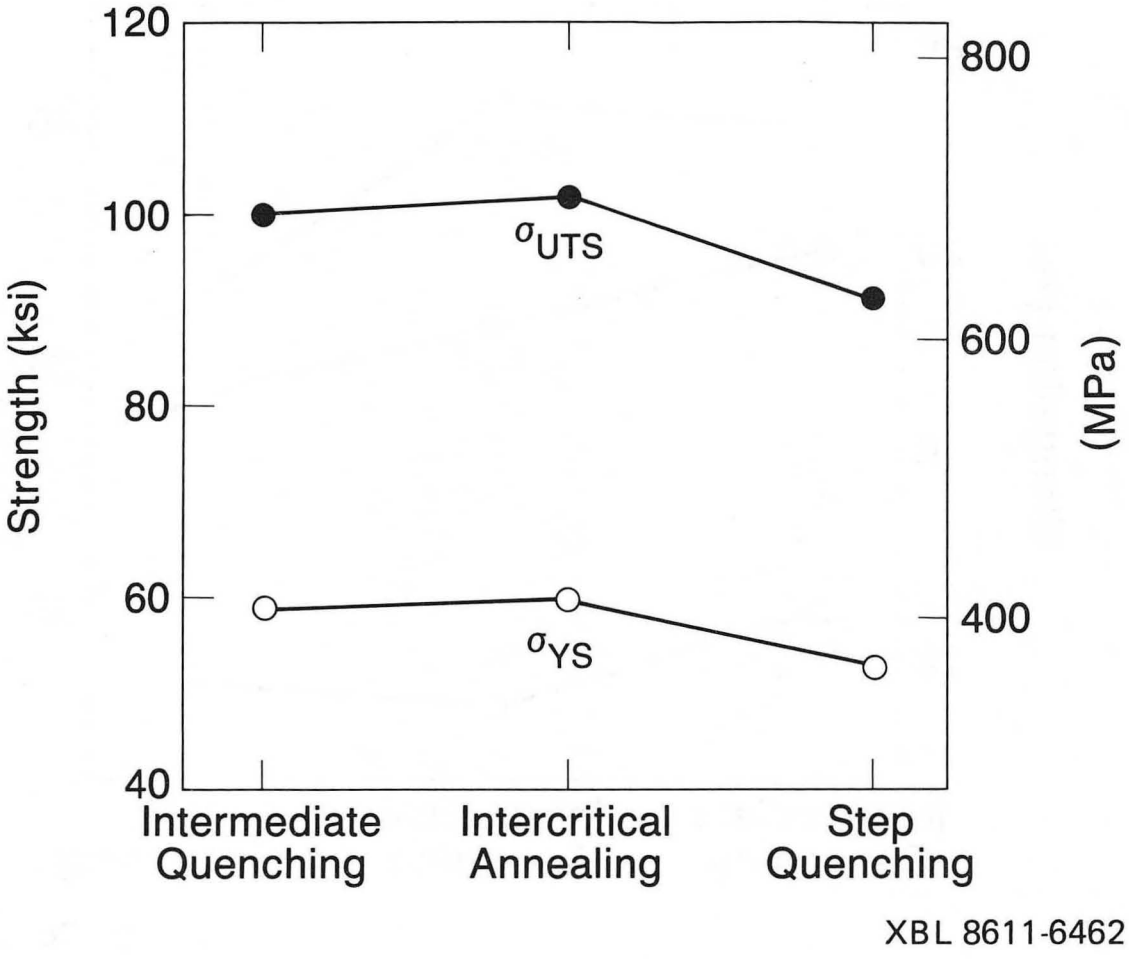
120
100
80
60
40
Strength (ksi)
800
600
400
(MPa)
σ_{UTS}
σ_{YS}
Intermediate Quenching
Intercritical Annealing
Step Quenching
XBL 8611-6462

Fig. 35

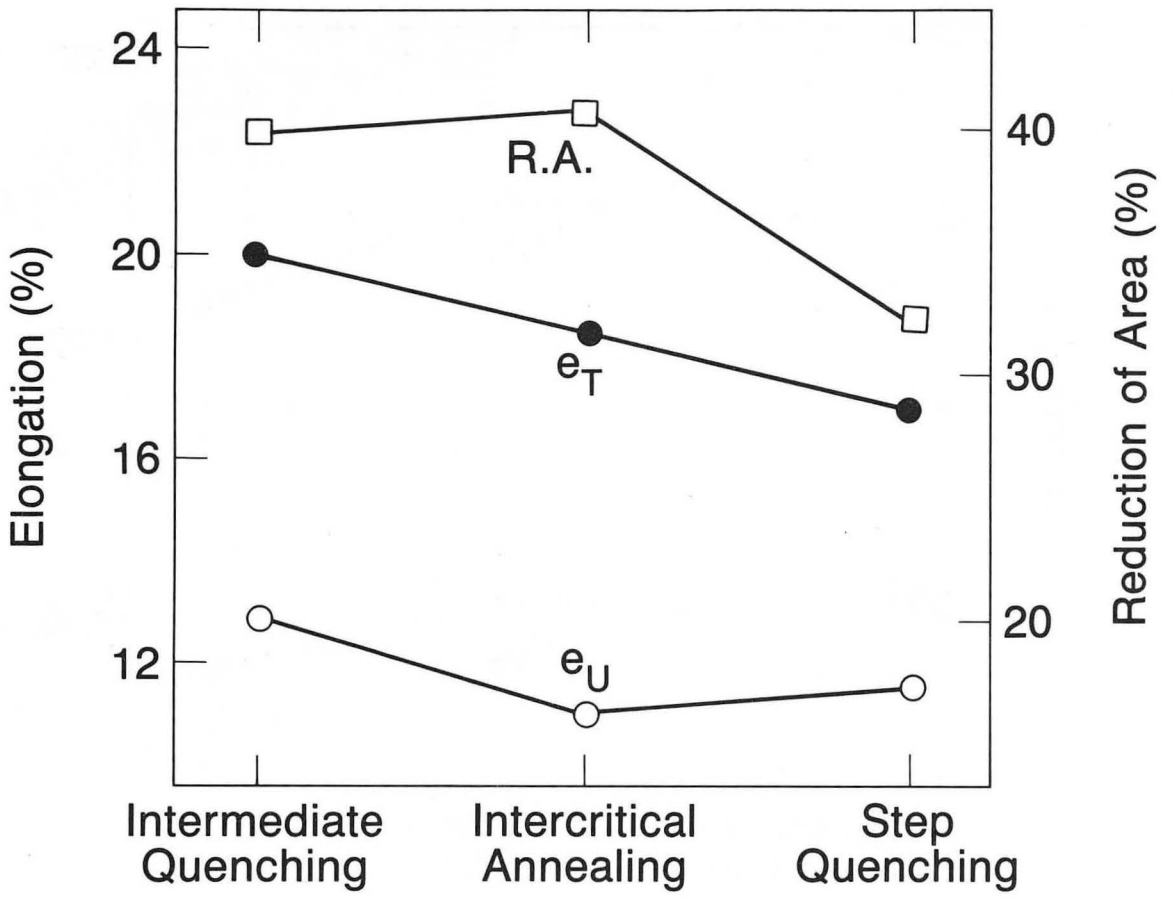
24
20
16
12
Elongation (%)
40
30
20
Reduction of Area (%)
R.A.
e_T
e_U
Intermediate Quenching
Intercritical Annealing
Step Quenching
XBL 8611-6463

Fig. 36

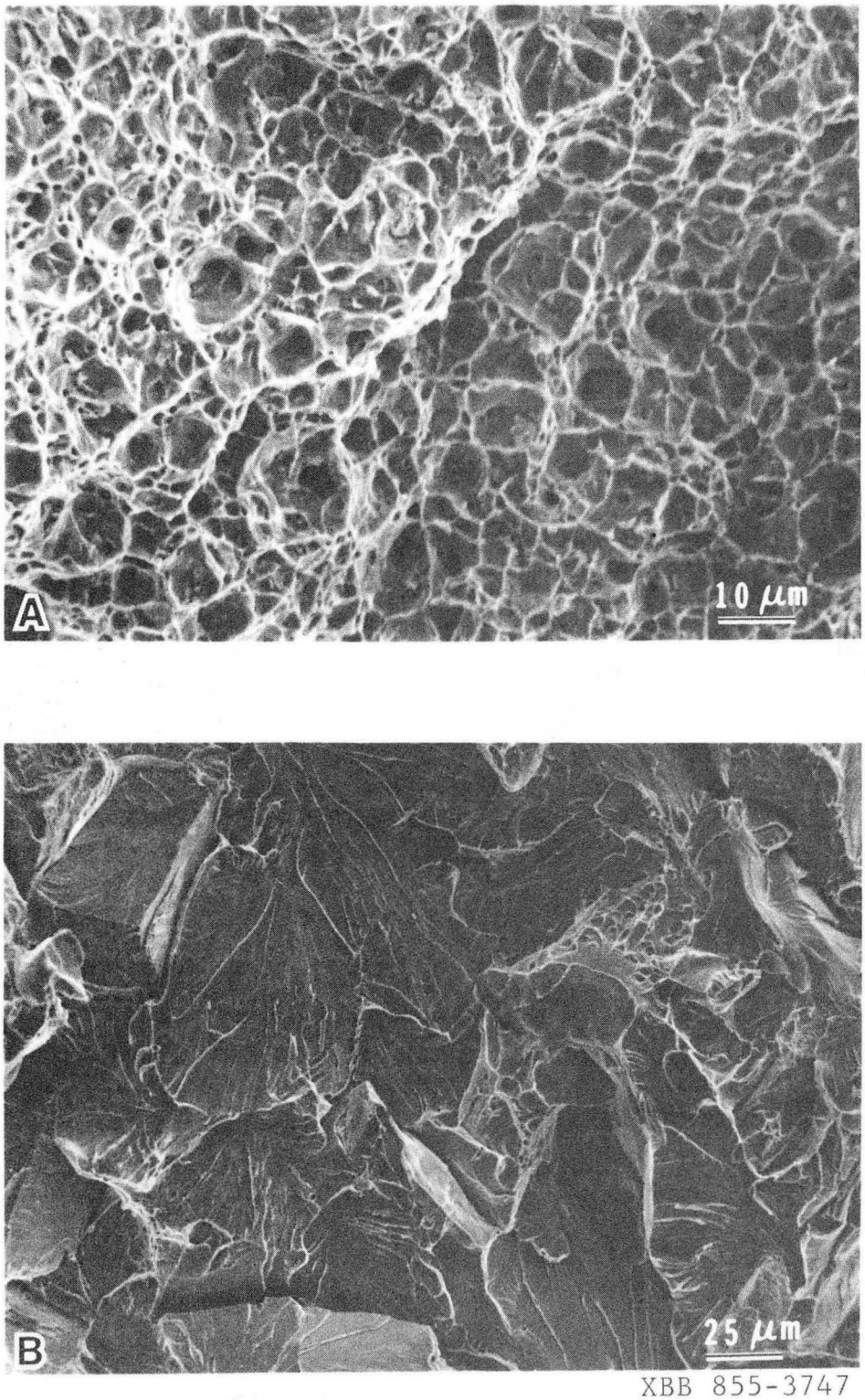

XBB 855-3747

Fig. 37

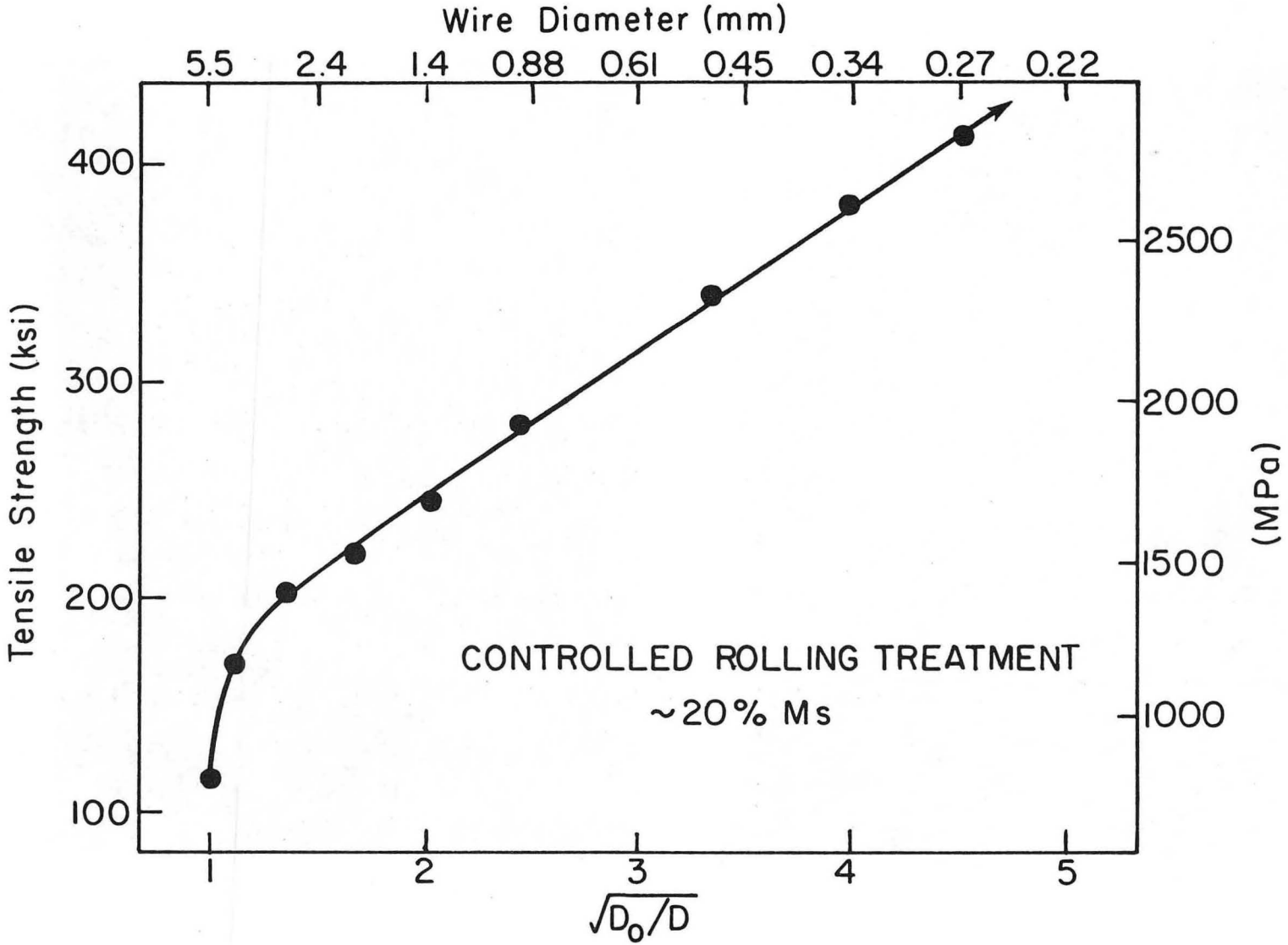
Wire Diameter (mm)
5.5
2.4
1.4
0.88
0.61
0.45
0.34
0.27
0.22
Tensile Strength (ksi)
400
300
200
100
2500
2000
1500
1000
(MPa)
CONTROLLED ROLLING TREATMENT
~20% Ms
1
2
3
4
5
$\sqrt{D_0/D}$
XBL 852-5870

Fig. 38

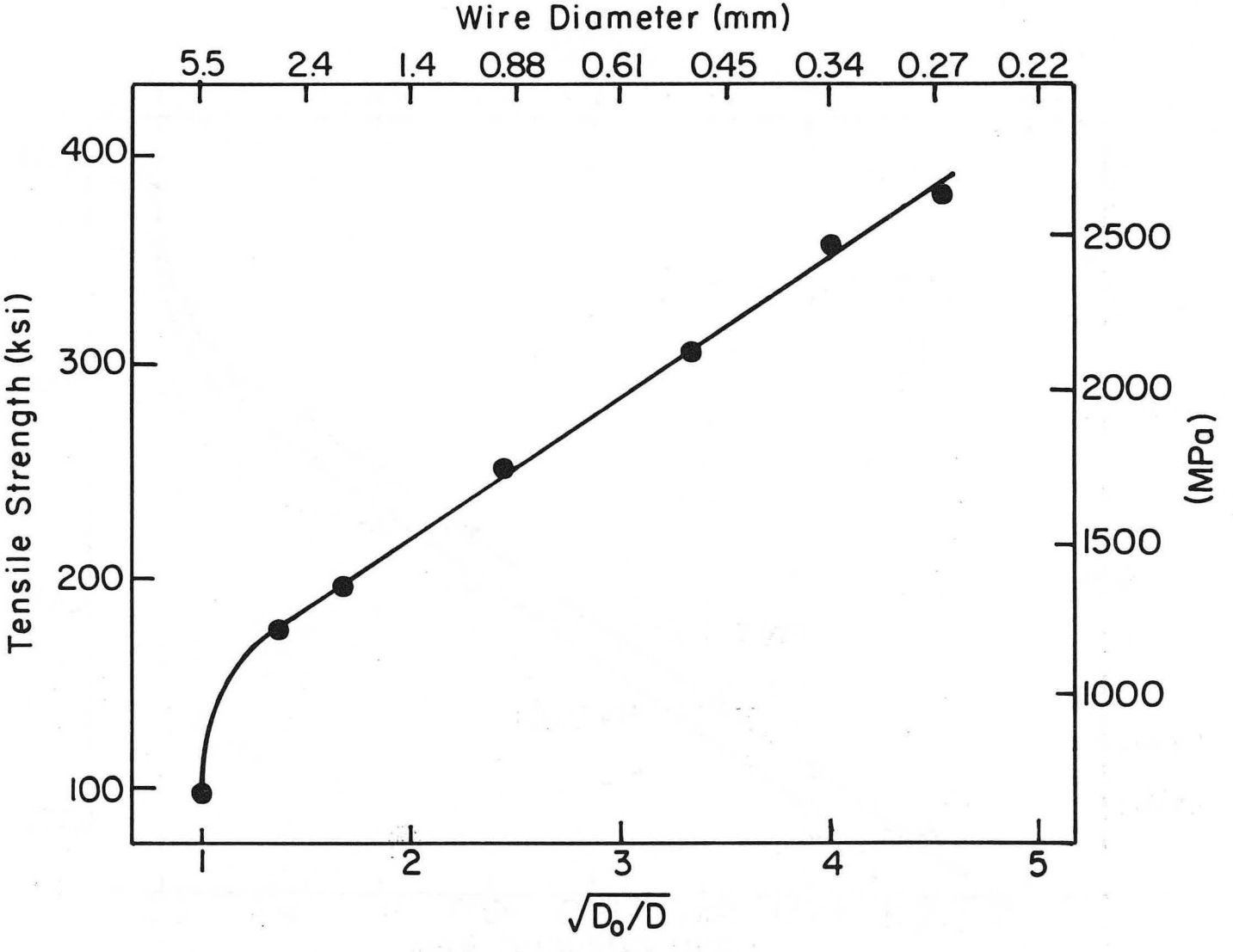
Wire Diameter (mm)
5.5
2.4
1.4
0.88
0.61
0.45
0.34
0.27
0.22
Tensile Strength (ksi)
400
300
200
100
2500
2000
1500
1000
(MPa)
1
2
3
4
5
$\sqrt{D_o/D}$
XBL857-6465

Fig. 39

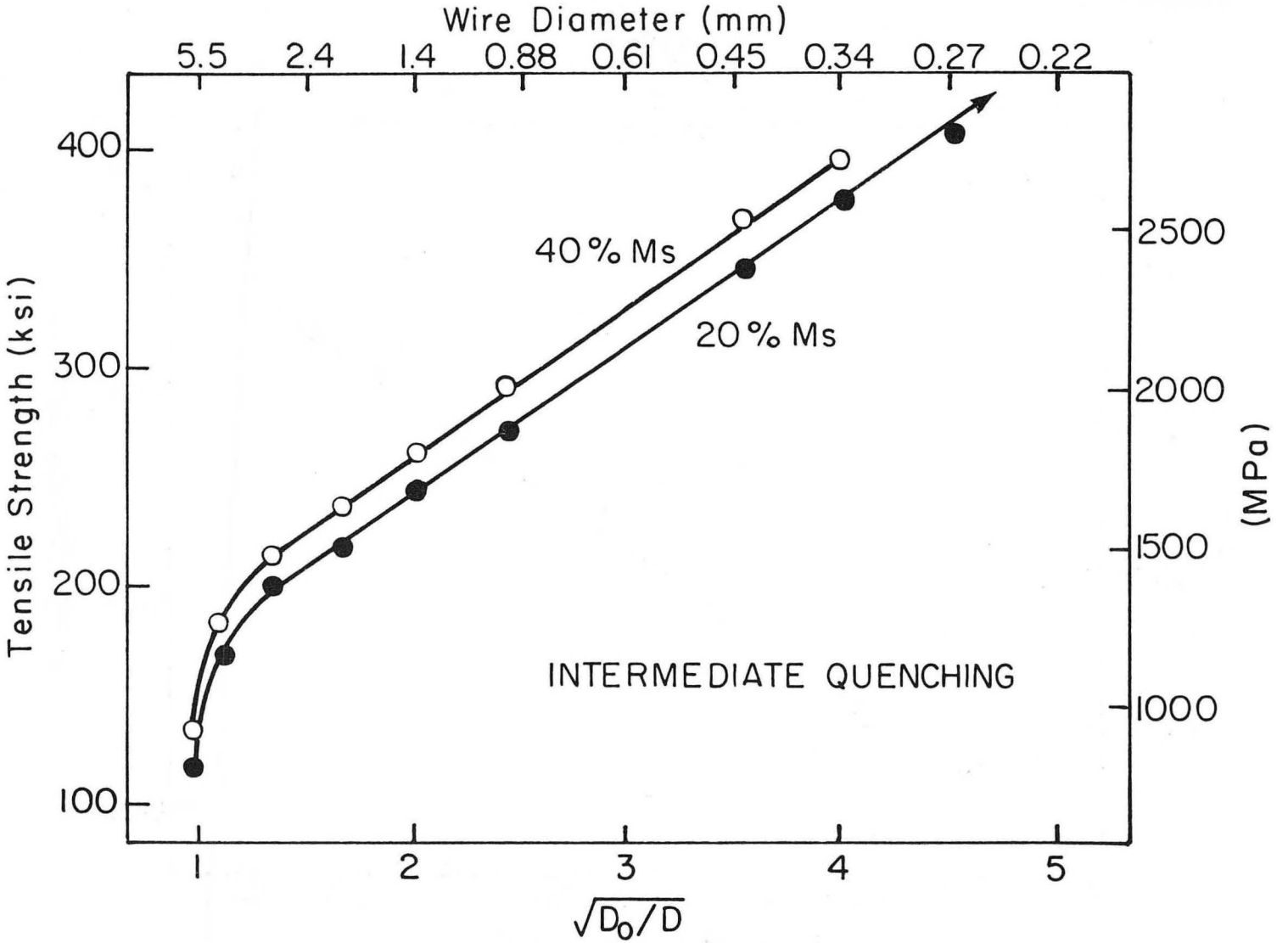

XBL852-5871

Fig. 40

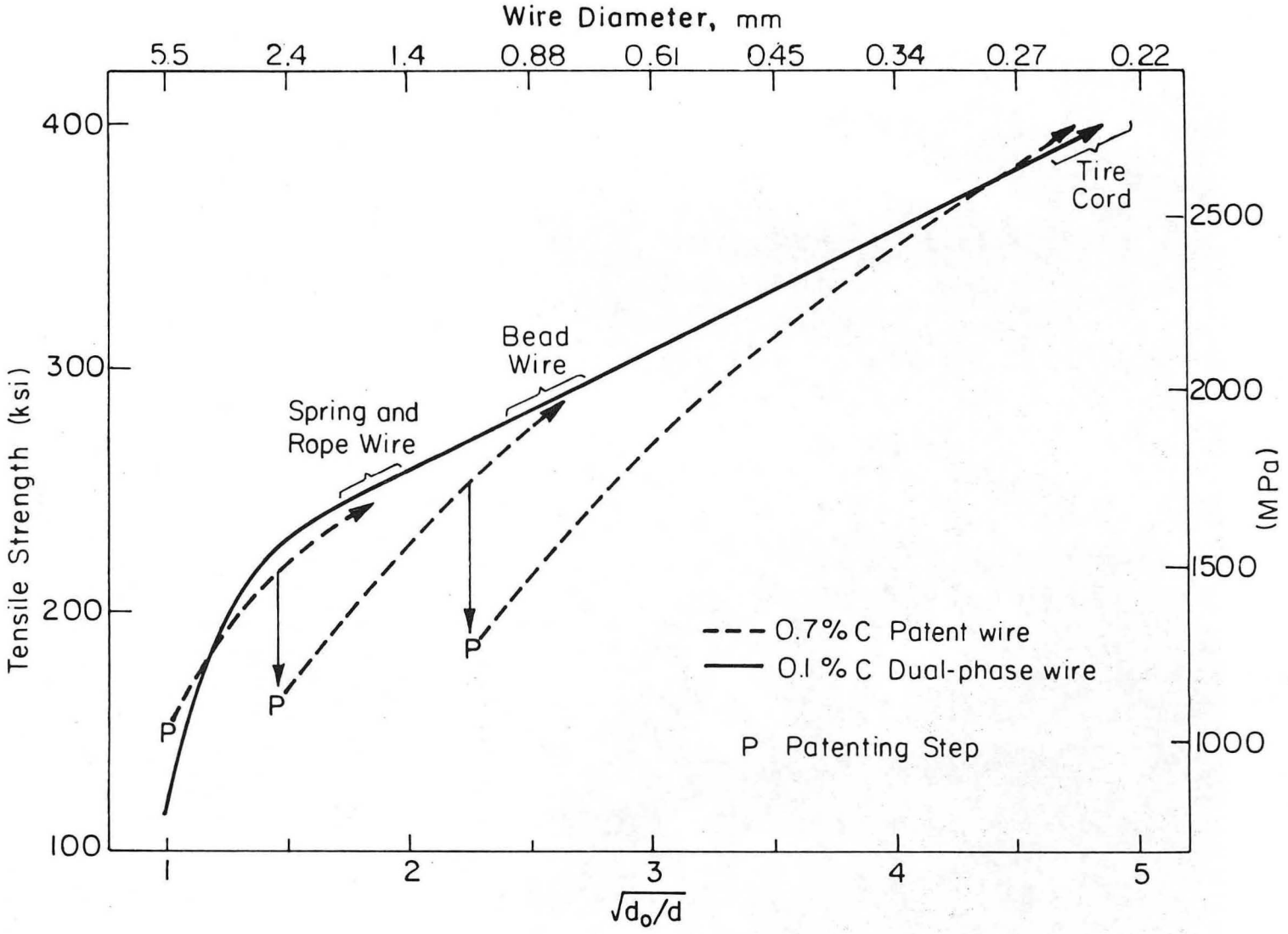

XBL 8210-6760B

Fig. 41

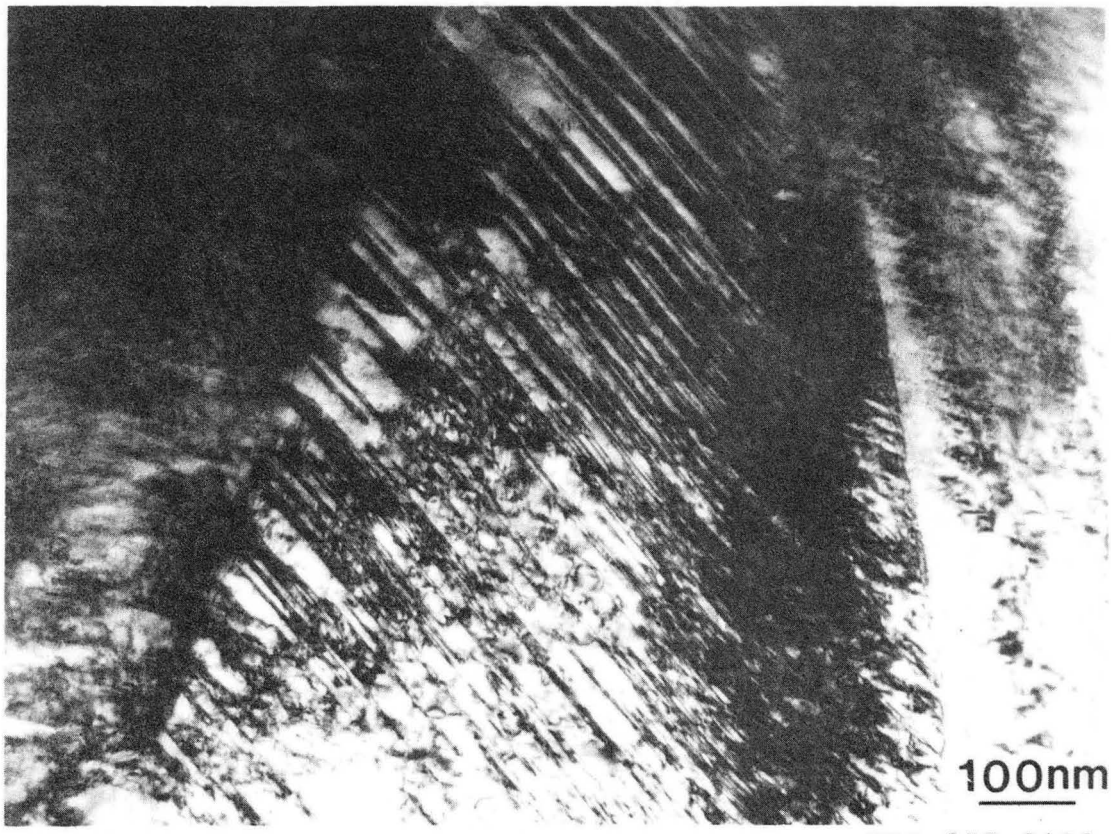

XBB 850-8428

Fig. 42

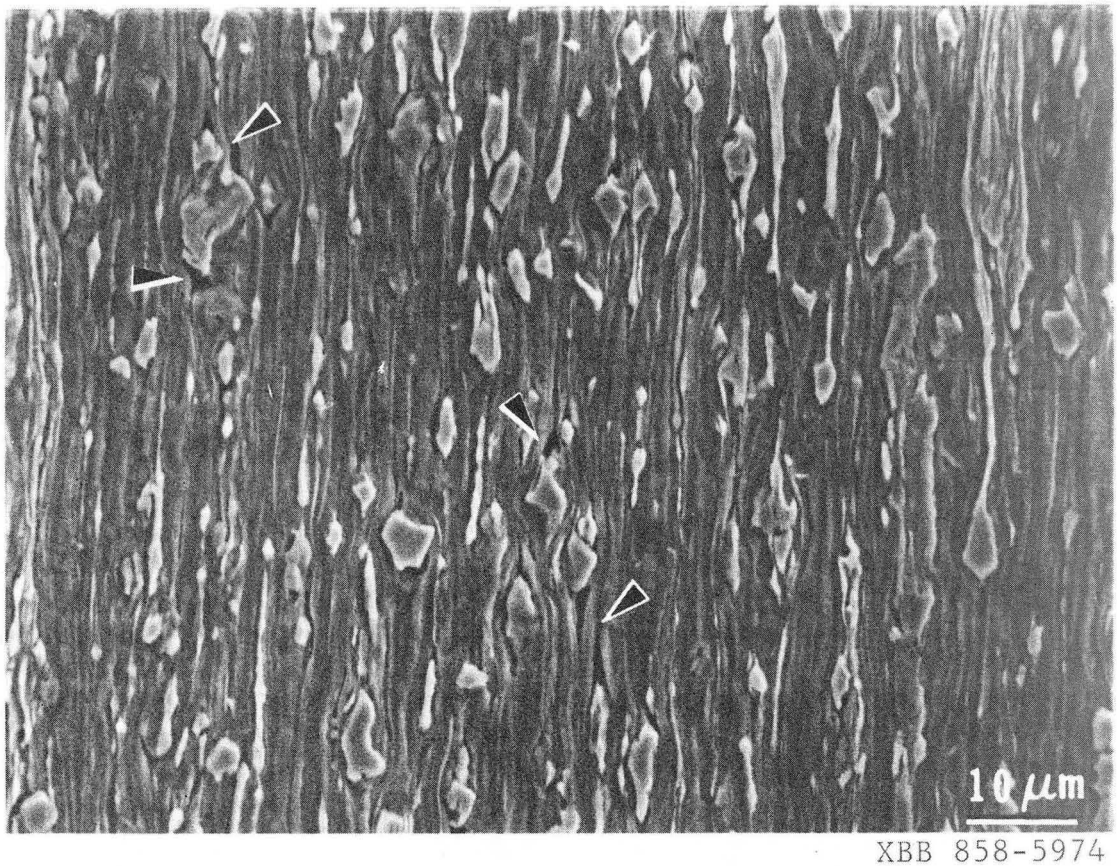

XBB 858-5974

Fig. 43

This report was done with support from the Department of Energy. Any conclusions or opinions expressed in this report represent solely those of the author(s) and not necessarily those of The Regents of the University of California, the Lawrence Berkeley Laboratory or the Department of Energy.

Reference to a company or product name does not imply approval or recommendation of the product by the University of California or the U.S. Department of Energy to the exclusion of others that may be suitable.

LAWRENCE BERKELEY LABORATORY
TECHNICAL INFORMATION DEPARTMENT
UNIVERSITY OF CALIFORNIA
BERKELEY, CALIFORNIA 94720